Diss. ETH No. 26522

Coupling Finite Elements and Auxiliary Sources

A thesis submitted to attain the degree of
DOCTOR OF SCIENCES of ETH ZURICH
(Dr. sc. ETH Zurich)

presented by

DANIELE CASATI

MSc ETH CSE, ETH Zurich

born on 04.06.1990

citizen of Italy

accepted on the recommendation of
Prof. Dr. Ralf Hiptmair, ETH Zurich, examiner
Prof. Dr. Jasmin Smajic, Hochschule für Technik Rapperswil, co-examiner
Prof. Dr. Igor Tsukerman, University of Akron, co-examiner

2020

Daniele Casati

Coupling Finite Elements and Auxiliary Sources

Abstract

We propose a hybrid method to solve time-harmonic Maxwell's equations in $\mathbb{R}^3$ through the *Finite Element Method* (FEM) in a bounded region encompassing parameter inhomogeneities, coupled with the *Multiple Multipole Program* (MMP) in the unbounded complement.

FEM and MMP enjoy complementary capabilities. FEM requires a mesh of the computational domain of interest. This is expensive, but can treat inhomogeneous materials, shapes with corners, or other singularities. Moreover, FEM allows a purely local construction of the discrete system of equations.

On the other hand, MMP belongs to the class of *methods of auxiliary sources* and of *Trefftz methods*, as it employs point sources that are exact solutions of the homogeneous equations as (global) basis functions: one only needs to evaluate them on hypersurfaces to obtain the discrete problem, and the resulting linear combination is valid in the whole domain where the equations hold, which can be unbounded. MMP performs well where the electromagnetic field is smooth, i.e. in the free space far from physical sources and material interfaces.

Thus, a natural way to combine the strengths of these methods arises when one needs to simulate the electromagnetic field of components with inhomogeneous parameters or nonsmooth shapes surrounded by free space: use FEM on a mesh defined on the components and MMP in the unbounded domain outside. The boundary between the FEM and MMP domains can be nonphysical if one surrounds the components by a conforming mesh of an "airbox" also modeled by FEM.

The interface conditions on the surface of the FEM domain are key to accurate coupled FEM–MMP solutions. Integrating by parts the variational form solved by FEM, surface integrals appear, through which one can impose interface conditions by substituting the ansatz of MMP.

However, one interface condition (for example, the continuity of the tangential trace for Maxwell's equations) cannot be imposed in this way.

To include this additional condition, we derive four methods from Lagrangian functionals that enforce both the variational form in the FEM domain and all the interface conditions between different discretizations:

1. *Least-squares-based coupling* using techniques from *PDE-constrained optimization.* This approach optimizes a functional for the additional condition, subject to a constraint expressed by the variational form of FEM.

2. *Discontinuous Galerkin* (DG) between the meshed FEM domain and the single-entity "MMP mesh", interpreting MMP as FEM with special basis functions.

3. *Multi-field variational formulation* in the spirit of *mortar finite element methods*, relying on the same interpretation of MMP as the DG-based coupling.

4. Coupling through the *Dirichlet-to-Neumann operator*: here we introduce a weak formulation of the additional condition where MMP basis functions are used as test functions. This approach is generalized to couple MMP with any numerical method based on volume meshes that fits *co-chain calculus.*

Furthermore, to minimize the meshed region and for the sake of generalization, we assume that equation parameters are *piecewise constant* in the MMP domain (instead of constant everywhere). This induces a partition: we consider the case of one unbounded subdomain with other bounded, but possibly very large, subdomains, each requiring its own MMP discretization space (but without the need of meshes). Hence, on top of the interface conditions between the FEM and MMP domains, one should also impose interface conditions between the MMP subdomains themselves.

We compare the FEM–MMP coupling approaches in a series of numerical experiments with different geometries and equation parameters, including examples that exhibit triple-point singularities. Convergence tests are performed for examples that cover the whole spectrum of computational electromagnetics, obtaining the expected results.

Riassunto

Proponiamo un metodo ibrido per risolvere in $\mathbb{R}^3$ equazioni di Maxwell armoniche nel tempo tramite il *metodo degli elementi finiti* (FEM) in una regione limitata caratterizzata da parametri disomogenei, accoppiato col *programma dei "multipoli multipli"* (Multiple Multipole Program, MMP) nel complemento illimitato.

FEM ed MMP offrono caratteristiche complementari. FEM richiede una mesh del dominio di interesse. Ciò è dispendioso, ma permette di trattare materiali disomogenei, figure con spigoli o altre singolarità. Inoltre, con FEM si può costruire localmente il sistema di equazioni discreto.

D'altra parte, MMP appartiene alla classe dei *metodi delle sorgenti ausiliarie* e dei *metodi di Trefftz*, dato che utilizza come funzioni di base (globali) delle sorgenti puntiformi che sono soluzioni esatte delle equazioni omogenee: per ottenere il problema discreto si deve valutarle solo su ipersuperfici, e la combinazione lineare risultante è valida nell'intero dominio di validità delle equazioni, che può essere illimitato. MMP funziona bene quando il campo elettromagnetico è regolare, ovvero in spazio libero da sorgenti fisiche e interfacce di materiali.

Si ha quindi un modo naturale di combinare i punti di forza di questi metodi quando si vuole simulare il campo elettromagnetico di componenti con parametri disomogenei o forme non lisce circondate da spazio libero: si usi FEM su una mesh definita sulle componenti ed MMP nel dominio illimitato esterno. Il bordo tra i domini FEM ed MMP può non essere fisico se si circondano le componenti con una mesh conforme di una "scatola d'aria", anch'essa modellata da FEM.

Le condizioni di interfaccia sulla superficie del dominio di FEM sono cruciali per ottenere soluzioni accoppiate tra FEM ed MMP. Integrando per parti la forma variazionale risolta da FEM, appaiono integrali di superficie con cui si possono imporre condizioni di interfaccia sostituendovi l'ansatz di MMP.

Tuttavia, una delle condizioni di interfaccia (ad esempio, la continuità della traccia tangenziale per equazioni di Maxwell) non può essere imposta in questo modo.

Per includere questa condizione aggiuntiva, deriviamo quattro metodi da funzionali di Lagrange che impongono sia la forma variazionale delle equazioni nel dominio di FEM, sia tutte le condizioni di interfaccia tra discretizzazioni differenti:

1. *Accoppiamento basato sui minimi quadrati* tramite tecniche di ottimizzazione con vincoli dati da equazioni alle derivate parziali. Questo approccio ottimizza un funzionale per la condizione aggiuntiva soggetto ad un vincolo espresso dalla forma variazionale di FEM.

2. *Galerkin discontinuo* (DG) tra la mesh di FEM e la "mesh di MMP" formata da una sola cella, se si considera MMP come un metodo agli elementi finiti con funzioni di base speciali.

3. *Formulazione variazionale multicampo* nello spirito dei metodi degli elementi finiti *mortar*, che si affida alla stessa interpretazione di MMP su cui si fonda l'accoppiamento basato su DG.

4. Accoppiamento tramite l'*operatore Dirichlet a Neumann*: introduciamo una formulazione debole della condizione aggiuntiva dove funzioni di base MMP sono usate come funzioni test. Questo approccio si può generalizzare per accoppiare MMP con qualsiasi metodo numerico basato su mesh di volume che rientri nel *calcolo delle cocatene*.

Inoltre, per minimizzare la regione con mesh e per generalizzare, assumiamo che i parametri delle equazioni siano *costanti a tratti* nel dominio MMP (invece di costanti ovunque). Ciò induce una partizione: consideriamo il caso di un solo sottodominio illimitato assieme ad altri sottodomini limitati, che comunque possono essere molto grandi, ciascuno col proprio spazio di discretizzazione MMP (ma senza bisogno di mesh). Dunque, in aggiunta alle condizioni di interfaccia tra i domini FEM ed MMP, si devono anche imporre condizioni di interfaccia tra gli stessi sottodomini di MMP.

Paragoniamo i modi di accoppiare FEM ed MMP in una serie di esperimenti numerici con diverse geometrie e parametri delle equazioni, inclusi esempi che esibiscono singolarità di punto triplo.

Eseguiamo test di convergenza per esempi che coprono l'intero spettro dell'elettromagnetismo computazionale, ottenendo i risultati sperati.

Acknowledgments

Contents

Contents

Acronyms

BEM Boundary Element Method. xx, xxi, 55, 115

DEC Discrete Exterior Calculus. 56

DG Discontinuous Galerkin. iv, vi, 32, 38–40, 43, 45, 48, 50, 68, 70, 89, 95, 107, 109, 111, 113–115

DoF Degree of Freedom. xv, xvi, 76–78, 89, 91, 107, 109–111, 113, 114

DtN Dirichlet-to-Neumann. xii, xv, xxii, xxiii, 50–53, 55, 61, 67, 70, 84, 95, 97, 100, 102, 103, 115

FEEC Finite Element Exterior Calculus. 56

FEM Finite Element Method. iii–vi, xiii, xvi, xvii, xx–xxiv, 1, 4–7, 11, 14, 29–32, 38–40, 43, 50, 53, 55, 56, 65–69, 71, 72, 74, 76, 78, 81, 83, 84, 86, 87, 89, 92, 95, 97–99, 103–105, 107, 109, 111, 112, 114, 115

MAS Method of Auxiliary Sources. 14, 15

MMP Multiple Multipole Program. iii–vi, xiii, xv, xvi, 13, 15, 17, 19, 20, 22–30, 38, 40, 42, 45, 48, 50, 55, 65–72, 74–76, 78, 80–84, 86–89, 91, 92, 94, 95, 97, 98, 103–107, 109–111, 113, 114

PDE Partial Differential Equation. iv, xi, 11, 14, 15, 32, 33, 35–37, 42, 53, 70, 89, 104, 107, 111, 113–115

TPS Triple-Point Singularity. xv–xvii, xxiii, 25–28, 87–89, 91, 107–114

---

[0]*Notation.*

   Subscript f in formulas: FEM.
   Subscript m in formulas: Trefftz method (MMP).
   Superscript n in formulas: discrete.

List of Figures

List of Figures

Introduction

Computational electromagnetics is devoted to the numerical simulation of the interactions of the electromagnetic field with the physical world. Compared to the subject of electromagnetism, the focus is on practical applications, rather than the theory.

The well-known *Maxwell's equations* in differential form [43, p. 337, (7.40)] constitute the basis of this analysis. These linear equations look simple and almost symmetric with respect to their unknowns, and present smooth exact solutions where equation parameters are constant (for example, [43, p. 395, (9.43)]). Difficulties arise from complex geometries or local equation parameters, which can even be nonlinear or subject to a *hysteresis loop* (see [43, p. 290]); for example, these parameters can have jump discontinuities on the interface between different materials. Hence, the geometry of the components forming the spatial domain is of paramount importance.

Different numerical methods perform best in different circumstances. Methods relying on volume meshes can handle singularities of shapes with corners by locally refining the mesh there, but only work in bounded domains. Other methods only require evaluations on hypersurfaces to obtain a solution that also holds inside volumes, as long as the problem is simple enough, but require to explicitly know the solution of some other related problem in advance (for example, for the homogeneous equation).

A common strategy to simulate real-world applications is to use methods of the first class, which can handle inhomogeneities, with a boundary condition that well approximates the field despite artificially truncating the mesh.

Some boundary conditions are trivial to implement, such as the surface of a *perfect electric conductor*, where the tangential component of the electric field and the normal component of the magnetic field are set to zero [43, p. 425, (9.175)]. Things become more difficult if the solution is a wave propagating to infinity. In this case, *absorbing boundary conditions* or *perfectly matched*

layers can be used [72]. Both, however, are local approximations to nonlocal operators, and therefore have limitations [59, p. 14, Section 7].

Hence, a good strategy is to use both kinds of methods discussed above, based on volume meshes and hypersurfaces, for the same problem, i.e. to devise a *hybrid domain-decomposition method*. *Domain decomposition* refers to splitting the equations into coupled problems on smaller subdomains forming a partition of the original domain. To form a hybrid method, this decomposition becomes relevant at the discrete level, where different approximation methods are employed in each subdomain.

The most popular hybrid method is probably the *Finite Element Method* (FEM) coupled with the *Boundary Element Method* (BEM): as a famous paper states in the title, the marriage of convenience (*à la mode*) between these methods can achieve the "best of both worlds" [15]. FEM is not only apt to model inhomogeneous materials, but can also be used without knowing fundamental solutions of the governing differential equations. These solutions, which BEM requires, can be nonexistent or extremely complex.

On the other hand, BEM is clearly better-suited for domains involving a small ratio of boundary surface to volume: extreme cases are unbounded domains. Moreover, the coupling of FEM and BEM is not very difficult, as both have their roots in integrations by parts by means of Green's identities [64, p. 4, (1.8) and (1.9)] (*variational form* for FEM, *boundary integral equation* for BEM) and are set in related function space frameworks [8].

However, BEM presents two disadvantages:

1. Singular integrals in its formulation. While one can usually get rid of these singularities (for example, with *Duffy transformations* or analytic integrals for some geometries of the boundary), an ad-hoc solution per problem has to be identified. This complicates the implementation, which cannot be a "black box", i.e. valid for any problem involving Maxwell's equations, as with FEM.

2. More importantly, given that kernels of boundary integral equations are nonlocal, BEM leads to large, dense matrices. A whole set of techniques is devoted to their study (*panel-clustering methods* or *hierarchical matrices* [75, pp. 464–465, Section 7.6]), but those same matrices still appear

as blocks of the linear system of equations originating from coupling FEM and BEM.

Thus, we propose to couple FEM with a *Trefftz method* (Chapter 2) instead of BEM. In fact, Trefftz methods present the following desirable features:

1. No singular integrals, because if Trefftz basis functions have central singularities, they are placed at points outside the Trefftz domain of approximation. When coupled with FEM, these singularities are therefore positioned in the FEM domain.

2. When applied to analytic solutions, the approximation error of Trefftz methods *converges exponentially*. We can formally prove this when Trefftz methods are used to model the Poisson's equation [64, p. 246, Chapter 8] in $\mathbb{R}^2$ (Section 2.3) and show it empirically for Maxwell's equations (Section 2.4).

Quoting again the author arguing in favor of the marriage between BEM and FEM [87, p. 314, Section 5],

> it seems without doubt that in the future Trefftz type elements will frequently be encountered in general finite element codes. [...] It is the author's belief that the simple Trefftz approach will in the future displace much of the boundary type analysis with singular kernels.

Of course, Trefftz methods also have a major flaw, namely their dependence on *heuristics*, especially impacting the choice of Trefftz basis functions in 3D settings. As a matter of fact, when modeling close to field singularities or sources, the quality of their numerical solutions is heavily impacted by the choice of Trefftz basis functions; e.g., the position of their central singularities inside the FEM domain. An ideal strategy is therefore to apply FEM where the field is difficult to model and Trefftz methods elsewhere, such that heuristics becomes irrelevant. This suggests to use an *artificial interface* between the FEM and Trefftz domains, not coinciding with any discontinuity of material properties.

Throughout this thesis we show how well the coupling between FEM and Trefftz methods matches the aforementioned expectations through numerical

results covering the whole spectrum of *frequency-domain* computational electromagnetics.

Scope

Several approaches to couple FEM and a Trefftz method for the Poisson's equation in both 2D and 3D have been discussed by the author from the perspective of numerical analysis in [28]. Existence, uniqueness, and stability of all coupling approaches is formally proven in that work, which only deals with scalar unknown functions. We offer numerical evidence for Maxwell's equations (vector unknown functions) in [29, 30], which illustrate numerical convergence results for the magnetostatic and eddy-current equations, respectively.

[26] generalizes one of the coupling approaches, the *Dirichlet-to-Neumann-based coupling* (DtN-based coupling, Section 3.4), to any numerical method based on volume meshes. The particular case of the coupling with the *cell method*, a technique based on both a primal and a dual volume mesh [83], is illustrated theoretically and through numerical experiments performed with iterative solvers applied to the Schur complement [18, p. 221] of the coupling systems (Trefftz degrees of freedom are eliminated).

Finally, [27] assumes that equation parameters are piecewise constant in the Trefftz domain, which induces a partition: one unbounded subdomain and other bounded, but possibly very large, subdomains, each requiring its own Trefftz discretization space. Hence, coupling strategies are extended to handle more than one Trefftz domain for the case of 2D Helmholtz equation [64, p. 276, Chapter 9].

The coupling between FEM and a Trefftz method has also been addressed before from an engineering perspective [79]. However, a different methodology for the coupling is used in that work: FEM and Trefftz field values, the Dirichlet data, are matched in selected points on the interface between their domains (*collocation method*), while the Neumann data enter through a boundary term of the variational form. The resulting overdetermined system of equations is solved in the least-squares sense.

To the best of our knowledge, apart from these papers, little research has been devoted to the investigation of strategies combining Trefftz methods with conventional finite element methods. We cite [45, 71]: in particular, the coupling proposed in [45, p. 672, Section III] is the same as the DtN-based coupling of Section 3.4.

Remark. *It is also worth mentioning the* infinite element method *[39], primarily used for exterior Helmholtz problems, which employs standard FEM in a bounded domain and* infinite elements *in the unbounded exterior. In fact, given a spherical coordinate system [43, p. 38, Section 1.4.1], the radial component of infinite elements is expressed by a* multipole expansion *[43, p. 151, Section 3.4], which can be used as Trefftz basis functions (see Section 2.2). Conversely, the spherical component is approximated by standard polynomial finite element shape functions [67, p. 143, Section 5.6].*

Infinite elements are then coupled with standard FEM by solving the variational form of the equations everywhere (see Section 1.4): unbounded radial integrals can be computed by choosing a radial dependence that leads to exponential integrals *[2, p. 227, Chapter 5]. The final coupling system may not be symmetric.*

This thesis describes the coupling techniques introduced in [28, 29, 30, 27] for Poisson's (one Trefftz domain) and time-harmonic Maxwell's equations and illustrate all the numerical results reported in these works. Novel results for FEM coupled with more than one Trefftz domain are also included ([27] is confined to 2D Helmholtz).

Having multiple Trefftz domains allows to treat piecewise-constant material parameters on potentially very large regions, while using a minimal volume mesh for the FEM domain. This mesh can be so small that it only surrounds points where the field is singular, like *Triple-Point Singularities* (TPS), which emerge at the junction of three different materials [42]. At the same time, one also needs to impose interface conditions between neighboring Trefftz domains, which requires a mesh on the interfaces separating them.

Furthermore, while mesh-based methods like FEM suffer from the well-known *pollution effect* [9] with time-harmonic Maxwell's equations, oscillating basis

functions are used in the Trefftz domains (see Section 2.2): these basis functions may achieve better approximation properties than the classical piecewise-polynomial spaces of FEM [54].

Outline

Chapter 1 illustrates the boundary value problems discussed in this work. It also provides references to the relevant formalism of functional analysis and, specifically, FEM, one leg of the hybrid strategy we propose. The other leg, Trefftz methods, is more thoroughly described in Chapter 2, where we also present results on the related exponential convergence behavior.

Given these approaches, Chapter 3 describes four algorithms to couple them: one of these strategies is further generalized in Chapter 4, so that it can couple Trefftz methods with any numerical technique based on volume meshes.

Chapter 5 gives some insight into the code that is used for the numerical experiments of this work. The corresponding results are described in Chapter 6, showing the convergence of all coupling approaches with one or more Trefftz domains (that also need to be coupled with each other) and with or without an analytic solution: an example of the latter is when singularities are introduced.

Some remarks in Chapter 7 conclude the work.

1 Preliminaries

This chapter illustrates the boundary value problems and notation behind our description of the coupling approaches between FEM and Trefftz methods. Firstly, the *continuous* setting: the boundary value problems considered in this work (Section 1.1), including time-harmonic Maxwell's equations (Section 1.1.3), the partition of their domain $\mathbb{R}^d$, $d = 2, 3$ (Section 1.2), and the function spaces involved in each subdomain and on the interfaces between them (Section 1.3). Secondly, given all these ingredients, in Section 1.4 we derive the variational (weak) forms of the boundary value problems, which constitute the basis of their discretizations relying on volume meshes, and present the *discrete* finite element spaces used in this work.

1.1 Boundary Value Problems

1.1.1 Poisson's Equation

To derive some theoretical (Section 2.3 and Chapter 3) and numerical results (Sections 2.3.1, 6.1, and 6.2), we refer to the following Poisson's problem:

$$- \nabla \cdot \left[\mathbf{M}_{\mu}^{-1}(\mathbf{x}) \, \nabla u \right] = j \quad \text{in } \mathbb{R}^d, \ d = 2, 3, \tag{1.1a}$$

$$u(\mathbf{x}) = \begin{cases} c \log\|\mathbf{x}\| + \mathcal{O}(\|\mathbf{x}\|^{-1}) & \text{in } \mathbb{R}^2, \ c \in \mathbb{R} \\ \mathcal{O}(\|\mathbf{x}\|^{-1}) & \text{in } \mathbb{R}^3 \end{cases} \quad \text{for } \|\mathbf{x}\| \to \infty \text{ uniformly,} \tag{1.1b}$$

which, in $\mathbb{R}^3$, models an *electrostatic* phenomenon [43, p. 60] through *Gauss's law* [43, p. 182, (4.22)] for the *electric displacement field* [43, p. 182, (4.21)].

- $u \colon \mathbb{R}^d \to \mathbb{C}$, $d = 2, 3$, represents the electric displacement field.

1 Preliminaries

- $\mathbf{M}_\mu\colon\ \mathbb{R}^d \to \mathbb{C}^{d,d}$ is a symmetric, bounded, uniformly positive-definite matrix that corresponds to an inhomogeneous, anisotropic *permeability* [43, p. 285, (6.32)]. We assume that $\mathbf{M}_\mu(\mathbf{x}) = \mu\,\mathbf{I}\ \ \forall \mathbf{x} \in \mathbb{R}^d \setminus \Omega_\star$, given a bounded domain $\Omega_\star \subset \mathbb{R}^d$, and $\mu \in \mathbb{C}$ *constant everywhere* in $\mathbb{R}^d \setminus \Omega_\star$.

- $j\colon \mathbb{R}^d \to \mathbb{C}$ represents the stationary current that generates the electromagnetic field. j has compact support in $\Omega_\star$.

- The decay condition (1.1b) follows from [64, p. 259, Theorem 8.9].

1.1.2 Helmholtz Equation

The numerical results in Sections 2.3.2 and 6.3 are obtained for the reference 2D Helmholtz problem

$$-\nabla \cdot \left[\mathbf{M}_\mu^{-1}(\mathbf{x})\,\nabla u\right] - \omega^2 \epsilon(\mathbf{x})\,u = j \quad \text{in } \mathbb{R}^2, \tag{1.2a}$$

$$\nabla u \cdot \mathbf{x} - \imath k \|\mathbf{x}\| u = 0 \quad \text{for } \|\mathbf{x}\| \to \infty \text{ uniformly}, \tag{1.2b}$$

which models the scattering of transverse-electric polarized z-invariant time-harmonic electromagnetic waves at penetrable objects [43, p. 427, (9.181)].

- $u\colon\ \mathbb{R}^2 \to \mathbb{C}$ represents the longitudinal (z-)component of a *magnetic vector potential* [43, p. 243, (5.61)]

- $\mathbf{M}_\mu\colon \mathbb{R}^2 \to \mathbb{C}^{2,2}$ is the same permeability of Section 1.1.1, while $\epsilon\colon \mathbb{R}^2 \to \mathbb{C}$ represents an inhomogeneous *permittivity* [43, p. 186, (4.33)]. We again assume that $\mathbf{M}_\mu(\mathbf{x}) = \mu\,\mathbf{I}\ \ \forall \mathbf{x} \in \mathbb{R}^2 \setminus \Omega_\star$, given a bounded domain $\Omega_\star \subset \mathbb{R}^2$, but this time $\mu, \epsilon \in \mathbb{C}$ are *piecewise constant* in $\mathbb{R}^2 \setminus \Omega_\star$.

- $\omega \in \mathbb{R}$ is the *angular frequency* [43, p. 386, (9.11)], while $k := \omega\sqrt{\mu\epsilon}$ the piecewise-constant *wavenumber* [43, p. 385, Section 9.1.2] in $\mathbb{R}^2 \setminus \Omega_\star$.

- $j\colon \mathbb{R}^2 \to \mathbb{C}$ is the same stationary current of Section 1.1.1.

- (1.2b) is the *Sommerfeld radiation condition*; please refer to [32, p. 19, Definition 2.4].

1.1.3 Maxwell's Equations

We now consider the following second-order vector boundary value problem
for numerical results in Sections 2.4 and 6.6:

$$
\begin{cases}
\nabla \times \left[\mathbf{M}_\mu^{-1}(\mathbf{x}) \, \nabla \times \mathbf{u} \right] - \omega^2 \mathbf{M}_\epsilon(\mathbf{x}) \, \mathbf{u} + \nabla \phi = \mathbf{j} \\
\hspace{10em} \nabla \cdot \mathbf{u} = 0
\end{cases}
\quad \text{in } \mathbb{R}^3, \tag{1.3a}
$$

$$
\nabla \times \mathbf{u} \times \mathbf{x} - \imath k \|\mathbf{x}\| \mathbf{u} = \mathbf{0} \quad \text{for } \|\mathbf{x}\| \to \infty \text{ uniformly,} \tag{1.3b}
$$

which models time-harmonic Maxwell's equations [43, p. 233, (5.56)] expressed
in terms of a magnetic vector potential subject to the *Coulomb gauge* [43,
p. 440, (10.8)].

- $\mathbf{u} \colon \mathbb{R}^3 \to \mathbb{C}^3$ represents the magnetic vector potential.

- $\phi \colon \mathbb{R}^3 \to \mathbb{C}$ represents the *electric scalar potential* [43, p. 79, (2.23)],
  which also acts as a Lagrange multiplier to impose the Coulomb gauge.
  ϕ must be subject to a further constrain such that it is uniquely defined
  by (1.3a). In the scope of this work, we set $\int_{\mathbb{R}^3} \phi \, \mathrm{d}\mathbf{x} = 0$.

- $\mathbf{M}_\mu, \mathbf{M}_\epsilon \colon \mathbb{R}^3 \to \mathbb{C}^{3,3}$ are symmetric, bounded, uniformly positive-definite
  matrices that correspond to an inhomogeneous, anisotropic permeability
  and permittivity, respectively. We assume that both $\mathbf{M}_\mu(\mathbf{x}) = \mu\,\mathbf{I}$ and
  $\mathbf{M}_\epsilon(\mathbf{x}) = \epsilon\,\mathbf{I} \quad \forall \mathbf{x} \in \mathbb{R}^3 \setminus \Omega_\star$, given a bounded domain $\Omega_\star \subset \mathbb{R}^3$, and
  $\mu, \epsilon \in \mathbb{C}$ are piecewise constant in $\mathbb{R}^3 \setminus \Omega_\star$.

- $\omega \in \mathbb{R}$ and $k \coloneqq \omega \sqrt{\mu\epsilon}$ are the same constant angular frequency and
  piecewise-constant wavenumber (in $\mathbb{R}^3 \setminus \Omega_\star$) of Section 1.1.2.

- $\mathbf{j} \colon \mathbb{R}^3 \to \mathbb{C}^3$, with $\nabla \cdot \mathbf{j} = 0$, represents the stationary current that
  generates the electromagnetic field. $\mathbf{j}$ has compact support in $\Omega_\star$.

- (1.3b) is the *Silver-Müller radiation condition*; please refer to [32, p. 195,
  Definition 6.6].

It is implicitly assumed that $k \neq 0$; otherwise, if, e.g., $\omega = 0$, we would be in a
magnetostatic regime [43, p. 241, Section 5.3.4] – see Section 6.4. In this case,

the Silver-Müller radiation condition would be replaced by the decay condition [57, p. 180, (5.28)]

$$\mathbf{u}(\mathbf{x}) = \mathcal{O}(\|\mathbf{x}\|^{-1}) \quad \text{for } \|\mathbf{x}\| \to \infty \text{ uniformly.} \tag{1.4}$$

1.1.4 Eddy-Current Model

Here we consider a special case of Section 1.1.3, i.e. a *magnetoquasistatic* [55] reduced *eddy-current* [43, p. 310] model obtained from Maxwell's equations. We use the **H**-Φ formulation [63], which employs the **H**-field [43, p. 279, Section 6.3] in electrically-conductive [43, p. 296] domains Ω^{c} ($\equiv \Omega_\star$ from Section 1.1.3) and a *magnetic scalar potential* Φ (see Remark 1.2.1 in the next section) in nonconductive domains Ω^{n}. This form typically requires to know the source magnetic field $\mathbf{H}_{\mathrm{s}}$ before simulating and has difficulties with a multiply-connected Ω^{c} (see Remark 1.2.1).

J. Smajic in [78] proposes a new **H**-Φ field formulation on a multiply-connected domain not requiring to precompute the $\mathbf{H}_{\mathrm{s}}$-field before the actual simulation. Here we present another formulation with the same property and later solve it by coupling FEM and Trefftz methods.

Indeed, let us consider the same eddy-current boundary value problem as in [78], but on an unbounded domain $\Omega^{\mathrm{n}} \coloneqq \Omega_+ \setminus \Omega^{\mathrm{c}}$, where Ω_+ designates the first octant of $\mathbb{R}^3$ (all axes with positive directions). The reason for the octant is that we treat XY, XZ, and YZ as symmetry planes of our model, where we impose boundary conditions.

$$\begin{cases} \nabla \times \left(\sigma^{-1}\nabla \times \mathbf{H}\right) + \imath\omega\mu_{\mathrm{c}}\,\mathbf{H} = \mathbf{0} & \text{in } \Omega^{\mathrm{c}} \\ \mathbf{n} \times \nabla \times \mathbf{H} = \mathbf{0} & \text{on } \partial_{\mathrm{N}}\Omega^{\mathrm{c}} \\ \mathbf{n} \times \mathbf{H} = \mathbf{0} & \text{on } \partial_{\mathrm{D}}\Omega^{\mathrm{c}} \\ \mathbf{H} = \nabla\Phi, \ \ \nabla \cdot (\mu_{\mathrm{n}}\nabla\Phi) = 0 & \text{in } \Omega^{\mathrm{n}} \\ \mathbf{n} \cdot \mu_{\mathrm{n}}\nabla\Phi = 0 & \text{on } \partial_{\mathrm{N}}\Omega^{\mathrm{n}} \\ \Phi = I/2 & \text{on } \partial_{\mathrm{D}1}\Omega^{\mathrm{n}} \\ \Phi = 0 & \text{on } \partial_{\mathrm{D}2}\Omega^{\mathrm{n}} \\ \Phi \text{ is const on } \partial_{\mathrm{D}3}\Omega^{\mathrm{n}} \end{cases} \tag{1.5}$$

Φ on $\partial_{\mathrm{D3}}\Omega^{\mathrm{n}}$ is a constant potential that has to be determined. For Φ at infinity we aim at the same behavior as (1.4).

We assume that the bounded conductive domain Ω^{c} lies inside Ω_{f}, $\Omega^{\mathrm{c}} \subseteq \Omega_{\mathrm{f}}$, similarly to $\Omega_{\star}$ in Section 1.2. Hence, given Lemma 1.3.1, interface conditions between Ω^{c} and Ω^{n} (*inside* Ω_{f}) are required for the field to be well-posed:

$$
\begin{cases}
\mathbf{n} \times \mathbf{H} = \mathbf{n} \times \nabla\Phi \\
\mu_{\mathrm{c}}\, \mathbf{n} \cdot \mathbf{H} = \mu_{\mathrm{n}}\, \mathbf{n} \cdot \nabla\Phi
\end{cases}
\quad \text{on } \partial_{\mathrm{cn}}\Omega^{\mathrm{c}}.
\tag{1.6a}
$$

(1.6a) should be imposed together with the other interface conditions between the FEM and Trefftz domains, also derived from Lemma 1.3.1:

$$
\begin{cases}
\Phi_{\mathrm{f}} = \Phi_{\mathrm{m}} \\
\mathbf{n} \cdot \nabla\Phi_{\mathrm{f}} = \mathbf{n} \cdot \nabla\Phi_{\mathrm{m}}
\end{cases}
\quad \text{on } \Gamma,
\tag{1.6b}
$$

with Γ lying inside Ω^{n}.

We will solve this problem in Section 6.5, where a geometric model of Ω^{c}, Ω^{n}, and their boundary conditions is provided.

1.2 Domain Decomposition

For Sections 1.1.2 and 1.1.3, piecewise-constant μ, ϵ in $\mathbb{R}^d \setminus \Omega_{\star}$, $d = 2, 3$, induce a natural partition of $\mathbb{R}^d \setminus \Omega_{\star}$ into $m+1$ subdomains Ω_i, $i = 0, \ldots, m$, such that the pair $(\mu, \epsilon) \in \mathbb{C}^2$ (and therefore the wavenumber k) is constant in each Ω_i. We denote the constant wavenumber in each subdomain with k_i, $i = 0, \ldots, m$, and assume that there is only one unbounded domain in this partition, which we refer to as Ω_0.

To simplify the exposition and without loss of generality, from now on we assume that $m = 1$ for Sections 1.1.2 and 1.1.3, i.e. that $\Omega_0 \cup \Omega_1 = \mathbb{R}^d \setminus \Omega_{\star}$, with constant $k_0 \in \mathbb{C}$ in the unbounded domain Ω_0 and constant $k_1 \in \mathbb{C}$ in the bounded Ω_1. Generalization to $m > 1$ is immediate. For Section 1.1.1, the simpler case $m = 0$ (one unbounded domain) holds.

(a) Sample domains $\Omega_\star$, Ω_0, and Ω_1.   (b) Sample domains Ω_f, Ω_m^0, and Ω_m^1.
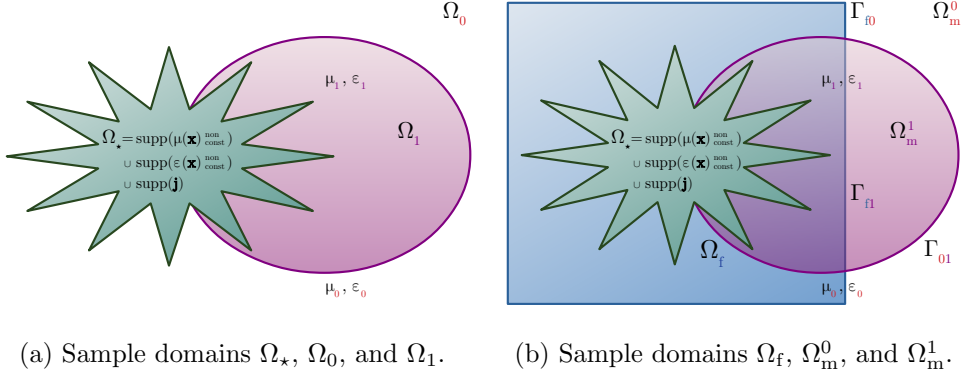
Figure 1.1: Physical domains (Figure 1.1a) do not necessarily correspond to computational domains (Figure 1.1b): Γ_{f0}, Γ_{f1} can be artificial interfaces. Different colors in the (left) figure represent regions with different parameters μ, ϵ.

However, for our computations we introduce a different domain decomposition. As a matter of fact, we do not necessarily have to couple FEM and Trefftz methods across physical interfaces that coincide with discontinuities of parameters μ, ϵ. Hence, instead of considering the physical domains $\Omega_\star, \Omega_0, \Omega_1$ (see Figure 1.1a), we take a different partition for computations (see Figure 1.1b):

$$\mathbb{R}^d = \Omega_f \cup \Omega_m^0 \cup \Omega_m^1 \cup \Gamma_{f0} \cup \Gamma_{f1} \cup \Gamma_{01}, \tag{1.7}$$

with $\Gamma_{f0} := \partial\Omega_f \cap \partial\Omega_m^0$, $\Gamma_{f1} := \partial\Omega_f \cap \partial\Omega_m^1$, $\Gamma_{01} := \partial\Omega_m^0 \cap \partial\Omega_m^1$ and $\Omega_f \cap \Omega_m^0 = \varnothing$, $\Omega_f \cap \Omega_m^1 = \varnothing$, $\Omega_m^0 \cap \Omega_m^1 = \varnothing$. We also define $\Omega_m := \Omega_m^0 \cup \Omega_m^1$ and $\Gamma := \Gamma_{f0} \cup \Gamma_{f1} \cup \Gamma_{01}$; for Section 1.1.1, $\Omega_m = \Omega_m^0$ and $\Gamma = \Gamma_{f0} = \partial\Omega_f = \partial\Omega_m$.

We demand $\Omega_\star \subseteq \Omega_f$, but not necessarily $\Omega_\star = \Omega_f$. If $\Omega_\star \neq \Omega_f$, $\Gamma_{f0} \cup \Gamma_{f1} = \partial\Omega_f$ is an artificial interface. Note that Ω_f can be composed of disjoint regions.

We also demand that Ω_m^0, Ω_m^1 include different values of the equation parameters of (1.3a): $\Omega_m^i \subseteq \Omega_i$, $i = 0, 1$, i.e. constant wavenumbers k_0, k_1 for Ω_m^0, Ω_m^1.

We call Ω_f, a bounded Lipschitz domain [41, p. 4, Definition 1.1], the *FEM domain*, whereas Ω_m^0 is the unbounded and Ω_m^1 the bounded *Trefftz domain*. The terminology indicates the type of approximation of the unknown to be

employed in each domain. Coupling between the FEM and Trefftz domains is done across the (artificial) interfaces $\Gamma_{\mathrm{f}i}$, $i = 0, 1$, while coupling between the two Trefftz domains occurs across the physical interface Γ_{01} (not required for Poisson's problem of Section 1.1.1).

Remark 1.2.1. *A special setting occurs when $k_i = 0$ and Ω_{m}^i is also* simply connected *[37, p. 252, Section 8]. As a matter of fact, as Ω_{m}^i does not contain any free current by definition ($\Omega_{\star} \subseteq \Omega_{\mathrm{f}}$), then we can replace Maxwell's equations* (1.3a) *for $k = 0$ in Ω_{m}^i with the Poisson's problem* (1.1) *using a* magnetic scalar potential *[43, p. 245, (5.67)] (see Section 1.1.4) as unknown, which is easier to handle (see Sections 4.4 and 6.5).*

1.3 Function Spaces

We look for unknowns u (Sections 1.1.1 and 1.1.2) and $\phi, \mathbf{u}$ (Section 1.1.3) in *Sobolev spaces* [67, p. 36, Chapter 3] on a generic open set $\Omega \subseteq \mathbb{R}^d$, $d = 2, 3$:

- $H^1(\Omega)$ [67, p. 38] for u and $H_*^1(\Omega) := \left\{ v \in H^1(\Omega) \colon \int_{\Omega} v \, \mathrm{d}\mathbf{x} = 0 \right\}$ for ϕ, and

- $\mathbf{H}(\mathbf{curl}, \Omega)$ [67, p. 55, (3.40)] and the broader $\mathbf{H}_{\mathrm{loc}}(\mathbf{curl}, \Omega)$ for $\mathbf{u}$: the subscript "loc" indicates that functions belong to the reported space, here $\mathbf{H}(\mathbf{curl}, \Omega)$, after multiplication with a compactly-supported smooth function [67, p. 230].

In the following we will also make use of Sobolev spaces $L^2(\Omega)$ [67, p. 36, Section 3.2], $L_t^2(\partial\Omega)$ [67, p. 48, (3.13)], and $H(\mathrm{div}, \Omega)$ [67, p. 52, (3.29)].

Given these spaces and the computational domains introduced in Section 1.2, for Sections 1.1.2 and 1.1.3 we can decompose $u, \phi, \mathbf{u}$ as

$$u_{\mathrm{f}} := u|_{\Omega_{\mathrm{f}}} \in H^1(\Omega_{\mathrm{f}}), \qquad u_{\mathrm{m}}^0 := u|_{\Omega_{\mathrm{m}}^0} \in H_{\mathrm{loc}}^1(\Omega_{\mathrm{m}}^0), \qquad u_{\mathrm{m}}^1 := u|_{\Omega_{\mathrm{m}}^1} \in H^1(\Omega_{\mathrm{m}}^1),$$
$$\tag{1.8a}$$

$$\phi_{\mathrm{f}} := \phi|_{\Omega_{\mathrm{f}}} \in H_*^1(\Omega_{\mathrm{f}}), \qquad \phi_{\mathrm{m}}^0 := \phi|_{\Omega_{\mathrm{m}}^0} \in H_{*,\mathrm{loc}}^1(\Omega_{\mathrm{m}}^0), \qquad \phi_{\mathrm{m}}^1 := \phi|_{\Omega_{\mathrm{m}}^1} \in H_*^1(\Omega_{\mathrm{m}}^1),$$
$$\tag{1.8b}$$

$$\mathbf{u}_{\mathrm{f}} := \mathbf{u}|_{\Omega_{\mathrm{f}}} \in \mathbf{H}(\mathbf{curl}, \Omega_{\mathrm{f}}), \mathbf{u}_{\mathrm{m}}^0 := \mathbf{u}|_{\Omega_{\mathrm{m}}^0} \in \mathbf{H}_{\mathrm{loc}}(\mathbf{curl}, \Omega_{\mathrm{m}}^0), \mathbf{u}_{\mathrm{m}}^1 := \mathbf{u}|_{\Omega_{\mathrm{m}}^1} \in \mathbf{H}(\mathbf{curl}, \Omega_{\mathrm{m}}^1).$$
$$\tag{1.8c}$$

1 Preliminaries

For Section 1.1.1, the decomposition (1.8a) is only on domains Ω_{f} and $\Omega_{\mathrm{m}} = \Omega_{\mathrm{m}}^0$.

It is now important to introduce a formalism to evaluate $u, \phi, \mathbf{u}$ on the interfaces $\Gamma_{\mathrm{f}0}, \Gamma_{\mathrm{f}1}, \Gamma_{01}$ between $\Omega_{\mathrm{f}}, \Omega_{\mathrm{m}}^0, \Omega_{\mathrm{m}}^1$. The relevant *traces* [67, p. 42, Section 3.2.1] are

- the *Dirichlet trace* [67, p. 43, (3.8)],

- the *Neumann trace* γ_{N} [75, p. 68, (2.103)]:

$$
\gamma_{\mathrm{N}} : \begin{cases} H^1_{\mathrm{loc}}(\nabla^2, \Omega_{\square}) \to \widetilde{H}^{-\frac{1}{2}}(\Gamma_{\square}), \\ v \mapsto \mathbf{n} \cdot \mathbf{M}_{\mu}^{-1} \nabla v \ \ \text{for} \ \ v \in H^2_{\mathrm{loc}}(\Omega_{\square}), \end{cases} \tag{1.9a}
$$

- the *tangential trace* [67, p. 57, (3.45)],

- the *tangential components trace* [67, p. 57, (3.46)], and

- the *magnetic trace* $\boldsymbol{\gamma}_{\mathrm{m}}$ [67, p. 59, (3.51)]:

$$
\boldsymbol{\gamma}_{\mathrm{m}} : \begin{cases} \mathbf{H}_{\mathrm{loc}}(\mathbf{curl\,curl}, \Omega_{\square}) \to \widetilde{\mathbf{H}}^{-\frac{1}{2}}(\mathrm{div}_{\Gamma_{\square}}, \Gamma_{\square}), \\ \mathbf{v} \mapsto \mathbf{n} \times \left(\mathbf{M}_{\mu}^{-1} \nabla \times \mathbf{v} \right). \end{cases} \tag{1.9b}
$$

We define the terms appearing in (1.9a) and (1.9b):

- $\Omega_{\square} \in \left\{ \Omega_{\mathrm{f}}, \Omega_{\mathrm{m}}^0, \Omega_{\mathrm{m}}^1 \right\}$ and $\Gamma_{\square} \in \{ \Gamma_{\mathrm{f}0}, \Gamma_{\mathrm{f}1}, \Gamma_{01} \}$.

- $\mathbf{n}$ is the normal vector on $\Gamma_{\square}$.

- $H^1_{\mathrm{loc}}(\nabla^2, \Omega_{\square})$ is the space of functions $v \in H^1_{\mathrm{loc}}(\Omega_{\square})$ for which $\nabla^2 v \in L^2_{\mathrm{loc}}(\Omega_{\square})$.

- $\widetilde{H}^{-\frac{1}{2}}(\Gamma_{\square})$ [67, p. 44] is the *dual space* [67, p. 19, Definition 2.14] of $H^{\frac{1}{2}}(\Gamma_{\square})$ [67, p. 44], given by the range of Dirichlet traces. The tilde of $\widetilde{H}^{-\frac{1}{2}}(\Gamma_{\square})$ takes into account that $\Gamma_{\square}$ is generally an open interface [75, p. 59, (2.90)].

- $\mathbf{H}_{\mathrm{loc}}(\mathbf{curl\,curl}, \Omega_{\square})$ is the space of functions $\mathbf{v} \in \mathbf{H}_{\mathrm{loc}}(\mathbf{curl}, \Omega_{\square})$ for which $\nabla \times (\nabla \times \mathbf{v}) \in \mathbf{L}^2_{\mathrm{loc}}(\Omega_{\square}) \coloneqq \left[L^2_{\mathrm{loc}}(\Omega) \right]^3$.

- $\widetilde{\mathbf{H}}^{-\frac{1}{2}}(\text{div}_{\Gamma_\square}, \Gamma_\square)$ [67, p. 59] is the dual space of $\mathbf{H}^{-\frac{1}{2}}(\mathbf{curl}_{\Gamma_\square}, \Gamma_\square)$ [67, p. 59, (3.53)].

Relying on this formalism, we can then write the *interface conditions* that the restrictions of the solution of a generic boundary value problem on two different domains Ω_1, Ω_2 have to satisfy across the common interface $\Gamma := \overline{\Omega}_1 \cap \overline{\Omega}_2$ for the joint solution to be well-posed. They are given by [67, p. 107, Lemma 5.3], which we report here, given the importance of these conditions for our work:

Lemma 1.3.1. *Let Ω_1, Ω_2 be nonoverlapping Lipschitz domains [67, p. 38, Definition 3.1] with a common surface $\Gamma := \overline{\Omega}_1 \cap \overline{\Omega}_2$ with nonzero measure.*

- *Given $u_1 := u|_{\Omega_1} \in H^1(\Omega_1)$, $u_2 := u|_{\Omega_2} \in H^1(\Omega_2)$, and $u \in L^2(\Omega_1 \cup \Omega_2 \cup \Gamma)$, then:*

$$u_1\big|_\Gamma = u_2\big|_\Gamma \Longrightarrow u \in H^1(\Omega_1 \cup \Omega_2 \cup \Gamma).$$

- *Given $\mathbf{u}_1 := \mathbf{u}|_{\Omega_1} \in \mathbf{H}(\mathbf{curl}, \Omega_1)$, $\mathbf{u}_2 := \mathbf{u}|_{\Omega_2} \in \mathbf{H}(\mathbf{curl}, \Omega_2)$, and $\mathbf{u} \in \mathbf{L}^2(\Omega_1 \cup \Omega_2 \cup \Gamma)$, then:*

$$\mathbf{n} \times \mathbf{u}_1\big|_\Gamma = \mathbf{n} \times \mathbf{u}_2\big|_\Gamma \Longrightarrow \mathbf{u} \in \mathbf{H}(\mathbf{curl}, \Omega_1 \cup \Omega_2 \cup \Gamma).$$

- *Given $\mathbf{u}_1 := \mathbf{u}|_{\Omega_1} \in H(\text{div}, \Omega_1)$, $\mathbf{u}_2 := \mathbf{u}|_{\Omega_2} \in H(\text{div}, \Omega_2)$, and $\mathbf{u} \in \mathbf{L}^2(\Omega_1 \cup \Omega_2 \cup \Gamma)$, then:*

$$\mathbf{n} \cdot \mathbf{u}_1\big|_\Gamma = \mathbf{n} \cdot \mathbf{u}_2\big|_\Gamma \Longrightarrow \mathbf{u} \in H(\text{div}, \Omega_1 \cup \Omega_2 \cup \Gamma).$$

Hence, for Poisson's problem (1.1), interface conditions between $u_\text{f} := u|_{\Omega_\text{f}} \in H^1(\Omega_\text{f})$ and $u_\text{m} := u|_{\Omega_\text{m}} \in H^1_{\text{loc}}(\Omega_\text{m})$, given a single Trefftz domain Ω_m ($m = 0$), with $\Gamma = \partial\Omega_\text{f} = \partial\Omega_\text{m}$, are

$$u_\text{f}|_\Gamma = u_\text{m}|_\Gamma, \tag{1.10a}$$
$$\gamma_\text{N} u_\text{f}|_\Gamma = \gamma_\text{N} u_\text{m}|_\Gamma. \tag{1.10b}$$

For Helmholtz problem (1.2), interface conditions are the same as (1.10) but for the three interfaces $\Gamma_{\text{f}0}, \Gamma_{\text{f}1}, \Gamma_{01}$ between $\Omega_\text{f}, \Omega_\text{m}^0, \Omega_\text{m}^1$:

$$u_\text{f}|_{\Gamma_{\text{f}i}} = u_\text{m}^i\big|_{\Gamma_{\text{f}i}}, \tag{1.11a}$$

9

$$\gamma_{\mathrm N}u_{\mathrm f}\big|_{\Gamma_{\mathrm f i}} = \gamma_{\mathrm N}u_{\mathrm m}^{i}\big|_{\Gamma_{\mathrm f i}}, \tag{1.11b}$$

with $i = 0, 1$. Analogous conditions also have to hold across Γ_{01}.

Finally, the interface conditions that the solution $\mathbf{u}$ of (1.3) has to satisfy across $\Gamma_{\mathrm f i}$, $i = 0, 1$, are

$$\mathbf{n} \times \mathbf{u}_{\mathrm f}\big|_{\Gamma_{\mathrm f i}} = \mathbf{n} \times \mathbf{u}_{\mathrm m}^{i}\big|_{\Gamma_{\mathrm f i}}, \tag{1.12a}$$

$$\boldsymbol{\gamma}_{\mathrm m}\mathbf{u}_{\mathrm f}\big|_{\Gamma_{\mathrm f i}} = \boldsymbol{\gamma}_{\mathrm m}\mathbf{u}_{\mathrm m}^{i}\big|_{\Gamma_{\mathrm f i}}, \tag{1.12b}$$

$$\mathbf{n} \cdot \mathbf{u}_{\mathrm f}\big|_{\Gamma_{\mathrm f i}} = \mathbf{n} \cdot \mathbf{u}_{\mathrm m}^{i}\big|_{\Gamma_{\mathrm f i}}. \tag{1.12c}$$

(1.12a) and (1.12b) stem from the first line of (1.3a), (1.12c) from the second line (Coulomb gauge).[1] Analogous conditions also have to hold across Γ_{01}.

1.4 Finite Elements

Integrating Maxwell's equations over any volumes and surfaces in $\mathbb{R}^d$, $d = 2, 3$, and exploiting the divergence [43, p. 31, (1.56)] or Stokes' theorems [43, p. 34, (1.57)], one obtains the *integral (weak) form* of Maxwell's equations [43, p. 342, Section 7.3.6]. This form, involving fluxes and line integrals, is considered by some [83] to be more "physical" than the corresponding differential form [43, p. 341, (7.56)], as it involves directly measurable quantities, like currents, allows more relaxed smoothness requirements for the unknowns (which can be smooth almost everywhere), and also encodes conservation of energy. For these reasons, Maxwell's equations in integral form constitute the basis of the *cell method* [84].

On a similar note, a finite element analysis always starts from the *variational form* of the differential equations involved. By testing the integral form of (1.1a) on $\Omega_{\mathrm f}$ with suitable functions and integrating by parts, we obtain

Seek $u_{\mathrm f} \in H^1(\Omega_{\mathrm f})$:

$$\int_{\Omega_{\mathrm f}} \left(\mathbf{M}_\mu^{-1}\nabla u_{\mathrm f}\right) \cdot \nabla v_{\mathrm f}\,\mathrm d\mathbf{x} - \int_{\Gamma} \gamma_{\mathrm N}u_{\mathrm f}\,v_{\mathrm f}\,\mathrm dS = \int_{\Omega_{\mathrm f}} j\,v_{\mathrm f}\,\mathrm d\mathbf{x} \quad \forall v_{\mathrm f} \in H^1(\Omega_{\mathrm f}). \tag{1.13a}$$

---

[1] At first sight, one could think of combining (1.12a) and (1.12c) and impose the continuity $\mathbf{u}_{\mathrm f}\big|_{\Gamma_{\mathrm f i}} = \mathbf{u}_{\mathrm m}^{i}\big|_{\Gamma_{\mathrm f i}}$, $i = 0, 1$. However, this would only hold if each restriction of $\mathbf{u}$ lay in $\mathbf{H}^1(\Omega_\square) \coloneqq \left[H^1(\Omega_\square)\right]^3$.

Let us also introduce the variational form for Maxwell's PDEs (1.3a):

Seek $\mathbf{u}_f \in \mathbf{H}(\mathbf{curl}, \Omega_f)$, $\phi_f \in H^1_*(\Omega_f)$:

$$
\begin{cases}
\int_{\Omega_f} \left[\left(\mathbf{M}_\mu^{-1} \nabla \times \mathbf{u}_f \right) \cdot (\nabla \times \mathbf{v}_f) - \omega^2 \left(\mathbf{M}_\epsilon \mathbf{u}_f \right) \cdot \mathbf{v}_f \right] \, d\mathbf{x} + \\
\sum_{i=0,1} \int_{\Gamma_{fi}} \boldsymbol{\gamma}_m \mathbf{u}_f^i \cdot \mathbf{v}_f \, dS + \int_{\Omega_f} \nabla \phi_f \cdot \mathbf{v}_f \, d\mathbf{x} = \int_{\Omega_f} \mathbf{j} \cdot \mathbf{v}_f \, d\mathbf{x} \quad \forall \mathbf{v}_f \in \mathbf{H}(\mathbf{curl}, \Omega_f), \\
\int_{\Omega_f} \mathbf{u}_f \cdot \nabla \psi_f \, d\mathbf{x} - \sum_{i=0,1} \int_{\Gamma_{fi}} \left(\mathbf{n} \cdot \mathbf{u}_f^i \right) \psi_f \, dS = 0 \qquad\qquad \forall \psi_f \in H^1_*(\Omega_f).
\end{cases}
$$
$$(1.13b)$$

We use standard *finite element spaces* to discretize (1.13a) and (1.13b) in $\Omega_f \supseteq \Omega_\star$, where $\mathbf{M}_\mu, \mathbf{M}_\epsilon$ may vary in space. These discrete spaces are built on *triangular* [18, p. 65, Section 5.6] (in $\mathbb{R}^2$) or *tetrahedral meshes* $\mathcal{M}_f$ [67, p. 112, Section 5.3] on Ω_f. More specifically, we discretize $u_f \in H^1(\Omega_f)$ and $\phi_f \in H^1_*(\Omega_f)$ with piecewise-linear Lagrangian finite elements [67, p. 143, Section 5.6], i.e.

$$
V^n(\mathcal{M}_f) := \mathcal{S}^0_1(\mathcal{M}_f) := \Big\{ v^n \in C^0(\Omega_f) \colon \; v^n|_K (\mathbf{x}) = a_K + \mathbf{b}_K \cdot \mathbf{x},
$$
$$
a_K \in \mathbb{R}, \; \mathbf{b}_K \in \mathbb{R}^d, \; \mathbf{x} \in K \quad \forall K \in \mathcal{M}_f \Big\}, \quad (1.14a)
$$

with $d = 2, 3$ depending on the problem, and $\mathbf{u}_f \in \mathbf{H}(\mathbf{curl}, \Omega_f)$ with the lowest-order $\mathbf{H}(\mathbf{curl}, \Omega_f)$-conforming edge elements of the first family due to Nédélec [67, p. 126, Section 5.5], i.e.

$$
\mathbf{V}^n(\mathcal{M}_f) := \mathcal{R}^1(\mathcal{M}_f) := \Big\{ \mathbf{v}^n \in \mathbf{H}_0(\mathbf{curl}, \Omega_f) \colon \; \mathbf{v}^n|_K (\mathbf{x}) = \mathbf{a}_K + \mathbf{b}_K \times \mathbf{x},
$$
$$
\mathbf{a}_K, \mathbf{b}_K \in \mathbb{R}^3, \; \mathbf{x} \in K \quad \forall K \in \mathcal{M}_f \Big\}. \quad (1.14b)
$$

On each discrete function $\phi_f^n \in H^1_*(\Omega_f)$ discretized by $V^n(\mathcal{M}_f) \subset H^1(\Omega_f)$ we impose the condition $\int_{\Omega_f} \phi_f^n \, d\mathbf{x} = 0$ by means of a scalar Lagrange multiplier [18, p. 129].

(1.13a) and (1.13b) are used in Chapter 3 to describe the strategies to couple FEM with Trefftz methods.

2 Trefftz Methods

Given the model problems (1.1) and (1.3) and their finite element discretizations (1.13a) and (1.13b) in Ω_f, we introduce here the other leg of our hybrid approach, which is made of *Trefftz methods*. Section 2.1 describes the continuous Trefftz spaces for the boundary value problems of Section 1.1, while Section 2.2 the discrete basis functions that are used by a particular Trefftz method, the *Multiple Multipole Program* (MMP). A theorem for exponential convergence of MMP for Poisson's problem (1.1) in $\mathbb{R}^2$ is proven in Section 2.3: numerical results in Sections 2.3.1 and 2.3.2 agree with this theorem and also show what happens when the hypotheses are no longer true. Section 2.4 only provides empirical evidence for $\mathbb{R}^3$, with considerations about the limitations of Trefftz methods.

2.1 Trefftz Spaces

In the partition of $\mathbb{R}^d \setminus \Omega_\star$, $d = 2, 3$, induced by piecewise-constant equation parameters μ, ϵ and giving rise to the unbounded domain Ω_0 and the (possibly very large) domain Ω_1 (Figure 1.1a), we do not intend to employ mesh-based basis functions, as required in $\Omega_\star$. Indeed, given the computational domains $\Omega_\mathrm{m}^0, \Omega_\mathrm{m}^1$ introduced in Section 1.2, the weak solution $\mathbf{u}_\mathrm{m}^0 \in \mathbf{H}_\mathrm{loc}(\mathbf{curl}, \Omega_\mathrm{m}^0)$ of (1.3) is sought in the *Trefftz space*

$$\mathcal{T}(\Omega_\mathrm{m}^0) := \Big\{ \mathbf{v} \in \mathbf{H}_\mathrm{loc}(\mathbf{curl}, \Omega_\mathrm{m}^0) \colon \ \nabla \times (\nabla \times \mathbf{v}) - k_0^2 \, \mathbf{u} = \mathbf{0} \, , \ k_0 \in \mathbb{C} \, , \quad \nabla \cdot \mathbf{v} = 0 \, ,$$

$$\mathbf{v} \text{ satisfies the radiation condition (1.3b)} \Big\}, \tag{2.1a}$$

which is composed of exact solutions of (1.3) in Ω_m^0. Correspondingly, $\mathbf{u}_\mathrm{m}^1 \in \mathbf{H}(\mathbf{curl}, \Omega_\mathrm{m}^1)$ is sought in

$$\mathcal{T}(\Omega_\mathrm{m}^1) := \Big\{ \mathbf{v} \in \mathbf{H}(\mathbf{curl}, \Omega_\mathrm{m}^1) \colon \quad \nabla \times (\nabla \times \mathbf{v}) - k_1^2 \, \mathbf{u} = \mathbf{0} \, , \ k_1 \in \mathbb{C} \, , \quad \nabla \cdot \mathbf{v} = 0 \Big\}. \tag{2.1b}$$

Similar *scalar* Trefftz spaces $\mathcal{T}$ are needed for u of Poisson's and Helmholtz problems (1.1) and (1.2).

Trefftz methods seek to approximate the unknown in $\Omega_{\mathrm{m}}^0, \Omega_{\mathrm{m}}^1$ using finite-dimensional (discrete) subspaces of $\mathcal{T}(\Omega_{\mathrm{m}}^0), \mathcal{T}(\Omega_{\mathrm{m}}^1)$. When Trefftz methods are used alone, the coefficients of the chosen basis that express the unknown are found by matching either a boundary condition or interface conditions with the basis of another neighboring Trefftz domain. There are several methods to achieve this goal [54]: the most common is arguably *collocation* on selected *matching points* of the hypersurface [46].

However, the main feature that characterizes a Trefftz method is its own discrete Trefftz space, not the way such space is used to solve a problem. Hence, the functional form of the corresponding discrete basis functions leads to different types of Trefftz methods:

- *Plane waves* [43, p. 395, (9.43)] or *(generalized) harmonic polynomials* [66, p. 47, Section 2.4] constitute the most common choice [54].

- If Trefftz basis functions solve an inhomogeneous problem, then we obtain the *method of fundamental solutions* [61].

- Conversely, if they are point sources solving homogeneous equations (the right-hand side can be expressed by a known offset function), then we get the *Method of Auxiliary Sources* (MAS) [86].

In spite of this diversity, all Trefftz methods share a desirable feature and a drawback. The former is the exponential convergence of their approximation error if the field is sufficiently smooth (see Sections 2.3 and 2.4). The drawback is that, as exact solutions of a PDE are global functions and simple choices for a basis of $\mathcal{T}(\Omega_{\mathrm{m}}^0), \mathcal{T}(\Omega_{\mathrm{m}}^1)$ may be affected by near-linear dependence, Trefftz basis functions typically lead to ill-conditioned dense matrices. *Stability* is therefore an issue. Related is the need of heuristic rules to build the discrete Trefftz spaces when the unknown is difficult to model, e.g., when close to singularities: instability can have such a large impact that the numerical solution is not accurate.

The numerical examples of Chapter 6 show that coupling a Trefftz method with FEM can be a way to overcome this issue. These examples rely on

a special case of MAS. Specifically, we use spaces spanned by *multipoles* and refer to this discretization as the MMP approximation after the Trefftz method known as *Multiple Multipole Program.*

2.2 Multiple Multipole Program

The concept of the Multiple Multipole Program was proposed by Ch. Hafner in his dissertation [46] and popularized by his free code `OpenMaXwell` [48] for 2D axisymmetric problems. Hafner's MMP is in turn based on the much older work of G. Mie and I. N. Vekua [65, 85]. Essentially, the Mie-Vekua approach expands some scalar field in a 2D multiply-connected domain [37, p. 252, Section 8] by a *multipole expansion* supplemented with generalized harmonic polynomials. Extending these ideas, MMP introduces more basis functions (*multiple multipoles*) than required according to Vekua's theory [85] to span the Trefftz spaces (2.1).

Multipoles are potentials spawned by (anisotropic) *point sources.* These point sources are taken from the exact solutions of the homogeneous PDEs (1.3a) that can be subject to the decay condition (1.3b), depending on whether they are used to approximate the solution in Ω_{m}^0.

A multipole can generally be written as $v\left(\mathbf{x}\right) \coloneqq f\left(r_{xc}\right) g\left(\theta_{xc}\right)$ or $\mathbf{v}\left(\mathbf{x}\right) \coloneqq f\left(r_{xc}\right) \mathbf{g}\left(\theta_{xc}, \varphi_{xc}\right)$ in a polar/spherical coordinate system in $\mathbb{R}^d$, $d = 2, 3$ ($r \in [0, \infty)$, $\theta \in [0, 2\pi)$, $\varphi \in [0, \pi]$) with respect to its center $\mathbf{c} \in \mathbb{R}^d$ ($\mathbf{x}, \mathbf{c} \in \mathbb{R}^d$ are position vectors in Cartesian coordinates). Here, $\left(r_{xc}, \theta_{xc}\right)^\top$ and $\left(r_{xc}, \theta_{xc}, \varphi_{xc}\right)^\top$ are polar/spherical coordinates of the vector $\mathbf{x}_c \coloneqq \mathbf{x} - \mathbf{c}$.

The radial dependence $f\left(r_{xc}\right)$ has a center that may present a singularity, $|f\left(r\right)| \to \infty$ for $r \to 0$, and, when needed, the desired decay condition at infinity. If there is a singularity, multipoles are centered outside the domain in which they are used for approximation.

On the other hand, the polar/spherical dependence g or $\mathbf{g}$ is usually formulated in terms of trigonometric functions [2, p. 71, Section 4.3] or *(vector) spherical harmonics* [21, p. 289]. The additional constraint of the Coulomb gauge in (1.3a) is taken into account by selecting a subset of vector spherical harmonics to express $\mathbf{g}$.
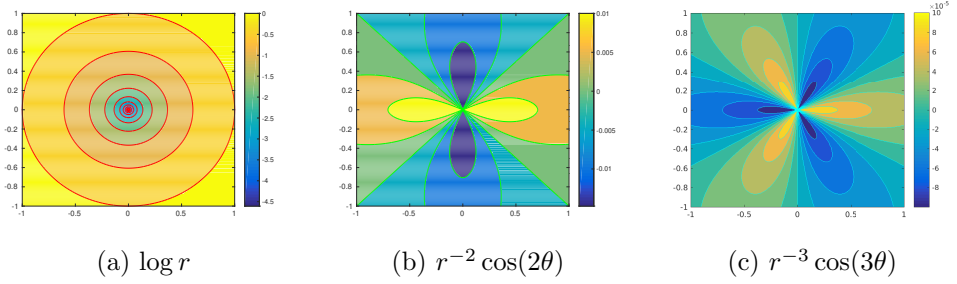
Figure 2.1: Sample multipoles for 2D Poisson's problem.

More specifically, the multipoles chosen for the numerical experiments tackling (1.1) in $\mathbb{R}^d$, $d = 2, 3$, have the forms

$$\text{in } \mathbb{R}^2\colon (r, \theta) \mapsto \begin{cases} \log r_{xc} & \ell = 0, \\ r_{xc}^{-\ell} \cos(\ell\theta_{xc}), & \ell = 1, \dots, \infty, \\ r_{xc}^{-\ell} \sin(\ell\theta_{xc}), & \ell = 1, \dots, \infty, \end{cases} \tag{2.2a}$$

and

$$\text{in } \mathbb{R}^3\colon (r, \theta, \varphi) \mapsto r_{xc}^{-(\ell+1)} Y_{\ell m}(\theta_{xc}, \varphi_{xc}), \quad \ell = 0, \dots, \infty, \quad m = -l, \dots, l. \tag{2.2b}$$

$Y_{lm}(\theta, \varphi)$ denotes the spherical harmonics [64, p. 250]. Figure 2.1 shows three examples of multipoles according to (2.2a) with center $\mathbf{c} = \mathbf{0}$.

Secondly, for the Helmholtz problem (1.2) in $\mathbb{R}^2$:

$$(r, \theta) \mapsto \begin{cases} B_0(kr_{xc}), & B_1(kr_{xc})\cos(\theta_{xc}), & B_1(kr_{xc})\sin(\theta_{xc}), \dots, \\ & B_\ell(kr_{xc})\cos(\ell\,\theta_{xc}), & B_\ell(kr_{xc})\sin(\ell\,\theta_{xc}), \dots \end{cases} \tag{2.3}$$

- B_ℓ is a (non-spherical) Hankel function of the first kind $H_\ell^{(1)}$ [64, p. 280] or a (non-spherical) Bessel function of the first kind J_ℓ [64, p. 278, (9.7)], depending on whether the Trefftz space is subject to the Sommerfeld radiation condition (1.2b).

- $k := \omega\sqrt{\mu\epsilon} \in \mathbb{C}$ is the piecewise-constant wavenumber: $k = k_i$ in Ω_{m}^i, $i = 0, 1$.

We conclude the exposition with multipoles for Maxwell's problem (1.3) in $\mathbb{R}^3$:

$$(r, \theta, \varphi) \mapsto$$

$$\begin{cases} b_\ell(kr_{xc})\, \boldsymbol{\Phi}_{\ell m}(\theta_{xc}, \varphi_{xc}), \\ \ell(\ell+1)\, \dfrac{b_\ell(kr_{xc})}{kr_{xc}}\, \mathbf{Y}_{\ell m}(\theta_{xc}, \varphi_{xc}) + \left[b'_\ell(kr_{xc}) + \dfrac{b_\ell(kr_{xc})}{kr_{xc}} \right] \boldsymbol{\Psi}_{\ell m}(\theta_{xc}, \varphi_{xc}), \\ \ell = 1, \ldots, \infty, \quad m = -l, \ldots, l, \end{cases}$$

$$(2.4)$$

given vector spherical harmonics defined as

$$\mathbf{Y}_{\ell m}(\theta, \varphi) := \mathbf{e}_r\, Y_{\ell m}(\theta, \varphi), \quad \mathbf{e}_r = (1, 0, 0)^\top, \tag{2.5a}$$

$$\boldsymbol{\Phi}_{\ell m}(\theta, \varphi) := \mathbf{r} \times \nabla_{\mathrm{sph}} Y_{\ell m}(\theta, \varphi), \quad \mathbf{r} = (r, 0, 0)^\top, \tag{2.5b}$$

$$\boldsymbol{\Psi}_{\ell m}(\theta, \varphi) := r\, \nabla_{\mathrm{sph}} Y_{\ell m}(\theta, \varphi), \tag{2.5c}$$

here with spherical components.

- b_ℓ is a spherical Hankel function of the first kind $h^{(1)}_\ell$ [64, p. 281] or a spherical Bessel function of the first kind j_ℓ [64, p. 279], depending on whether the Trefftz space is subject to the Silver-Müller radiation condition (1.3b).

- ∇_{sph} denotes the gradient in spherical coordinates. It can be shown that $\boldsymbol{\Phi}_{\ell m}, \boldsymbol{\Psi}_{\ell m}$ do not depend on r despite its presence in their definitions (2.5b) and (2.5c).

However, in a magnetostatic regime ($k = 0$, see Section 1.1.3), multipoles would take the form [29, p. 4, (4)]

$$(r, \theta, \varphi) \mapsto r_{xc}^{-(l+1)}\, \boldsymbol{\Phi}_{\ell m}(\theta_{xc}, \varphi_{xc}), \quad \ell = 1, \ldots, \infty, \quad m = -l, \ldots, l, \tag{2.6}$$

which satisfies the decay condition (1.4).

Remark 2.2.1. *Yet, let us consider the case of a single (unbounded) MMP domain Ω_{m} to solve the magnetostatic problem $\nabla \times (\nabla \times \mathbf{u}) = \mathbf{j}$, $\nabla \cdot \mathbf{u} = 0$ in $\mathbb{R}^3$ subject to the decay condition (1.4) (compare with Section 6.4). If Ω_{m} is multiply connected [37, p. 252, Section 8], then multipoles (2.6) solving the homogeneous problem are not enough for Ampère's law in integral form [43, p. 233, (5.57)] to hold in Ω_{m}.*
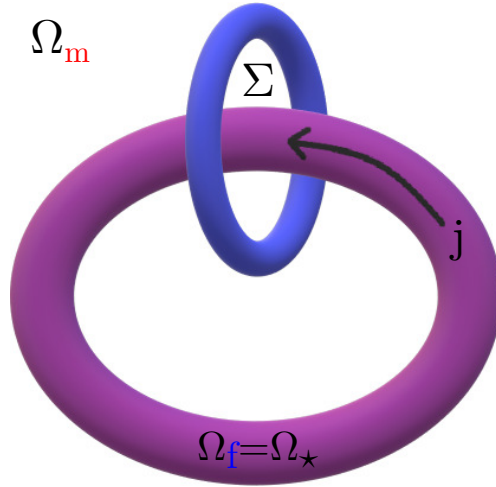
Figure 2.2: A current loop $\Omega_\mathrm{f} = \Omega_\star$, along which $\mathbf{j}$ is tangential, and a closed curve in $\Omega_\mathrm{m} = \mathbb{R}^3 \setminus \Omega_\star$ where to test Ampère's law.

As a matter of fact, let us consider the case when $\Omega_\mathrm{f} = \Omega_\star$ is a torus that contains a current loop along which $\mathbf{j}$ is tangential, which is $\Omega_\star$ (see Figure 2.2). Ampère's law states that the magnetic field $\nabla \times \mathbf{u}$ [43, p. 243, (5.61)] integrated on any closed curve is equal to the current flowing through it; therefore, if one takes a closed curve such that the current loop passes through it (like two links of a chain), we should have

$$\oint (\nabla \times \mathbf{u}_\mathrm{m}) \cdot \mathrm{d}\vec{s} = \int_\Sigma \mathbf{j} \cdot \mathrm{d}S, \tag{2.7a}$$

where Σ is the surface bounded by the closed curve. However, on any closed curve in Ω_m, including those through which the torus Ω_f passes, given $\mathbf{u}_\mathrm{m}$ linear combination of multipoles (2.6), we always have

$$\oint (\nabla \times \mathbf{u}_\mathrm{m}) \cdot \mathrm{d}\vec{s} = \int_\Sigma [\nabla \times (\nabla \times \mathbf{u}_\mathrm{m})] \cdot \mathrm{d}S = 0, \tag{2.7b}$$

where the first step follows from Stokes' theorem [43, p. 34, (1.57)].

To address this issue, one should complete (2.6) with a known offset function being the solution of the inhomogeneous magnetostatic problem in free space, i.e. Biot–Savart law [43, p. 224, (5.34) and p. 227, (5.42)].

Each multipole from (2.2a), (2.2b), (2.3), (2.4), and (2.6) is characterized by a location, i.e. its center $\mathbf{c}$, and parameters ℓ (degree) and, optionally, m (subdegree). When we place several multipoles at a given location up to a certain order, which is the maximum degree of multipoles with that center, we use the term *multipole expansion*. Summing the number of terms of all multipole expansions used for approximation yields the total number of degrees of freedom of the discretized Trefftz spaces $\boldsymbol{\mathcal{T}}^n(\Omega_{\mathrm{m}}^i) \subset \boldsymbol{\mathcal{T}}(\Omega_{\mathrm{m}}^i)$, $i = 0, 1$.

2.3 Trefftz Approximation Error in 2D

Let the solution u of the Poisson's problem (1.1) in $\mathbb{R}^2$ allow an analytic extension beyond an MMP domain $\Omega_{\mathrm{m}} \in \mathbb{R}^2$, into the region of $\Omega_{\mathrm{m}}^{\mathsf{c}} := \mathbb{R}^2 \setminus \Omega_{\mathrm{m}}$ between $\Gamma := \partial\Omega_{\mathrm{m}}$ and the curve Σ along which the multipole expansions are placed. Then we expect exponential convergence of MMP in terms of its number of degrees of freedom, both when the number of multipole expansions and the order of the expansions is raised. This result has been proven in [74, p. 1385, Theorem 4.1] for the dipole simulation method, but the author of [74] expects that the proof can be extended to MMP [74, p. 1392, Section 6].

Moreover, one can prove that convergence results in H^1-seminorm for the Poisson's problem (1.1) solved by harmonic polynomials inside a domain $\Omega_\star \in \mathbb{R}^2$ also hold for multipoles in the complement $\Omega_\star^{\mathsf{c}}$. This is stated in the following theorem, originally reported in [28, p. 3, Proposition 1].

Proposition 2.3.1. *Let $d = 2$. If the solution $u: \Omega_\star^{\mathsf{c}} \to \mathbb{R}$ of the Poisson's problem* (1.1)

- *is harmonic [36, p. 20] in the complement $\Omega_\star^{\mathsf{c}}$ of a 2D bounded uniformly star-shaped [66, p. 56, Assumption 3.1.1] (with respect to the origin) domain $\Omega_\star$,*

- *satisfies the decay condition (1.1b) at infinity,*

- *and possesses a harmonic extension into parts of the domain $\Omega_\star$,*

then its best approximation by multipoles (2.2a) located in the origin converges exponentially with respect to the order of the multipole expansion in the H^1-seminorm.

2 Trefftz Methods

Proof. The proof is based on the *Kelvin transform* [64, p. 259, Equation 8.30]

$$u \to u^* : \quad u^*(\mathbf{x}) \coloneqq u(\mathbf{x}^*), \quad \mathbf{x}^* \coloneqq \frac{\mathbf{x}}{\|\mathbf{x}\|^2}, \quad \mathbf{x} \in \mathbb{R}^2 \setminus \{0\}. \tag{2.8}$$

For the H^1-seminorm we can show that

$$|u|_{H^1(\Omega)} = |u^*|_{H^1(\Omega^*)} \quad \forall u \colon \Omega \to \mathbb{R}, \tag{2.9}$$

where Ω is any domain in $\mathbb{R}^2$, given that the Kelvin transform preserves harmonicity. Indeed, when the Kelvin transform is applied to harmonic polynomials $p(r,\theta) = r^\ell \operatorname{cs}(\ell\theta)$, with r, θ polar coordinates in $\mathbb{R}^2$ ($r \in [0,\infty)$, $\theta \in [0, 2\pi)$), $\ell \in \mathbb{Z}^*$, $\operatorname{cs} \in \{\cos, \sin\}$, we obtain multipoles (2.2a) for the Laplace's equation in $\mathbb{R}^2$:

$$p^*(r,\theta) = r^{-\ell} \operatorname{cs}(\ell\theta). \tag{2.10}$$

Let us now consider u, solution of the Poisson's problem (1.1) respecting the conditions stated above, and the domain $\Omega_{\mathrm{m}} \coloneqq \Omega_\star^\complement$ where we want to estimate the MMP approximation. We first define $\tilde{u} \coloneqq u - c \log r$, $c \in \mathbb{R}$, whose decay satisfies $\tilde{u}(\mathbf{x}) = \mathcal{O}(\|\mathbf{x}\|^{-1})$ for $\|\mathbf{x}\| \to \infty$ uniformly. Under the Kelvin transform, $\tilde{u}^* = \mathcal{O}(\|\mathbf{x}\|)$ for $\|\mathbf{x}\| \to 0$.

Without loss of generality, we assume that Ω_{m}^*, Kelvin-transformed Ω_{m}, contains the unit disk and that $\tilde{u}^*$ is harmonic in Ω_{m}^*, which implies that $\tilde{u}^*$ possesses a harmonic extension beyond Ω_{m}^*. Thus, we can conclude exponential convergence in H^1-seminorm for the approximation by harmonic polynomials of $\tilde{u}^*$ in Ω_{m}^* [66, p. 61, Remark 3.2.6]:

$$\forall N \in \mathbb{Z}^*, \quad \exists \alpha_\ell^{(N)}, \beta_\ell^{(N)} \in \mathbb{R}, \ \ell = 1, \dots, N :$$
$$\left| \tilde{u}^* - \sum_{\ell=1}^N \alpha_\ell^{(N)} r^\ell \cos(\ell\theta) + \beta_\ell^{(N)} r^\ell \sin(\ell\theta) \right|_{H^1(\Omega_{\mathrm{m}}^*)} \leq C \, q^N \tag{2.11a}$$
for some $0 \leq q \leq 1$, $\quad C \in \mathbb{R}^+$ independent of N.

By applying (2.9) and (2.10) to (2.11a), we get that

$$\forall N \in \mathbb{Z}^*, \quad \exists \alpha_\ell^{(N)}, \beta_\ell^{(N)} \in \mathbb{R}, \ \ell = 1, \dots, N :$$
$$\left| \tilde{u} - \sum_{\ell=1}^N \alpha_\ell^{(N)} r^{-\ell} \cos(\ell\theta) + \beta_\ell^{(N)} r^{-\ell} \sin(\ell\theta) \right|_{H^1(\Omega_{\mathrm{m}})} \leq C \, q^N \tag{2.11b}$$

for some $0 \leq q \leq 1$, $\quad C \in \mathbb{R}^+$ independent of N.

Finally, we can restore the proper decay condition of u, $u(\mathbf{x}) = c \log r + \mathcal{O}(\|\mathbf{x}\|^{-1})$ for $\|\mathbf{x}\| \to \infty$, where $c \in \mathbb{R}$ is given by the coefficient $\alpha_0^{(N)}$ of the zeroth-order multipole $\log r$ (see (2.2a)). This concludes the proof. $\qquad\square$

2.3.1 Numerical Results for the Poisson's Equation

By means of a simple numerical experiment we illustrate the convergence results of Proposition 2.3.1 in $\mathbb{R}^2$. Ω_{m} is the complement of the unit square $[0,1]^2$. We test the following solution which enjoys a $\mathcal{O}(\|\mathbf{x}\|^{-1})$-decay for $\|\mathbf{x}\| \to \infty$:

$$u(\mathbf{x}) = r_{xc}^{-2} \sin(2\theta_{xc}), \tag{2.12}$$

where $r_{xc} \in [0, \infty)$ and $\theta_{xc} \in [0, 2\pi)$ are polar coordinates of vector $\mathbf{x} - \mathbf{c}$. We consider two positions of $\mathbf{c}$: $(0.4, 0.4)^\top$ and $(0.2, 0.2)^\top$. (2.12) represents a harmonic function in $H^1(\mathbb{R}^2 \setminus [0,1]^2)$ that uniformly decays for $\|\mathbf{x}\| \to \infty$ with a singularity in $\mathbf{c}$.

Multipoles are chosen from (2.2a). We consider two configurations:

1. Multipole expansions up to a fixed order 1 uniformly located on a circle at the center of the unit square $[0,1]^2$ with radius 0.25. During the convergence test we increase the number of expansions.
   Note that, given this choice of multipoles, the singularity of the solution with $\mathbf{c} = (0.4, 0.4)^\top$ lies inside the circle of multipoles, i.e. the solution has an analytic extension between Γ and the circle of multipoles Σ. On the other hand, the solution with $\mathbf{c} = (0.2, 0.2)^\top$ has the singularity outside Σ and does not have an analytic extension.

2. One multipole expansion of a given order placed in the center of the unit square $[0,1]^2$. During the test we increase this order.

We compute the best approximation of the solutions in spaces spanned by multipoles by means of the collocation method on uniformly spaced points on the edges of the unit square (corners are avoided). The number of points is chosen to make the overdetermined system almost square. The system is then solved by *QR decomposition* [47, p. 25, Section 3.3].
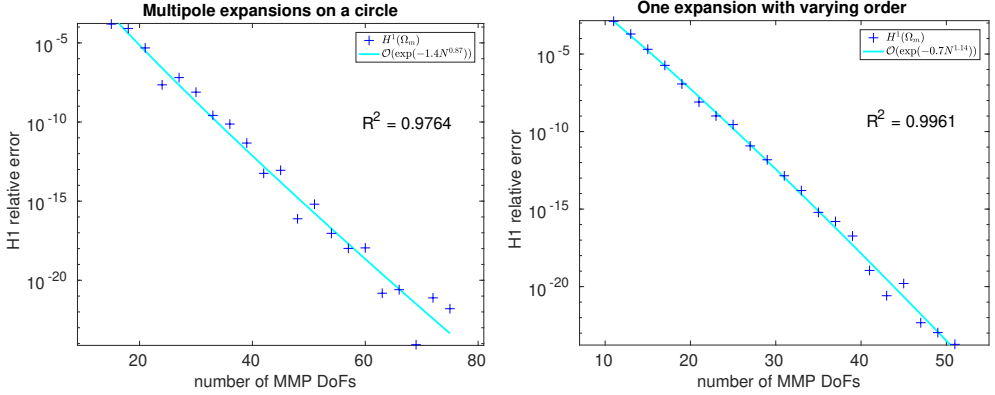
Figure 2.3: p-refinement semi-log error plots for 2D Poisson's equation without singularities solved by MMP: exponential convergence in $H^1(\Omega)$-seminorm. The solution is $r_{xc}^{-2}\sin(2\theta_{xc})$ with $\mathbf{c} = (0.4, 0.4)^\top$.

The (relative) approximation error in H^1-seminorm on the unbounded domain Ω_{m} is computed using

$$\int_{\Omega_{\mathrm{m}}} \|\nabla\,(u - u_{\mathrm{m}})\|_{\ell^2}^2 \,\mathrm{d}\mathbf{x} = \int_\Gamma \gamma_{\mathrm{N}}(u - u_{\mathrm{m}})\,(u - u_{\mathrm{m}})\,\mathrm{d}S, \qquad (2.13)$$

given the definition of multipoles (2.2a), with γ_{N} defined in Section 1.1.1. (2.13) is approximated by a Gaussian quadrature rule that is exact for polynomials of degree 2 (order 3).

For the solution with an analytic extension $(\mathbf{c} = (0.4, 0.4)^\top)$, we observe exponential convergence given both fixed-order multipole expansions on a circle and one variable-order expansion placed in the origin, as shown in Figure 2.3. This is in accordance with Proposition 2.3.1 and the literature.

For the solution without an analytic extension $(\mathbf{c} = (0.2, 0.2)^\top)$, we see convergence from Figure 2.4, but without the same regular pattern as Figure 2.3 (and the error is much higher).
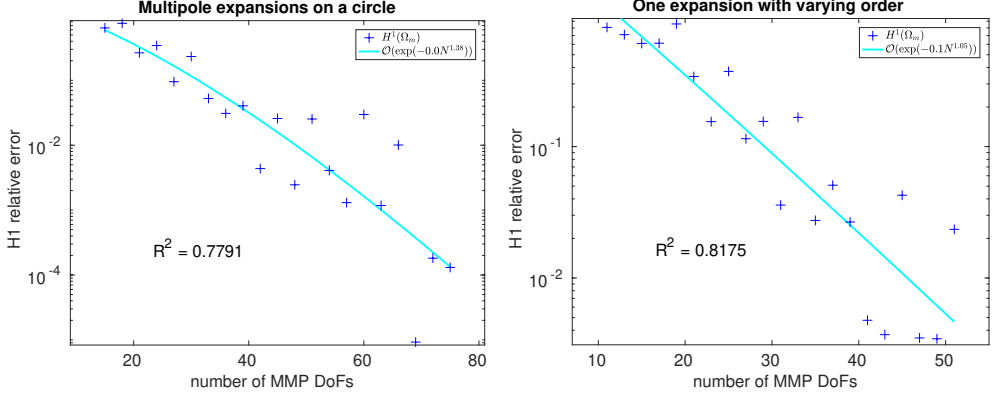
Figure 2.4: p-refinement semi-log error plots for 2D Poisson's equation with a singularity solved by MMP: convergence in $H^1(\Omega)$-seminorm. The solution is $r_{xc}^{-2}\sin(2\theta_{xc})$ with $\mathbf{c} = (0.2, 0.2)^\top$.
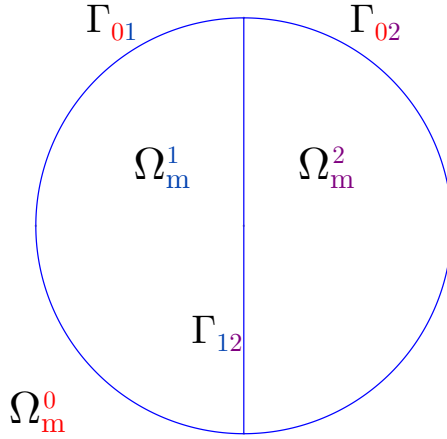
Figure 2.5: The geometry represents Ω_m^0, Ω_m^1, and Ω_m^2, the three MMP subdomains with different wavenumbers, and their shared boundaries Γ_{01}, Γ_{02}, and Γ_{12}.

2.3.2 Numerical Results for the Helmholtz Equation

We now consider the 2D Helmholtz problem (1.2) subject to the Sommerfeld radiation condition (1.2b) to show the exponential convergence implied by Proposition 2.3.1 for Helmholtz equation solved by more than one MMP discretization coupled together. The domain is $\mathbb{R}^2$ with a unit disk split into two halves: we call these subdomains Ω_m^0, Ω_m^1, and Ω_m^2 (see Figure 2.5). In each of them, the wavenumber k is referred to as k_1 in one half of the disk (Ω_m^1), k_2 in the other half (Ω_m^2), and k_0 in the complement (Ω_m^0). In Ω_m^0 we also assume that the solution u is decomposable as $u_\mathrm{inc} + u_\mathrm{ref}$, with $u_\mathrm{inc} := \exp(\imath k_0 x)$ (with x first Cartesian coordinate) a known plane wave that gives rise to the right-hand side of the problem and u_ref to be determined.

At the endpoints of the segment splitting the disk in two the solution has triple-point singularities if k_0, k_1, k_2 are all different. Hence, assuming piecewise-constant k, we need to use different Trefftz spaces for each subdomain. Multipoles are then chosen according to (2.3): Hankel functions are used on the unbounded domain Ω_m^0, Bessel functions on the bounded domains $\Omega_\mathrm{m}^1, \Omega_\mathrm{m}^2$.

We consider two configurations of multipoles:

1. Multipole expansions up to a fixed order 1 uniformly located on a circle at the center of each subdomain: $(-0.5, 0)$ for Ω_m^1, $(0.5, 0)$ for Ω_m^2, and the origin for Ω_m^0. Radii are 1.5, 1.5, and 0.5 for Ω_m^1, Ω_m^2, and Ω_m^0, respectively. During the convergence test we increase the number of expansions.

2. For each subdomain, one multipole expansion of a given order placed in the origin. During the test we increase this order.

We solve this problem by collocation, imposing interface conditions (1.11) between u_m^i, $i = 0, 1, 2$, denoting the MMP solution in Ω_m^i; in Ω_m^0, u_m^0 is shifted by the plane wave $\exp(\imath k_0 x)$. From now on, Γ_{ij}, $i < j$, $j = 0, 1, 2$, refers to the boundary $\Omega_\mathrm{m}^i \cap \Omega_\mathrm{m}^j$ (Figure 2.5).

Matching points for collocation on Γ_{ij} are found through the intersections of conforming meshes on the disk $\Omega_\mathrm{m}^1 \cup \Omega_\mathrm{m}^2$: these meshes are more refined depending on the number of degrees of freedom of $\mathcal{T}^n(\Omega_\mathrm{m}^i)$, $i = 0, 1, 2$, such that the number of matching points is always larger than the sum of the dimensions of the discrete Trefftz spaces (leading to overdetermined systems

Figure 2.6: p-refinement semi-log error plots for 2D Helmholtz equation without TPS solved with three MMP domains: exponential convergence in $H^1(\Omega_i)$-seminorm, $i = 1, 2$. Parameters are $k_1 = k_2 = 1.59\,k_0$ and $k_0 = 7.86\,\mathrm{rad\,m}^{-1}$.

solved in a least-squares sense by QR decomposition). We use volume meshes to identify matching points on boundaries Γ_{ij} because we also want to track a volume error; specifically, the (relative) approximation error in $H^1(\Omega_\mathrm{m}^i)$-seminorm

$$\int_{\Omega_\mathrm{m}^i} \left\| \nabla \left(u - u_\mathrm{m}^i \right) \right\|_{\ell^2}^2 \, \mathrm{d}\mathbf{x} \tag{2.14}$$

on bounded domains $\Omega_\mathrm{m}^1, \Omega_\mathrm{m}^2$. (2.14) is approximated by a Gaussian quadrature rule that is exact for polynomials of degree 2 (order 3). As benchmark u we rely on the numerical solution that MMP provides with a number of degrees of freedom substantially higher than the highest number used in the convergence study.

Firstly, we consider the case $k_1 = k_2 = 1.59\,k_0$ and $k_0 = 7.86\,\mathrm{rad\,m}^{-1}$, i.e. without TPS. Figure 2.6 shows the corresponding relative H^1-errors: the measured errors provide some evidence of exponential convergence, as in this example the solution possesses analytic extensions beyond the interface.

Conversely, Figure 2.7 shows these errors for $k_1 = 4\,k_0$, $k_2 = 2\,k_0$, and $k_0 = 7.86\,\mathrm{rad\,m}^{-1}$: here we may conjecture only algebraic convergence. Indeed, exponential convergence is not preserved because the solution has TPS (no
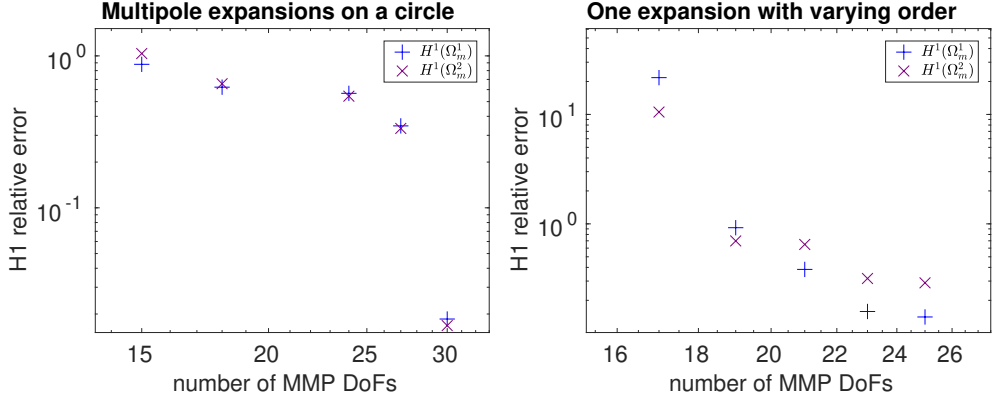
Figure 2.7: *p*-refinement log-log error plots for 2D Helmholtz equation with TPS solved with three MMP domains: convergence in $H^1(\Omega_i)$-seminorm, $i = 1, 2$. Parameters are $k_1 = 4\,k_0$, $k_2 = 2\,k_0$, and $k_0 = 7.86\,\mathrm{rad\,m^{-1}}$.
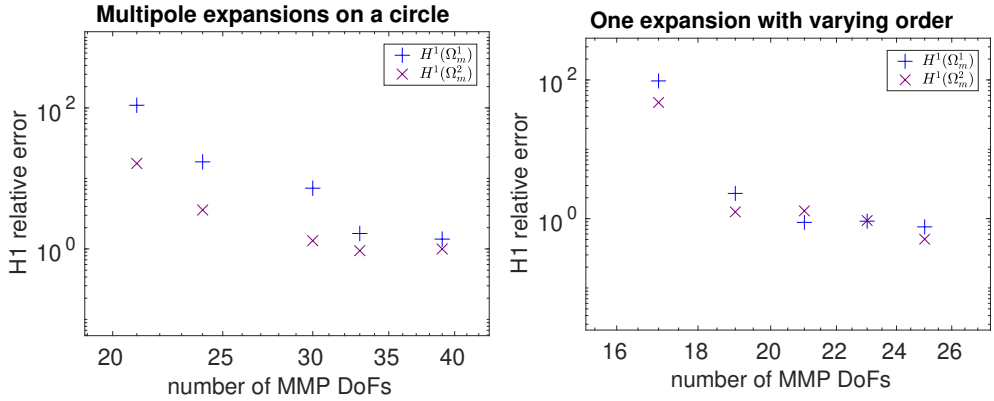
Figure 2.8: *p*-refinement log-log error plots for 2D Helmholtz equation with TPS solved with three MMP domains: convergence in $H^1(\Omega_i)$-seminorm, $i = 1, 2$. Parameters are $k_1 = 100\,k_0$, $k_2 = 10\,k_0$, and $k_0 = 7.86\,\mathrm{rad\,m^{-1}}$.

harmonic extension for Proposition 2.3.1), and therefore convergence becomes much slower. Figure 2.8 presents more pronounced TPS with $k_1 = 100\,k_0$, $k_2 = 10\,k_0$, and $k_0 = 7.86\,\mathrm{rad\,m^{-1}}$: even algebraic convergence becomes difficult to recognize.

2.4 Trefftz Approximation Error for Maxwell's Equations

A corresponding result to Proposition 2.3.1 for $d = 3$ remains elusive. However, here we present a numerical experiment showing that exponential convergence also holds for Maxwell's problem (1.3).

We consider the equations $\nabla \times (\nabla \times \mathbf{u}) - k^2\,\mathbf{u} = \mathbf{0}$, $\nabla \cdot \mathbf{u} = 0$ subject to the Silver-Müller radiation condition (1.3b). The domain is $\mathbb{R}^3$ with a unit ball: we call this subdomain Ω_{m}^1 and the complement Ω_{m}^0 (see Section 1.2). In each of them, the wavenumber k is referred to as k_1 and k_0. In Ω_{m}^0 we also assume that the solution $\mathbf{u}$ is decomposable as $\mathbf{u}_{\mathrm{inc}} + \mathbf{u}_{\mathrm{ref}}$, with $\mathbf{u}_{\mathrm{inc}} := \exp(\imath k_0 z)\,(0, 1, 0)^\top$ (with z third Cartesian coordinate) a known plane wave that gives rise to the right-hand side of the problem and $\mathbf{u}_{\mathrm{ref}}$ to be determined.

Assuming piecewise-constant k, we need to use different Trefftz spaces for each subdomain. Multipoles are then chosen according to (2.4): Hankel functions are used on the unbounded domain Ω_{m}^0, Bessel functions on the bounded domain Ω_{m}^1.

We consider two configurations of multipoles:

1. Multipole expansions up to a fixed order 1 uniformly located on unit cubes centered in the origin. Side lengths are 2.6 and 0.8 for Ω_{m}^1 and Ω_{m}^0, respectively. During the convergence test we increase the number of expansions.

2. For each subdomain, one multipole expansion of a given order placed in the origin. During the test we increase this order.

We solve this problem by collocation, imposing interface conditions (1.12) between $\mathbf{u}_{\mathrm{m}}^i$, $i = 0, 1$, denoting the MMP solution in Ω_{m}^i; in Ω_{m}^0, u_{m}^0 is shifted by the plane wave $\exp(\imath k_0 z)\,(0, 1, 0)^\top$. From now on, Γ_{01} refers to the boundary $\Omega_{\mathrm{m}}^0 \cap \Omega_{\mathrm{m}}^1$.
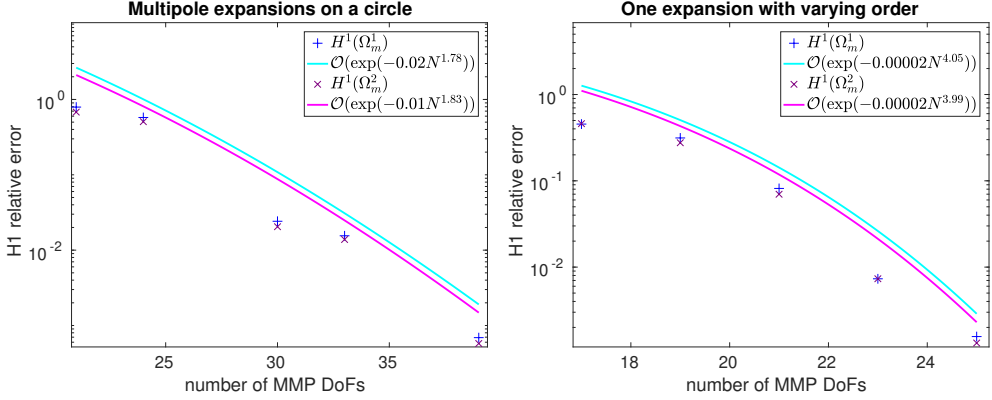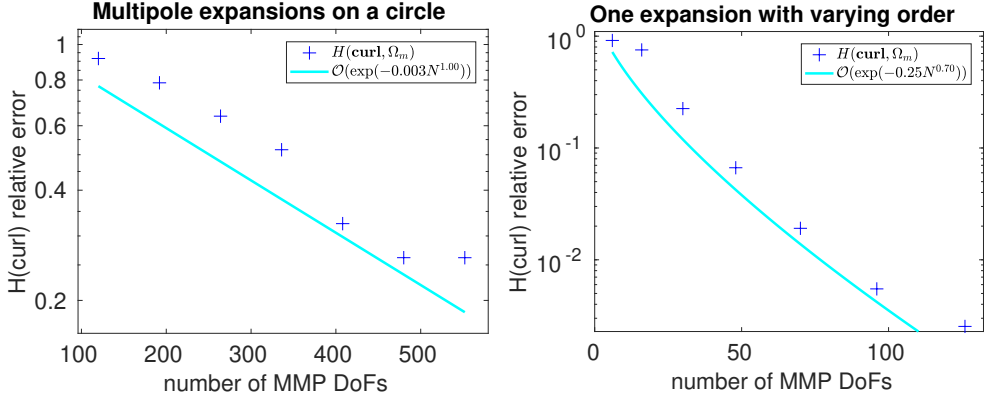
Figure 2.9: *p*-refinement semi-log error plots for Maxwell's equations without TPS solved with two MMP domains: exponential convergence in $\mathbf{H}(\mathbf{curl}, \Omega_1)$-seminorm. Parameters are $k_1 = 1.59\, k_0$ and $k_0 = 3.33\,\mathrm{rad\,m}^{-1}$.

Matching points for collocation on Γ_{01} are found through the intersections of meshes on the ball Ω_{m}^1: these meshes are more refined depending on the number of degrees of freedom of $\mathcal{T}^n(\Omega_{\mathrm{m}}^i)$, $i = 0, 1$, such that the number of matching points is always larger than the sum of the dimensions of the discrete Trefftz spaces (leading to overdetermined systems solved in a least-squares sense by QR decomposition). We use volume meshes to identify matching points on boundaries Γ_{01} because we also want to track a volume error; specifically, the relative approximation error in $\mathbf{H}(\mathbf{curl}, \Omega_{\mathrm{m}}^1)$-seminorm

$$\int_{\Omega_{\mathrm{m}}^1} \left\| \nabla \times \left(u - u_{\mathrm{m}}^1 \right) \right\|_{\ell^2}^2 \mathrm{d}\mathbf{x} \tag{2.15}$$

on the bounded domain Ω_{m}^1. (2.15) is approximated by a Gaussian quadrature rule that is exact for polynomials of degree 2 (order 3). As benchmark $\mathbf{u}$ we rely on the numerical solution that MMP provides with a number of degrees of freedom substantially higher than the highest number used in the convergence study.

We take constant parameters $k_1 = 1.59\, k_0$ and $k_0 = 3.33\,\mathrm{rad\,m}^{-1}$. Figure 2.9 shows the corresponding relative $\mathbf{H}(\mathbf{curl})$-errors: it hints at exponential convergence, as in this example the solution possesses analytic extensions beyond
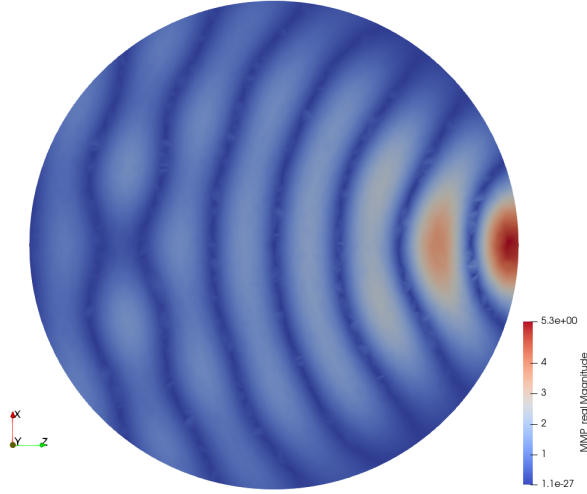
Figure 2.10: Magnitude of the real component of **u** along the XZ-plane for $k_1 = 1.59\,k_0$ and $k_0 = 7.86\,\mathrm{rad\,m^{-1}}$. The beam on the surface of the ball is the photonic nanojet.

the interface. Yet, the same error is reached by the multipoles on cubes with a much larger number of degrees of freedom than the single expansions: this is due to the higher instability of the former configuration compared to the latter (the aforementioned heuristics issue).

As a matter of fact, one could expand the incident plane wave in terms of vector spherical harmonics and obtain coefficients for the resulting fields in $\Omega_{\mathrm{m}}^0, \Omega_{\mathrm{m}}^1$ as multipole expansions centered in the origin – see Section 6.6.1. At the same time, considering a full plane wave as excitation, as we do in Figure 2.9, and choosing a slightly higher wavenumber $k_0 = 7.86\,\mathrm{rad\,m^{-1}}$ (higher frequency), one can observe a *photonic nanojet* [49, p. 1985, Fig. 4.a] in Figure 2.10, which illustrates the magnitude of the real component of **u** along the XZ-plane: given that $\exp(\imath k_0 z)\,(0,1,0)^\top$ propagates along the z-axis, we can in fact see a beam on the point where the plane wave first hits Ω_{m}^1, i.e. where Γ_{01} intersects the positive z-axis. We will again observe this phenomenon in Section 6.3.1 with the FEM–MMP coupling.

Remark 2.4.1. *MMP without modifications cannot properly handle more complicated situations than those explored in Sections 2.3.2 and 2.4, such as triple-*

point singularities, and preserve its exponential behavior. For example, this is shown in Figures 2.7 and 2.8 for 2D Helmholtz equation. There are two ways to cope with these situations:

1. *Augmenting the Trefftz spaces with basis functions that capture the singularities [11]. However, explicit knowledge of the form of such singularities is required.*

2. *Coupling MMP with a method based on volume meshes, like FEM, and applying the latter to a locally-refined mesh that encompasses both the singularities and their immediate surrounding regions. By truncating the mesh at an auxiliary boundary that does not coincide with any physical discontinuity, MMP can be applied to a region where the field is sufficiently easy to approximate that heuristics on the placement of multipoles (relevant for, e.g., the two configurations of Figure 2.9) does not impact much on the quality of the solution. This is the approach followed by this work.*

3 Coupling Strategies

From now on, we refer to the computational domain decomposition introduced in Section 1.2 (see, for example, Figure 1.1b) solved by FEM (Section 1.4) in Ω_{f} and a Trefftz method (Chapter 2) in Ω_{m}, which can be either a single domain or $:= \Omega_{\mathrm{m}}^0 \cup \Omega_{\mathrm{m}}^1$, depending on the problem of Section 1.1.

Interface conditions (1.10) on Γ (given a single Trefftz domain) and the weak form (1.13a) of (1.1a) in Ω_{f} are all the ingredients to obtain a FEM–Trefftz coupled solution of (1.1). By inserting the interface condition (1.10b) into the boundary integral of (1.13a), we obtain

Seek $u_{\mathrm{f}} \in H^1(\Omega_{\mathrm{f}})$, $u_{\mathrm{m}} \in \mathcal{T}(\Omega_{\mathrm{m}})$:

$$\int_{\Omega_{\mathrm{f}}} \left(\mathbf{M}_\mu^{-1} \nabla u_{\mathrm{f}} \right) \cdot \nabla v_{\mathrm{f}} \, \mathrm{d}\mathbf{x} - \int_{\Gamma} \gamma_{\mathrm{N}} u_{\mathrm{m}} \, v_{\mathrm{f}} \, \mathrm{d}S = \int_{\Omega_{\mathrm{f}}} j \, v_{\mathrm{f}} \, \mathrm{d}\mathbf{x} \quad \forall v_{\mathrm{f}} \in H^1(\Omega_{\mathrm{f}}). \tag{3.1a}$$

Correspondingly, we need interface conditions (1.12) on $\Gamma_{\mathrm{f0}}, \Gamma_{\mathrm{f1}}, \Gamma_{01}$ and the weak form (1.13b) of (1.3a) in Ω_{f} to develop the FEM–Trefftz coupling of (1.3). By inserting (1.12b) and (1.12c) on $\Gamma_{\mathrm{f0}}, \Gamma_{\mathrm{f1}}$ into the boundary integrals of (1.13b), we obtain

Seek $\mathbf{u}_{\mathrm{f}} \in \mathbf{H}_\Gamma(\mathbf{curl}, \Omega_{\mathrm{f}})$, $\mathbf{u}_{\mathrm{m}}^0 \in \boldsymbol{\mathcal{T}}(\Omega_{\mathrm{m}}^0)$, $\mathbf{u}_{\mathrm{m}}^1 \in \boldsymbol{\mathcal{T}}(\Omega_{\mathrm{m}}^1)$, $\phi_{\mathrm{f}} \in H_*^1(\Omega_{\mathrm{f}})$:

$$\begin{cases} \int_{\Omega_{\mathrm{f}}} \left[\left(\mathbf{M}_\mu^{-1} \nabla \times \mathbf{u}_{\mathrm{f}} \right) \cdot (\nabla \times \mathbf{v}_{\mathrm{f}}) - \omega^2 \left(\mathbf{M}_\epsilon \mathbf{u}_{\mathrm{f}} \right) \cdot \mathbf{v}_{\mathrm{f}} \right] \mathrm{d}\mathbf{x} \; + \\ \quad \sum\limits_{i=0,1} \int_{\Gamma_{\mathrm{f}i}} \boldsymbol{\gamma}_{\mathrm{m}} \mathbf{u}_{\mathrm{m}}^i \cdot \mathbf{v}_{\mathrm{f}} \, \mathrm{d}S + \int_{\Omega_{\mathrm{f}}} \nabla \phi_{\mathrm{f}} \cdot \mathbf{v}_{\mathrm{f}} \, \mathrm{d}\mathbf{x} = \int_{\Omega_{\mathrm{f}}} \mathbf{j} \cdot \mathbf{v}_{\mathrm{f}} \, \mathrm{d}\mathbf{x} \quad \forall \mathbf{v}_{\mathrm{f}} \in \mathbf{H}(\mathbf{curl}, \Omega_{\mathrm{f}}), \\ \int_{\Omega_{\mathrm{f}}} \mathbf{u}_{\mathrm{f}} \cdot \nabla \psi_{\mathrm{f}} \, \mathrm{d}\mathbf{x} - \sum\limits_{i=0,1} \int_{\Gamma_{\mathrm{f}i}} \left(\mathbf{n} \cdot \mathbf{u}_{\mathrm{m}}^i \right) \psi_{\mathrm{f}} \, \mathrm{d}S = 0 \qquad\qquad \forall \psi_{\mathrm{f}} \in H_*^1(\Omega_{\mathrm{f}}). \end{cases}$$

$$\tag{3.1b}$$

Note that, even if in (1.3a) the second equation (Coulomb gauge) is implicitly contained in the first in the case of piecewise-constant $\mu, \epsilon \in \mathbb{C}$ in Ω_{f}, the Coulomb gauge needs to be imposed nonetheless via the Lagrange multiplier

$\phi_\mathrm{f} \in H^1_*(\Omega_\mathrm{f})$ for (1.12c) to hold through the boundary integrals of the second line of (3.1b).[1] Conversely, the Coulomb gauge is already taken into account strongly for functions $\mathbf{u}^i_\mathrm{m} \in \boldsymbol{\mathcal{T}}(\Omega^i_\mathrm{m})$, $i = 0, 1$.

We end up with four different coupling approaches depending on how we impose

- the additional interface condition (1.10a) on Γ for (3.1a) and

- (1.12a) on $\Gamma_{\mathrm{f}0}, \Gamma_{\mathrm{f}1}$ and all interface conditions (1.12) on Γ_{01} for (3.1b).

These coupling approaches in the continuous and discrete cases are discussed in the following sections as stationary problems for different *Lagrangian functionals* [18, p. 129, (4.3)]. The resulting *linear variational saddle-point problems* [18, p. 129, (4.4)] are also stated.

The coupling strategies are illustrated for both the Poisson's (with one Trefftz domain) and Maxwell's cases. Furthermore, for Poisson's problem, we prove existence, uniqueness, and stability of the FEM–Trefftz coupled solutions based on abstract saddle-point theory [18, p. 129, Section 4] for both the continuous and discrete cases.[2]

3.1 PDE-constrained Least-Squares Coupling

3.1.1 Poisson's Equation

We determine a quadratic minimization problem under a linear variational constraint [50, p. 2, (1.1)] by seeking $u_\mathrm{f} \in H^1(\Omega_\mathrm{f})$ and $u_\mathrm{m} \in \mathcal{T}(\Omega_\mathrm{m})$ that

1. minimize the mismatch in the interface condition

$$\mathrm{J}_\Gamma(u_\mathrm{f}, u_\mathrm{m}) \coloneqq \|u_\mathrm{f} - u_\mathrm{m}\|^2_{H^{\frac{1}{2}}(\Gamma)} \tag{3.2}$$

2. and satisfy the constraint (3.1a).

---

[1] This is also why we choose $\phi_\mathrm{f} \in H^1_*(\Omega_\mathrm{f})$ instead of $H^1_0(\Omega_\mathrm{f})$ [67, p. 38, (3.5)]: otherwise, the boundary integrals to impose (1.12c) would disappear from the second line of (3.1b).

[2] Except for the DG-based coupling (Section 3.2), which only works in the discrete sense.

Note that here the constraint is given by the variational form of the system of PDEs (1.1a) in Ω_f, while the functional J_Γ to be minimized is based on the interface condition not imposed by the variational form (3.1a).

This problem can be rephrased as seeking a saddle point of the following Lagrangian:

$$
\mathrm{L}(u_f, u_m, p_f) := \frac{1}{2} \left\| u_f - u_m \right\|_{L^2(\Gamma)}^2 +
$$
$$
\int_{\Omega_f} \left(\mathbf{M}_\mu^{-1} \nabla u_f \right) \cdot \nabla p_f \, \mathrm{d}\mathbf{x} + \int_\Gamma \gamma_N u_m \, p_f \, \mathrm{d}S - \int_{\Omega_f} j \, p_f,
\tag{3.3}
$$

where $p_f \in H^1(\Omega_f)$ is the Lagrange multiplier imposing (3.1a).

Saddle-Point Problem

The trace norm $\left\| \cdot \right\|_{H^{\frac{1}{2}}(\Gamma)}$ is nonlocal. Thus, for practicality we replace it with the $L^2(\Gamma)$-norm in (3.2) and seek $u_f \in H_\Gamma^1(\Omega_f) := \left\{ v \in H^1(\Omega_f) \colon\ v|_\Gamma \in L_t^2(\Gamma) \right\}$. Given this substitution, the necessary and sufficient optimality conditions of (3.3) give rise to the saddle-point problem

$$
\text{Seek } u_f \in H_\Gamma^1(\Omega_f),\ u_m \in \mathcal{T}(\Omega_m),\ p_f \in H^1(\Omega_f)\colon
$$
$$
\begin{cases}
\mathrm{a}_{\mathrm{LS}}[(u_f, u_m),(v_f, v_m)] + \mathrm{b}_{\mathrm{LS}}[(v_f, v_m), p_f] = 0 \\
\mathrm{b}_{\mathrm{LS}}[(u_f, u_m), q_f] \qquad\qquad\qquad\quad = \int_{\Omega_f} j\, q_f \, \mathrm{d}\mathbf{x}
\end{cases}
\tag{3.4}
$$
$$
\forall v_f \in H_\Gamma^1(\Omega_f),\ \forall v_m \in \mathcal{T}(\Omega_m),\ \forall q_f \in H^1(\Omega_f),
$$

where

$$
\mathrm{a}_{\mathrm{LS}}[(u_f, u_m),(v_f, v_m)] := \int_\Gamma (u_f - u_m)\,(v_f - v_m) \, \mathrm{d}S,
\tag{3.5a}
$$

$$
\mathrm{b}_{\mathrm{LS}}[(u_f, u_m), q_f] := \int_{\Omega_f} \left(\mathbf{M}_\mu^{-1} \nabla u_f \right) \cdot \nabla q_f \, \mathrm{d}\mathbf{x} - \int_\Gamma \gamma_N u_m \, q_f \, \mathrm{d}S.
\tag{3.5b}
$$

We propose the following discretization for (3.4):

- $u_f, v_f, p_f, q_f \in V^n(\mathcal{M}_f)$, see (1.14a), and
- $u_m, v_m \in \mathcal{T}^n(\Omega_m)$.

Existence, Uniqueness, and Stability

The constraint implied by the second line of (3.4) uniquely defines a function $u_f = u_f(u_m)$ that satisfies $\gamma_N u_f = \gamma_N u_m$ from (1.10b). Thus, the existence and uniqueness of a solution to (3.4) follows from those for (1.1). However, stability in energy norms cannot be proven as a_{LS} fails to be coercive on the kernel of b_{LS}.

Remark 3.1.1. *If we relied on the $H^{\frac{1}{2}}(\Gamma)$-inner product $\langle \cdot, \cdot \rangle_{H^{\frac{1}{2}}(\Gamma)}$ and defined*

$$a_{LS}[(u_f, u_m), (v_f, v_m)] := \langle u_f - u_m, v_f - v_m \rangle_{H^{\frac{1}{2}}(\Gamma)}, \qquad (3.6)$$

then the ellipticity on the kernel *condition [18, p. 132, Theorem 4.3, (i)] of abstract saddle-point theory would be satisfied for* (3.4)*. To see it note that, if $(u_f, u_m) \in H^1(\Omega_f) \times \mathcal{T}(\Omega_m)$ satisfy $b_{LS}[(u_f, u_m), q_f] = 0$ for all $q_f \in H^1(\Omega_f)$, then integration by parts in Ω_m shows that*

$$|u_f|^2_{H^1(\Omega_f)} + |u_m|^2_{H^1(\Omega_m)} \leq C \left\{ \|u_f - u_m\|^2_{H^{\frac{1}{2}}(\Gamma)} + \|\gamma_N u_f - \gamma_N u_m\|^2_{H^{-\frac{1}{2}}(\Gamma)} \right\} \quad (3.7)$$

for some $C \in \mathbb{R}^+$. The second term on the right-hand side vanishes. Yet, the $H^{\frac{1}{2}}(\Gamma)$-inner product is nonlocal and, consequently, not suitable for numerical purposes.

The Galerkin discretization of (3.4) is straightforward:

- We replace $H^1(\Omega_f)$ with a Lagrangian finite element space $V^n(\mathcal{M}_f)$ built on a mesh $\mathcal{M}_f$ of Ω_f, as in (1.14a).

- We approximate u_m and v_m in a finite-dimensional Trefftz space $\mathcal{T}^n(\Omega_m) \subset \mathcal{T}(\Omega_m)$.

We appeal to variational saddle-point theory and note that a uniform discrete *inf-sup condition* [18, p. 130] of abstract saddle-point theory for b_{LS} is immediate.

Yet, ellipticity on the discrete kernel,

$$\ker^n b_{LS} := \{(v_f^n, v_m^n) \in V^n \times \mathcal{T}^n : b_{LS}[(v_f, v_m), q_f] = 0 \ \forall q_f \in V^n\}, \quad (3.8a)$$

hinges on an inverse inequality. Define

$$K^n := \sup \left\{ \|\gamma_{\mathrm{N}} u_{\mathrm{m}}^n\|_{L^2(\Gamma)} \colon \ u_{\mathrm{m}}^n \in \mathcal{T}^n, \ \|\gamma_{\mathrm{N}} u_{\mathrm{m}}^n\|_{H^{-\frac{1}{2}}(\Gamma)} = 1 \right\}. \tag{3.8b}$$

By the equivalence of all norms on finite-dimensional spaces, a finite $K^n \in \mathbb{R}^+$ will exist. Let $(u_{\mathrm{f}}^n, u_{\mathrm{m}}^n) \in \ker^n b_{\mathrm{LS}}$. This means that $\int_\Gamma \gamma_{\mathrm{N}} u_{\mathrm{m}}^n \, \mathrm{d}S = 0$, which implies $\nabla u_{\mathrm{m}}^n(\mathbf{x}) = \mathcal{O}(\|\mathbf{x}\|^{-2})$. As a consequence, $\nabla u_{\mathrm{m}}^n \in L^2(\Omega_{\mathrm{m}})$ also for $d = 2$. Thus, we get

$$\int_{\Omega_{\mathrm{f}}} \left(\mathbf{M}_\mu^{-1} \nabla u_{\mathrm{f}}^n \right) \cdot \nabla u_{\mathrm{f}}^n \, \mathrm{d}\mathbf{x} + \int_{\Omega_{\mathrm{m}}} \|\nabla u_{\mathrm{m}}^n\|_{\ell^2}^2 \, \mathrm{d}\mathbf{x} = \int_\Gamma (u_{\mathrm{f}}^n - u_{\mathrm{m}}^n) \, \gamma_{\mathrm{N}} u_{\mathrm{m}}^n \, \mathrm{d}S. \tag{3.9}$$

We conclude that, with $C \in \mathbb{R}^+$ independent of the choice of both $V^n(\mathcal{M}_{\mathrm{f}})$ and $\mathcal{T}^n(\Omega_{\mathrm{m}})$,

$$\|\nabla u_{\mathrm{f}}^n\|_{L^2(\Omega_{\mathrm{f}})}^2 + \|\nabla u_{\mathrm{m}}^n\|_{L^2(\Omega_{\mathrm{m}})}^2 \leq C \, \|u_{\mathrm{f}}^n - u_{\mathrm{m}}^n\|_{L^2(\Gamma)} \cdot \|\gamma_{\mathrm{N}} u_{\mathrm{m}}^n\|_{L^2(\Gamma)}. \tag{3.10a}$$

Next, we use the inverse inequality implicit in (3.8b), together with the estimate $\|\gamma_{\mathrm{N}} u_{\mathrm{m}}\|_{H^{-\frac{1}{2}}(\Gamma)} \leq C \, \|\nabla u_{\mathrm{m}}\|_{L^2(\Omega_{\mathrm{m}})} \ \forall u_{\mathrm{m}} \in \mathcal{T}(\Omega_{\mathrm{m}}), \, C \in \mathbb{R}^+$, and obtain

$$\|\nabla u_{\mathrm{f}}^n\|_{L^2(\Omega_{\mathrm{f}})} + \|\nabla u_{\mathrm{m}}^n\|_{L^2(\Omega_{\mathrm{m}})} \leq C \, K^n \, \|u_{\mathrm{f}}^n - u_{\mathrm{m}}^n\|_{L^2(\Gamma)}, \tag{3.10b}$$

which proves the ellipticity of a_{LS} on $\ker^n b_{\mathrm{LS}}$, albeit with a constant K^n tending to zero as the Trefftz space $\mathcal{T}^n(\Omega_{\mathrm{m}})$ is refined. Hence, the discrete variational problem is stable, but convergence is guaranteed only if, asymptotically, the approximation errors decay faster than K^n increases.

3.1.2 Maxwell's Equations

We determine a quadratic minimization problem under a linear variational constraint [50, p. 2, (1.1)] by seeking $\mathbf{u}_{\mathrm{f}} \in \mathbf{H}(\mathbf{curl}, \Omega_{\mathrm{f}})$, $\mathbf{u}_{\mathrm{m}}^0 \in \boldsymbol{\mathcal{T}}(\Omega_{\mathrm{m}}^0)$, and $\mathbf{u}_{\mathrm{m}}^1 \in \boldsymbol{\mathcal{T}}(\Omega_{\mathrm{m}}^1)$ that

1. minimize the mismatch in the interface conditions

$$\mathrm{J}_\Gamma(\mathbf{u}_{\mathrm{f}}, \mathbf{u}_{\mathrm{m}}^0, \mathbf{u}_{\mathrm{m}}^1) := \left\| \mathbf{n} \times \left(\mathbf{u}_{\mathrm{f}} - \mathbf{u}_{\mathrm{m}}^0 \right) \right\|_{\mathbf{H}^{-\frac{1}{2}}(\mathrm{div}_{\Gamma_{\mathrm{f}0}}, \Gamma_{\mathrm{f}0})}^2 +$$

$$\left\| \mathbf{n} \times \left(\mathbf{u}_{\mathrm{f}} - \mathbf{u}_{\mathrm{m}}^1 \right) \right\|_{\mathbf{H}^{-\frac{1}{2}}(\mathrm{div}_{\Gamma_{\mathrm{f}1}}, \Gamma_{\mathrm{f}1})}^2 + \left\| \mathbf{n} \times \left(\mathbf{u}_{\mathrm{m}}^0 - \mathbf{u}_{\mathrm{m}}^1 \right) \right\|_{\mathbf{H}^{-\frac{1}{2}}(\mathrm{div}_{\Gamma_{01}}, \Gamma_{01})}^2 +$$

$$\left\| \gamma_{\mathrm{m}} \left(\mathbf{u}_{\mathrm{m}}^0 - \mathbf{u}_{\mathrm{m}}^1 \right) \right\|_{\mathbf{H}^{-\frac{1}{2}}(\mathrm{div}_{\Gamma_{01}}, \Gamma_{01})}^2 + \left\| \mathbf{n} \cdot \left(\mathbf{u}_{\mathrm{m}}^0 - \mathbf{u}_{\mathrm{m}}^1 \right) \right\|_{H^{-\frac{1}{2}}(\Gamma_{01})}^2$$

$$\tag{3.11}$$

2. and satisfy the PDE-constraint (3.1b).

Note that here the constraint is given by the variational form of the system of PDEs (1.3a) in Ω_{f}, while the functional J_Γ to be minimized is based on the interface conditions not imposed by the variational form (3.1b).

This problem can be rephrased as seeking a saddle point of the following Lagrangian:

$$
\mathrm{L}(\mathbf{u}_{\mathrm{f}}, \mathbf{u}_{\mathrm{m}}^0, \mathbf{u}_{\mathrm{m}}^1, \phi_{\mathrm{f}}, \mathbf{p}_{\mathrm{f}}, \xi_{\mathrm{f}}) := \frac{1}{2}\ \mathrm{J}_\Gamma(\mathbf{u}_{\mathrm{f}}, \mathbf{u}_{\mathrm{m}}^0, \mathbf{u}_{\mathrm{m}}^1) +
$$

$$
\int_{\Omega_{\mathrm{f}}} \left[\left(\mathbf{M}_\mu^{-1} \nabla \times \mathbf{u}_{\mathrm{f}}\right) \cdot (\nabla \times \mathbf{p}_{\mathrm{f}}) - \omega^2 \left(\mathbf{M}_\epsilon \mathbf{u}_{\mathrm{f}}\right) \cdot \mathbf{p}_{\mathrm{f}} \right] \mathrm{d}\mathbf{x} + \sum_{i=0,1} \int_{\Gamma_{\mathrm{f}i}} \boldsymbol{\gamma}_{\mathrm{m}} \mathbf{u}_{\mathrm{m}}^i \cdot \mathbf{p}_{\mathrm{f}}\ \mathrm{d}S +
$$

$$
\int_{\Omega_{\mathrm{f}}} \nabla \phi_{\mathrm{f}} \cdot \mathbf{p}_{\mathrm{f}}\ \mathrm{d}\mathbf{x} - \int_{\Omega_{\mathrm{f}}} \mathbf{j} \cdot \mathbf{p}_{\mathrm{f}} + \int_{\Omega_{\mathrm{f}}} \mathbf{u}_{\mathrm{f}} \cdot \nabla \xi_{\mathrm{f}}\ \mathrm{d}\mathbf{x} - \sum_{i=0,1} \int_{\Gamma_{\mathrm{f}i}} \left(\mathbf{n} \cdot \mathbf{u}_{\mathrm{m}}^i\right) \xi_{\mathrm{f}}\ \mathrm{d}S.
$$

$$(3.12)$$

- $\phi_{\mathrm{f}} \in H_*^1(\Omega_{\mathrm{f}})$, as discussed in Section 1.3.

- $\mathbf{p}_{\mathrm{f}} \in \mathbf{H}(\mathbf{curl}, \Omega_{\mathrm{f}})$ is the Lagrange multiplier imposing the first line of (3.1b).

- $\xi_{\mathrm{f}} \in H_*^1(\Omega_{\mathrm{f}})$ is the Lagrange multiplier imposing the second line of (3.1b).

Saddle-Point Problem

The trace norms $\|\cdot\|_{\mathbf{H}^{-\frac{1}{2}}(\mathrm{div}_{\Gamma_\square}, \Gamma_\square)}, \|\cdot\|_{H^{-\frac{1}{2}}(\Gamma_\square)}$ are nonlocal. Thus, for practicality we replace them with the $\mathbf{L}^2(\Gamma_\square)$ and $L^2(\Gamma_\square)$-norms in (3.11), respectively, and seek $\mathbf{u}_{\mathrm{f}} \in \mathbf{H}_{\partial\Omega_{\mathrm{f}}}(\mathbf{curl}, \Omega_{\mathrm{f}}) := \left\{ \mathbf{v} \in \mathbf{H}(\mathbf{curl}, \Omega_{\mathrm{f}}): \ \mathbf{n} \times \mathbf{v}|_{\partial\Omega_{\mathrm{f}}} \in \mathbf{L}_t^2(\partial\Omega_{\mathrm{f}}) \right\}$. Given this substitution, the necessary and sufficient optimality conditions of

(3.12) give rise to the saddle-point problem

Seek $\mathbf{u}_{\mathrm{f}} \in \mathbf{H}_{\partial \Omega_{\mathrm{f}}}(\mathbf{curl}, \Omega_{\mathrm{f}})$, $\mathbf{u}_{\mathrm{m}}^0 \in \boldsymbol{\mathcal{T}}(\Omega_{\mathrm{m}}^0)$, $\mathbf{u}_{\mathrm{m}}^1 \in \boldsymbol{\mathcal{T}}(\Omega_{\mathrm{m}}^1)$,
$\phi_{\mathrm{f}} \in H_*^1(\Omega_{\mathrm{f}})$, $\mathbf{p}_{\mathrm{f}} \in \mathbf{H}(\mathbf{curl}, \Omega_{\mathrm{f}})$, $\xi_{\mathrm{f}} \in H_*^1(\Omega_{\mathrm{f}})$:

$$
\begin{cases}
\mathrm{a}_{\mathrm{LS}}[\left(\mathbf{u}_{\mathrm{f}}, \mathbf{u}_{\mathrm{m}}^0, \mathbf{u}_{\mathrm{m}}^1\right), \left(\mathbf{v}_{\mathrm{f}}, \mathbf{v}_{\mathrm{m}}^0, \mathbf{v}_{\mathrm{m}}^1\right)] + \mathrm{b}_{\mathrm{LS}}[\left(\mathbf{v}_{\mathrm{f}}, \mathbf{v}_{\mathrm{m}}^0, \mathbf{v}_{\mathrm{m}}^1, \psi_{\mathrm{f}}\right), (\mathbf{p}_{\mathrm{f}}, \xi_{\mathrm{f}})] = 0 \\
\mathrm{b}_{\mathrm{LS}}[\left(\mathbf{u}_{\mathrm{f}}, \mathbf{u}_{\mathrm{m}}^0, \mathbf{u}_{\mathrm{m}}^1, \phi_{\mathrm{f}}\right), (\mathbf{q}_{\mathrm{f}}, \zeta_{\mathrm{f}})] \qquad\qquad\qquad = \int_{\Omega_{\mathrm{f}}} \mathbf{j} \cdot \mathbf{q}_{\mathrm{f}} \, \mathrm{d}\mathbf{x}
\end{cases}
$$

$\forall \mathbf{v}_{\mathrm{f}} \in \mathbf{H}_{\partial \Omega_{\mathrm{f}}}(\mathbf{curl}, \Omega_{\mathrm{f}})$, $\forall \mathbf{v}_{\mathrm{m}}^0 \in \boldsymbol{\mathcal{T}}(\Omega_{\mathrm{m}}^0)$, $\forall \mathbf{v}_{\mathrm{m}}^1 \in \boldsymbol{\mathcal{T}}(\Omega_{\mathrm{m}}^1)$,
$\forall \psi_{\mathrm{f}} \in H_*^1(\Omega_{\mathrm{f}})$, $\forall \mathbf{q}_{\mathrm{f}} \in \mathbf{H}(\mathbf{curl}, \Omega_{\mathrm{f}})$, $\forall \zeta_{\mathrm{f}} \in H_*^1(\Omega_{\mathrm{f}})$,

$$\tag{3.13}$$

where

$$
\mathrm{a}_{\mathrm{LS}}\left[\left(\mathbf{u}_{\mathrm{f}}, \mathbf{u}_{\mathrm{m}}^0, \mathbf{u}_{\mathrm{m}}^1\right), \left(\mathbf{v}_{\mathrm{f}}, \mathbf{v}_{\mathrm{m}}^0, \mathbf{v}_{\mathrm{m}}^1\right)\right] :=
$$

$$
\int_{\Gamma_{\mathrm{f0}}} \left[\mathbf{n} \times \left(\mathbf{u}_{\mathrm{f}} - \mathbf{u}_{\mathrm{m}}^0\right)\right] \cdot \left[\mathbf{n} \times \left(\mathbf{v}_{\mathrm{f}} - \mathbf{v}_{\mathrm{m}}^0\right)\right] \mathrm{d}S +
$$

$$
\int_{\Gamma_{\mathrm{f1}}} \left[\mathbf{n} \times \left(\mathbf{u}_{\mathrm{f}} - \mathbf{u}_{\mathrm{m}}^1\right)\right] \cdot \left[\mathbf{n} \times \left(\mathbf{v}_{\mathrm{f}} - \mathbf{v}_{\mathrm{m}}^1\right)\right] \mathrm{d}S +
$$

$$
\int_{\Gamma_{01}} \left\{ \left[\mathbf{n} \times \left(\mathbf{u}_{\mathrm{m}}^0 - \mathbf{u}_{\mathrm{m}}^1\right)\right] \cdot \left[\mathbf{n} \times \left(\mathbf{v}_{\mathrm{m}}^0 - \mathbf{v}_{\mathrm{m}}^1\right)\right] + \left[\boldsymbol{\gamma}_{\mathrm{m}} \left(\mathbf{u}_{\mathrm{m}}^0 - \mathbf{u}_{\mathrm{m}}^1\right)\right] \cdot \left[\boldsymbol{\gamma}_{\mathrm{m}} \left(\mathbf{v}_{\mathrm{m}}^0 - \mathbf{v}_{\mathrm{m}}^1\right)\right] + \right.
$$

$$
\left. \left[\mathbf{n} \cdot \left(\mathbf{u}_{\mathrm{m}}^0 - \mathbf{u}_{\mathrm{m}}^1\right)\right] \cdot \left[\mathbf{n} \cdot \left(\mathbf{v}_{\mathrm{m}}^0 - \mathbf{v}_{\mathrm{m}}^1\right)\right] \right\} \mathrm{d}S,
$$

$$\tag{3.14}$$

$$
\mathrm{b}_{\mathrm{LS}}\left[\left(\mathbf{u}_{\mathrm{f}}, \mathbf{u}_{\mathrm{m}}^0, \mathbf{u}_{\mathrm{m}}^1, \phi_{\mathrm{f}}\right), (\mathbf{q}_{\mathrm{f}}, \zeta_{\mathrm{f}})\right] :=
$$

$$
\int_{\Omega_{\mathrm{f}}} \left[\left(\mathbf{M}_\mu^{-1} \nabla \times \mathbf{u}_{\mathrm{f}}\right) \cdot \left(\nabla \times \mathbf{q}_{\mathrm{f}}\right) - \omega^2 \left(\mathbf{M}_\epsilon \mathbf{u}_{\mathrm{f}}\right) \cdot \mathbf{q}_{\mathrm{f}}\right] \mathrm{d}\mathbf{x} + \sum_{i=0,1} \int_{\Gamma_{\mathrm{f}i}} \boldsymbol{\gamma}_{\mathrm{m}} \mathbf{u}_{\mathrm{m}}^i \cdot \mathbf{q}_{\mathrm{f}} \, \mathrm{d}S +
$$

$$
\int_{\Omega_{\mathrm{f}}} \nabla \phi_{\mathrm{f}} \cdot \mathbf{q}_{\mathrm{f}} + \int_{\Omega_{\mathrm{f}}} \mathbf{u}_{\mathrm{f}} \cdot \nabla \zeta_{\mathrm{f}} \, \mathrm{d}\mathbf{x} - \sum_{i=0,1} \int_{\Gamma_{\mathrm{f}i}} \left(\mathbf{n} \cdot \mathbf{u}_{\mathrm{m}}^i\right) \zeta_{\mathrm{f}} \, \mathrm{d}S.
$$

$$\tag{3.15}$$

We propose the following discretization for (3.13):

- $\mathbf{u}_{\mathrm{f}}, \mathbf{v}_{\mathrm{f}}, \mathbf{p}_{\mathrm{f}}, \mathbf{q}_{\mathrm{f}} \in \mathbf{V}^n(\mathcal{M}_{\mathrm{f}})$, see (1.14b),

- $\phi_{\mathrm{f}}, \psi_{\mathrm{f}}, \xi_{\mathrm{f}}, \zeta_{\mathrm{f}} \in V^n(\mathcal{M}_{\mathrm{f}})$, see (1.14a),

- $\mathbf{u}_{\mathrm{m}}^0, \mathbf{v}_{\mathrm{m}}^0 \in \boldsymbol{\mathcal{T}}^n(\Omega_{\mathrm{m}}^0)$, and

- $\mathbf{u}_{\mathrm{m}}^1, \mathbf{v}_{\mathrm{m}}^1 \in \boldsymbol{\mathcal{T}}^n(\Omega_{\mathrm{m}}^1)$.

3.2 Discontinuous Galerkin

3.2.1 Poisson's Equation

Discontinuous Galerkin (DG) methods allow to use FEM with nonconforming meshes on different neighboring domains for the same boundary value problem [5]. This is well-suited for the coupling because one can think of MMP as FEM with special trial and test functions used on a "mesh" with one entity, Ω_{m}. More specifically, we want to impose weak continuity of the tangential traces (1.12a) by a DG method [25].

Following this idea, the coupling can be expressed as a *discrete* stationary problem for the following Lagrangian:[3]

$$\mathrm{L}(u_{\mathrm{f}}^n, u_{\mathrm{m}}^n) := \mathrm{J}_{\Omega_{\mathrm{f}}}(u_{\mathrm{f}}^n) + \mathrm{J}_{\Omega_{\mathrm{m}}}(u_{\mathrm{m}}^n) + \int_{\Gamma} (u_{\mathrm{f}}^n - u_{\mathrm{m}}^n)\, \mathrm{P}^n(u_{\mathrm{f}}^n, u_{\mathrm{m}}^n)\, \mathrm{d}S. \qquad (3.16)$$

We propose $u_{\mathrm{f}}^n \in V^n(\mathcal{M}_{\mathrm{f}})$ (1.14a) and $u_{\mathrm{m}}^n \in \mathcal{T}^n(\Omega_{\mathrm{m}})$.

Let us first discuss functionals $\mathrm{J}_{\Omega_{\mathrm{f}}}, \mathrm{J}_{\Omega_{\mathrm{m}}}$ in the continuous case, then the discrete operator P^n.

Functionals $\mathrm{J}_{\Omega_{\mathrm{f}}}, \mathrm{J}_{\Omega_{\mathrm{m}}}$

$\mathrm{J}_{\Omega_{\mathrm{f}}}$ expresses the saddle-point problem that corresponds to (1.1a) in Ω_{f}:

$$\mathrm{J}_{\Omega_{\mathrm{f}}}(u_{\mathrm{f}}) := \frac{1}{2} \int_{\Omega_{\mathrm{f}}} \left(\mathbf{M}_{\mu}^{-1} \nabla u_{\mathrm{f}} \right) \cdot \nabla u_{\mathrm{f}}\, \mathrm{d}\mathbf{x} - \int_{\Omega_{\mathrm{f}}} j\, u_{\mathrm{f}}\, \mathrm{d}\mathbf{x}. \qquad (3.17a)$$

$\mathrm{J}_{\Omega_{\mathrm{m}}}$ for u_{m} has a similar formulation, but for constant scalar coefficients and no sources:

$$\mathrm{J}_{\Omega_{\mathrm{m}}}(u_{\mathrm{m}}) := \frac{1}{2} \int_{\Omega_{\mathrm{m}}} \mu_i^{-1} \|\nabla u_{\mathrm{m}}\|_{\ell^2}^2\, \mathrm{d}\mathbf{x}. \qquad (3.17b)$$

Because $u_{\mathrm{m}} \in \mathcal{T}(\Omega_{\mathrm{m}})$, one can rewrite the volume integral in (3.17b) as a boundary integral:

$$\frac{1}{2} \int_{\Omega_{\mathrm{m}}} \mu_i^{-1} \|\nabla u_{\mathrm{m}}\|_{\ell^2}^2\, \mathrm{d}\mathbf{x} = \frac{1}{2} \int_{\Gamma} \gamma_{\mathrm{N}} u_{\mathrm{m}}\, u_{\mathrm{m}}\, \mathrm{d}S. \qquad (3.18)$$

---

[3] A Lagrangian formulation for DG is given in [12, p. 21 and 28].

Operator P^n

Let us now go back to the Lagrangian functional (3.16). Depending on the choice of its discrete operator

$$\mathrm{P}^n \colon (V^n(\mathcal{M}_\mathrm{f}) + \mathcal{T}^n(\Omega_\mathrm{m})) \times (V^n(\mathcal{M}_\mathrm{f}) + \mathcal{T}^n(\Omega_\mathrm{m})) \to (V^n(\mathcal{M}_\mathrm{f}) + \mathcal{T}^n(\Omega_\mathrm{m})), \tag{3.19a}$$

we obtain different DG approaches. We follow the (symmetric) *Interior Penalty DG method* [80]:

$$\mathrm{P}^n(u^n, v^n) := -\,\mathbf{n} \cdot \overline{\mu}^{-1} \nabla(u^n + v^n) + \eta\, \overline{\mu}^{-1}(u^n - v^n). \tag{3.19b}$$

- $\overline{\mu}(\mathbf{x}) \colon \mathbb{R}^d \to \mathbb{C}$, $d = 2, 3$, is the mean of material parameters μ in Ω_f and Ω_m when integrating on Γ:

$$\overline{\mu}(\mathbf{x}) := \frac{\mu(\mathbf{x}) + \mu\,\mathbf{I}}{2} \quad \forall\, \mathbf{x} \in \Gamma. \tag{3.20}$$

- $\eta \in \mathbb{R}$ is a penalty parameter that needs to be assigned heuristically. η should be proportional to N_m/h, where N_m is the number of degrees of freedom of $\mathcal{T}^n(\Omega_\mathrm{m})$ and $h \in \mathbb{R}$ the meshwidth of $\mathcal{M}_\mathrm{f}$ restricted to Γ. This choice is inspired by $\eta \sim p/h$, used in case of polynomial DG–FEM [82, p. 229] (with $p \in \mathbb{N}^*$ the polynomial degree).

Saddle-Point Problem

Finding the stationary point of (3.16) leads to the discrete symmetric problem

$$\text{Seek } u_\mathrm{f}^n \in V^n(\mathcal{M}_\mathrm{f}),\ u_\mathrm{m}^n \in \mathcal{T}^n(\Omega_\mathrm{m})\colon$$

$$\mathrm{a}_\mathrm{DG}^n \left[(u_\mathrm{f}^n, u_\mathrm{m}^n), (v_\mathrm{f}^n, v_\mathrm{m}^n) \right] = \int_{\Omega_\mathrm{f}} j\, v_\mathrm{f}^n\, \mathrm{d}\mathbf{x} \tag{3.21}$$

$$\forall v_\mathrm{f}^n \in V^n(\mathcal{M}_\mathrm{f}),\ \forall v_\mathrm{m}^n \in \mathcal{T}^n(\Omega_\mathrm{m}),$$

where we define the symmetric bilinear form $\mathrm{a}_{\mathrm{DG}}^n(\cdot, \cdot)$ as

$$\mathrm{a}_{\mathrm{DG}}^n\left[(u_{\mathrm{f}}^n, u_{\mathrm{m}}^n), (v_{\mathrm{f}}^n, v_{\mathrm{m}}^n)\right] := \int_{\Omega_{\mathrm{f}}} \left(\mathbf{M}_\mu^{-1} \nabla u_{\mathrm{f}}^n\right) \cdot \nabla v_{\mathrm{f}}^n \, \mathrm{d}\mathbf{x} -$$

$$\int_\Gamma \left\{ [\gamma_{\mathrm{N}}(u_{\mathrm{f}}^n + u_{\mathrm{m}}^n)] \, (v_{\mathrm{f}}^n - v_{\mathrm{m}}^n) + (u_{\mathrm{f}}^n - u_{\mathrm{m}}^n) \, [\gamma_{\mathrm{N}}(v_{\mathrm{f}}^n + v_{\mathrm{m}}^n)] \right\} \, \mathrm{d}S + \qquad (3.22)$$

$$\int_\Gamma 2\, \eta \, (u_{\mathrm{f}}^n - u_{\mathrm{m}}^n) \, (v_{\mathrm{f}}^n - v_{\mathrm{m}}^n) \, \mathrm{d}S + \int_\Gamma \gamma_{\mathrm{N}} u_{\mathrm{m}} \, v_{\mathrm{m}} \, \mathrm{d}S.$$

3.2.2 Maxwell's Equations

Discontinuous Galerkin (DG) methods allow to use FEM with nonconforming meshes on different neighboring domains for the same boundary value problem [5]. This is well-suited for the coupling because one can think of MMP as FEM with special trial and test functions used on a "mesh" with two entities: Ω_{m}^0 and Ω_{m}^1. More specifically, we want to impose weak continuity of the tangential traces (1.12a) by a DG method [25].

Following this idea, the coupling can be expressed as a *discrete* stationary problem for the following Lagrangian:[4]

$$\mathrm{L}(\mathbf{u}_{\mathrm{f}}^n, \mathbf{u}_{\mathrm{m}}^{n,0}, \mathbf{u}_{\mathrm{m}}^{n,1}, \phi_{\mathrm{f}}^n, \phi_{\mathrm{m}}^{n,0}, \phi_{\mathrm{m}}^{n,1}) := \mathrm{J}_{\Omega_{\mathrm{f}}}(\mathbf{u}_{\mathrm{f}}^n, \phi_{\mathrm{f}}^n) + \mathrm{J}_{\Omega_{\mathrm{m}}}(\mathbf{u}_{\mathrm{m}}^{n,0}, \mathbf{u}_{\mathrm{m}}^{n,1}, \phi_{\mathrm{m}}^{n,0}, \phi_{\mathrm{m}}^{n,1}) +$$

$$\sum_{i=0,1} \int_{\Gamma_{\mathrm{f}i}} \left[\mathbf{n} \times \left(\mathbf{u}_{\mathrm{f}}^n - \mathbf{u}_{\mathrm{m}}^{n,i}\right)\right] \cdot \mathbf{P}^n(\mathbf{u}_{\mathrm{f}}^n, \mathbf{u}_{\mathrm{m}}^{n,i}) \, \mathrm{d}S +$$

$$\int_{\Gamma_{01}} \left[\mathbf{n} \times \left(\mathbf{u}_{\mathrm{m}}^{n,0} - \mathbf{u}_{\mathrm{m}}^{n,1}\right)\right] \cdot \mathbf{P}^n(\mathbf{u}_{\mathrm{m}}^{n,0}, \mathbf{u}_{\mathrm{m}}^{n,1}) \, \mathrm{d}S.$$

$$(3.23)$$

We propose $\mathbf{u}_{\mathrm{f}}^n \in \mathbf{V}^n(\mathcal{M}_{\mathrm{f}})$ (1.14b), $\mathbf{u}_{\mathrm{m}}^{n,0} \in \boldsymbol{\mathcal{T}}^n(\Omega_{\mathrm{m}}^0)$, $\mathbf{u}_{\mathrm{m}}^{n,1} \in \boldsymbol{\mathcal{T}}^n(\Omega_{\mathrm{m}}^1)$, and $\phi_{\mathrm{f}}^n \in V^n(\mathcal{M}_{\mathrm{f}})$ (1.14a). However, to discretize $\phi_{\mathrm{m}}^{n,0}, \phi_{\mathrm{m}}^{n,1}$, we first need to discuss functionals $\mathrm{J}_{\Omega_{\mathrm{f}}}, \mathrm{J}_{\Omega_{\mathrm{m}}}$ in the continuous case; the discrete operator $\mathbf{P}^n$ is discussed at a later stage.

---

[4]A Lagrangian formulation for DG is given in [12, p. 21 and 28].

Functionals $J_{\Omega_f}, J_{\Omega_m}$

J_{Ω_f} expresses the saddle-point problem that corresponds to (1.3a) in Ω_f:

$$J_{\Omega_f}(\mathbf{u}_f, \phi_f) := \frac{1}{2} \int_{\Omega_f} \left[\left(\mathbf{M}_\mu^{-1} \nabla \times \mathbf{u}_f \right) \cdot \left(\nabla \times \mathbf{u}_f \right) - \omega^2 \left(\mathbf{M}_\epsilon \mathbf{u}_f \right) \cdot \mathbf{u}_f \right] \mathrm{d}\mathbf{x} +$$

$$\int_{\Omega_f} \mathbf{u}_f \cdot \nabla \phi_f \, \mathrm{d}\mathbf{x} - \int_{\Omega_f} \mathbf{j} \cdot \mathbf{u}_f \, \mathrm{d}\mathbf{x}. \qquad (3.24a)$$

J_{Ω_m} for $\mathbf{u}_m^0, \mathbf{u}_m^1$ has a similar formulation, but for constant scalar coefficients and no sources:

$$J_{\Omega_m}(\mathbf{u}_m^0, \mathbf{u}_m^1, \phi_m^0, \phi_m^1) := \sum_{i=0,1} \frac{1}{2} \int_{\Omega_m^i} \left(\mu_i^{-1} \|\nabla \times \mathbf{u}_m^i\|_{\ell^2}^2 - \omega^2 \epsilon_i \|\mathbf{u}_m^i\|_{\ell^2}^2 \right) \mathrm{d}\mathbf{x} +$$

$$\sum_{i=0,1} \int_{\Omega_m^i} \mathbf{u}_m^i \cdot \nabla \phi_m^i \, \mathrm{d}\mathbf{x}. \qquad (3.24b)$$

Because $\mathbf{u}_m^i \in \mathcal{T}(\Omega_m^i)$, $i = 0, 1$, one can rewrite the volume integrals in (3.24b) as boundary integrals:

$$\frac{1}{2} \int_{\Omega_m^i} \left(\mu_i^{-1} \|\nabla \times \mathbf{u}_m^i\|_{\ell^2}^2 - \omega^2 \epsilon_i \|\mathbf{u}_m^i\|_{\ell^2}^2 \right) \mathrm{d}\mathbf{x} = -\frac{1}{2} \int_{\partial\Omega_m^i} \boldsymbol{\gamma}_m \mathbf{u}_m^i \cdot \mathbf{u}_m^i \, \mathrm{d}S,$$
$$(3.25a)$$

$$\int_{\Omega_m^i} \mathbf{u}_m^i \cdot \nabla \phi_m^i \, \mathrm{d}\mathbf{x} = \int_{\partial\Omega_m^i} \left(\mathbf{n} \cdot \mathbf{u}_m^i \right) \phi_m^i \, \mathrm{d}S. \quad (3.25b)$$

Normal Continuity

From (3.25b), by considering only the integrals on each $\Gamma_{fi} := \partial\Omega_f \cap \partial\Omega_m^i$, $i = 0, 1$, taking $\mathbf{n}$ always pointing from Ω_f to Ω_m^i, and setting $\phi_m^i|_{\Gamma_{fi}} = \phi_f|_{\Gamma_{fi}}$, from (3.25b) one can extract the terms

$$- \sum_{i=0,1} \int_{\Gamma_{fi}} \left(\mathbf{n} \cdot \mathbf{u}_m^i \right) \phi_f \, \mathrm{d}S, \qquad (3.26a)$$

which is like imposing (1.12c) on each $\Gamma_{\text{f}i}$ by inserting[5] the MMP ansatz in the boundary terms of the second line of the variational form (1.13b), as done in (3.1b). Furthermore, by considering only the integrals on $\Gamma_{01} := \partial\Omega_{\text{m}}^0 \cap \partial\Omega_{\text{m}}^1$, taking the same $\mathbf{n}$ on both sides of Γ_{01}, and defining $\phi_{\text{m}}^{01} := \phi_{\text{m}}^0\big|_{\Gamma_{01}} = \phi_{\text{m}}^1\big|_{\Gamma_{01}}$, from (3.25b) one can also extract

$$\int_{\Gamma_{01}} \left(\mathbf{n} \cdot \mathbf{u}_{\text{m}}^0 - \mathbf{n} \cdot \mathbf{u}_{\text{m}}^i \right) \phi_{\text{m}}^{01} \, \mathrm{d}S, \tag{3.26b}$$

which is like imposing (1.12c) on Γ_{01} by means of a Lagrange multiplier $\phi_{\text{m}}^{01} \in H^{\frac{1}{2}}(\Gamma_{01})$. Thus, we can rewrite (3.25b) as

$$\sum_{i=0,1} \int_{\partial\Omega_{\text{m}}^i} \left(\mathbf{n} \cdot \mathbf{u}_{\text{m}}^i \right) \phi_{\text{m}}^i \, \mathrm{d}S = - \sum_{i=0,1} \int_{\Gamma_{\text{f}i}} \left(\mathbf{n} \cdot \mathbf{u}_{\text{m}}^i \right) \phi_{\text{f}} \, \mathrm{d}S + \\ \int_{\Gamma_{01}} \left(\mathbf{n} \cdot \mathbf{u}_{\text{m}}^0 - \mathbf{n} \cdot \mathbf{u}_{\text{m}}^1 \right) \phi_{\text{m}}^{01} \, \mathrm{d}S. \tag{3.27}$$

To discretize $\phi_{\text{m}}^{01} \in H^{\frac{1}{2}}(\Gamma_{01})$, we use Dirichlet traces of $\mathbf{n} \cdot \mathbf{v}_{\text{m}}$ on Γ_{01}, given $\mathbf{v}_{\text{m}} \in \boldsymbol{\mathcal{T}}^n(\Omega_{\text{m}}^0)$ or $\boldsymbol{\mathcal{T}}^n(\Omega_{\text{m}}^1)$, and define this discrete trace space as $\mathcal{T}^n(\Gamma_{01})$. This choice of $\mathcal{T}^n(\Gamma_{01})$ is consistent with:

- The PDE-constrained least-squares coupling approach of Section 3.1.2: the same test functions in $\mathcal{T}^n(\Gamma_{01})$ are chosen to impose (1.12c) on Γ_{01} through (3.11) – see (3.14).

- *Mortar element methods* (Section 3.3). In fact, these methods impose weak continuity between nonconforming meshes by a Lagrange multiplier discretized by traces of functions belonging to one of the discretization spaces of the neighboring domains, here Ω_{m}^0 or Ω_{m}^1 [14, p. 100, Remark].

Operator $\mathbf{P}^n$

Let us now go back to the Lagrangian functional (3.23). Depending on the choice of its discrete operator

$$\mathbf{P}^n \colon \left(\mathbf{V}^n(\mathcal{M}_{\text{f}}) + \boldsymbol{\mathcal{T}}^n(\Omega_{\text{m}}^i) \right) \times \left(\mathbf{V}^n(\mathcal{M}_{\text{f}}) + \boldsymbol{\mathcal{T}}^n(\Omega_{\text{m}}^i) \right) \to \left(\mathbf{V}^n(\mathcal{M}_{\text{f}}) + \boldsymbol{\mathcal{T}}^n(\Omega_{\text{m}}^i) \right), \tag{3.28a}$$

---

[5]The minus sign is due to flipping the direction of $\mathbf{n}$, which now points from Ω_{f} to Ω_{m}^i, $i = 0, 1$, for this integral.

$i = 1, 2$, we obtain different DG approaches. We follow the (symmetric) *Interior Penalty DG method* [80]:

$$\mathbf{P}^n(\mathbf{u}^n, \mathbf{v}^n) := \overline{\mathbf{M}}_\mu^{-1}[\nabla \times (\mathbf{u}^n + \mathbf{v}^n)] + \eta \, \overline{\mathbf{M}}_\mu^{-1}[\mathbf{n} \times (\mathbf{u}^n - \mathbf{v}^n)]. \tag{3.28b}$$

- $\overline{\mathbf{M}}_\mu(\mathbf{x}) \colon \mathbb{R}^3 \to \mathbb{C}^{3,3}$ is the mean of material parameters $\mathbf{M}_\mu$ in Ω_f and Ω_m^i when integrating on each $\Gamma_{\mathrm{f}i}$, $i = 0, 1$:

$$\overline{\mathbf{M}}_\mu(\mathbf{x}) := \frac{\mathbf{M}_\mu(\mathbf{x}) + \mu_i \, \mathbf{I}}{2} \quad \forall \, \mathbf{x} \in \Gamma_{\mathrm{f}i}, \tag{3.29}$$

  and of $\mathbf{M}_\mu$ in Ω_m^0 and Ω_m^1 when integrating on Γ_{01}:

$$\overline{\mathbf{M}}_\mu(\mathbf{x}) := \frac{\mu_0 + \mu_1}{2} \, \mathbf{I} \qquad \forall \, \mathbf{x} \in \Gamma_{01}. \tag{3.30}$$

- $\eta \in \mathbb{R}$ is a penalty parameter that needs to be assigned heuristically. On any $\Gamma_{\mathrm{f}i}$, $i = 0, 1$, η should be proportional to N_m^i/h, where N_m^i is the number of degrees of freedom of $\mathcal{T}^n(\Omega_\mathrm{m}^i)$ and $h \in \mathbb{R}$ the meshwidth of $\mathcal{M}_\mathrm{f}$ restricted to $\Gamma_{\mathrm{f}i}$. On Γ_{01}, η should be proportional to $N_\mathrm{m}^0 + N_\mathrm{m}^1$. Both choices are inspired by $\eta \sim p/h$, used in case of polynomial DG–FEM [82, p. 229] (with $p \in \mathbb{N}^*$ the polynomial degree).

Saddle-Point Problem

Finding the stationary point of (3.23) leads to the discrete saddle-point problem

Seek $\mathbf{u}_\mathrm{f}^n \in \mathbf{V}^n(\mathcal{M}_\mathrm{f})$, $\mathbf{u}_\mathrm{m}^{n,0} \in \mathcal{T}^n(\Omega_\mathrm{m}^0)$, $\mathbf{u}_\mathrm{m}^{n,1} \in \mathcal{T}^n(\Omega_\mathrm{m}^1)$, $\phi_\mathrm{f}^n \in V^n(\mathcal{M}_\mathrm{f})$, $\phi_\mathrm{m}^{n,01} \in \mathcal{T}^n(\Gamma_{01})$:

$$\begin{cases} \mathrm{a}_{\mathrm{DG}}^n[(\mathbf{u}_\mathrm{f}^n, \mathbf{u}_\mathrm{m}^{n,0}, \mathbf{u}_\mathrm{m}^{n,1}), (\mathbf{v}_\mathrm{f}^n, \mathbf{v}_\mathrm{m}^{n,0}, \mathbf{v}_\mathrm{m}^{n,1})] + \mathrm{b}_{\mathrm{DG}}^n[(\mathbf{v}_\mathrm{f}^n, \mathbf{v}_\mathrm{m}^{n,0}, \mathbf{v}_\mathrm{m}^{n,1}), (\phi_\mathrm{f}^n, \phi_\mathrm{m}^{n,01})] = \int_{\Omega_\mathrm{f}} \mathbf{j} \cdot \mathbf{v}_\mathrm{f}^n \, \mathrm{d}\mathbf{x} \\ \mathrm{b}_{\mathrm{DG}}^n[(\mathbf{u}_\mathrm{f}^n, \mathbf{u}_\mathrm{m}^{n,0}, \mathbf{u}_\mathrm{m}^{n,1}), (\psi_\mathrm{f}^n, \psi_\mathrm{m}^{n,01})] \hspace{4.5cm} = 0 \end{cases}$$
$$\forall \mathbf{v}_\mathrm{f}^n \in \mathbf{V}^n(\mathcal{M}_\mathrm{f}), \, \forall \mathbf{v}_\mathrm{m}^{n,0} \in \mathcal{T}^n(\Omega_\mathrm{m}^0), \, \forall \mathbf{v}_\mathrm{m}^{n,1} \in \mathcal{T}^n(\Omega_\mathrm{m}^1), \, \forall \psi_\mathrm{f}^n \in V^n(\mathcal{M}_\mathrm{f}), \, \forall \psi_\mathrm{m}^{n,01} \in \mathcal{T}^n(\Gamma_{01}), \tag{3.31}$$

where we define the symmetric bilinear form $a_{DG}^n(\cdot, \cdot)$ and linear form $b_{DG}^n(\cdot, \cdot)$ as

$$
a_{DG}^n \left[\left(\mathbf{u}_f^n, \mathbf{u}_m^{n,0}, \mathbf{u}_m^{n,1} \right), \left(\mathbf{v}_f^n, \mathbf{v}_m^{n,0}, \mathbf{v}_m^{n,1} \right) \right] :=
$$

$$
\int_{\Omega_f} \left[\left(\mathbf{M}_\mu^{-1} \nabla \times \mathbf{u}_f^n \right) \cdot \left(\nabla \times \mathbf{v}_f^n \right) - \omega^2 \left(\mathbf{M}_\epsilon \mathbf{u}_f^n \right) \cdot \mathbf{v}_f^n \right] d\mathbf{x} +
$$

$$
\sum_{i=0,1} \int_{\Gamma_{fi}} \left\{ \left[\overline{\mathbf{M}}_\mu^{-1} \nabla \times \left(\mathbf{u}_f^n + \mathbf{u}_m^{n,i} \right) \right] \cdot \left[\mathbf{n} \times \left(\mathbf{v}_f^n - \mathbf{v}_m^{n,i} \right) \right] + \left[\mathbf{n} \times \left(\mathbf{u}_f^n - \mathbf{u}_m^{n,i} \right) \right] \cdot \left[\overline{\mathbf{M}}_\mu^{-1} \nabla \times \left(\mathbf{v}_f^n + \mathbf{v}_m^{n,i} \right) \right] \right\} dS +
$$

$$
\sum_{i=0,1} \int_{\Gamma_{fi}} 2\,\eta \left[\overline{\mathbf{M}}_\mu^{-1} \mathbf{n} \times \left(\mathbf{u}_f^n - \mathbf{u}_m^{n,i} \right) \right] \cdot \left[\mathbf{n} \times \left(\mathbf{v}_f^n - \mathbf{v}_m^{n,i} \right) \right] dS - \sum_{i=0,1} \int_{\partial\Omega_m^i} \boldsymbol{\gamma}_m \mathbf{u}_m^{n,i} \cdot \mathbf{v}_m^{n,i} \, dS +
$$

$$
\int_{\Gamma_{01}} \left\{ \left[\overline{\mathbf{M}}_\mu^{-1} \nabla \times \left(\mathbf{u}_m^{n,0} + \mathbf{u}_m^{n,1} \right) \right] \cdot \left[\mathbf{n} \times \left(\mathbf{v}_m^{n,0} - \mathbf{v}_m^{n,1} \right) \right] + \left[\mathbf{n} \times \left(\mathbf{u}_m^{n,0} - \mathbf{u}_m^{n,1} \right) \right] \cdot \left[\overline{\mathbf{M}}_\mu^{-1} \nabla \times \left(\mathbf{v}_m^{n,0} + \mathbf{v}_m^{n,1} \right) \right] \right\} dS +
$$

$$
\int_{\Gamma_{01}} 2\,\eta \left[\overline{\mathbf{M}}_\mu^{-1} \mathbf{n} \times \left(\mathbf{u}_m^{n,0} - \mathbf{u}_m^{n,1} \right) \right] \cdot \left[\mathbf{n} \times \left(\mathbf{v}_m^{n,0} - \mathbf{v}_m^{n,1} \right) \right] dS,
$$

$$(3.32)$$

$$
b_{DG}^n \left[\left(\mathbf{u}_f^n, \mathbf{u}_m^{n,0}, \mathbf{u}_m^{n,1} \right), \left(\psi_f^n, \psi_m^{n,01} \right) \right] := \int_{\Omega_f} \mathbf{u}_f^n \cdot \nabla \psi_f^n \, d\mathbf{x} -
$$

$$
\int_{\Gamma_{f0}} \left(\mathbf{n} \cdot \mathbf{u}_m^{n,0} \right) \psi_f^n \, dS - \int_{\Gamma_{f1}} \left(\mathbf{n} \cdot \mathbf{u}_m^{n,1} \right) \psi_f^n \, dS + \int_{\Gamma_{01}} \left(\mathbf{n} \cdot \mathbf{u}_m^{n,0} - \mathbf{n} \cdot \mathbf{u}_m^{n,1} \right) \psi_m^{n,01} \, dS.
$$

$$(3.33)$$

Remark 3.2.1. *The two coupling approaches we describe now can only[6] be used in the case of $m = 0$, i.e. a single (unbounded) Trefftz domain Ω_m^0, which we refer to as Ω_m. This also results in having a single interface $\Gamma \equiv \Gamma_{f0} = \partial\Omega_f = \partial\Omega_m$.*

Moreover, both these methods

1. *impose the continuity of the tangential components trace for Maxwell's equations (1.3), i.e.*

$$
\mathbf{n} \times \left(\mathbf{n} \times \mathbf{u}_f \right)\big|_\Gamma = \mathbf{n} \times \left(\mathbf{n} \times \mathbf{u}_m \right)\big|_\Gamma, \tag{3.34}
$$

instead of the continuity between tangential traces stated in (1.12a), and

---

[6]Except for the multi-field coupling, which can be extended to the case of multiple Trefftz domains for scalar equations (see Section 6.3).

2. *enforce (3.34) (or the continuity between Dirichlet traces (1.10a)) weakly through test functions $\boldsymbol{\gamma}_m \mathbf{v}$, given $\mathbf{v} \in \mathbf{H}_{loc}(\mathbf{curl}, \Omega_\square)$, $\Omega_\square \in \{\Omega_f, \Omega_m\}$ (or $\gamma_N v$, given $v \in H^1_{loc}(\Omega_\square)$).*

3.3 Multi-Field Coupling

3.3.1 Poisson's Equation

As for the DG-based coupling (Section 3.2), we treat the (here single) MMP discretization as a finite element with special functions. However, now we rely on the other main approach for imposing weak continuity on nonconforming meshes, which is the *multi-field domain decomposition method* [20].

For Poisson's equation, the multi-field method aims at imposing the continuity of the Dirichlet trace in a weak sense by means of a Lagrange multiplier

$$\lambda := \gamma_N v, \quad v \in H^1_{\mathrm{loc}}(\Omega), \quad \Omega \subseteq \mathbb{R}^d, \ d = 2, 3. \tag{3.35}$$

From (3.35) one can see that λ belongs to the dual space $H^{-\frac{1}{2}}(\Gamma)$ (see Section 1.3), which is consistent with Dirichlet traces being in $H^{\frac{1}{2}}(\Gamma)$.

The rationale behind the multi-field method becomes clear if one applies the divergence theorem in $H(\nabla^2, \Omega)$ [43, p. 31, (1.56)] to the weak form of (1.1a) in Ω_f, which then leads to the boundary integral

$$\int_\Gamma \gamma_N u_f \ v_f \ \mathrm{d}S. \tag{3.36}$$

Substituting v_m into (3.36) for the continuity of Dirichlet traces, as done in (3.1a), we can understand the reason for (3.35).

Hence, the multi-field coupling can be expressed by the following Lagrangian:

$$\mathrm{L}(u_f, u_m, \lambda) := \mathrm{J}_{\Omega_f}(u_f) + \mathrm{J}_{\Omega_m}(u_m) + \int_\Gamma (u_f - u_m) \ \lambda \ \mathrm{d}S, \tag{3.37}$$

where J_{Ω_f} and J_{Ω_m} are the same as in (3.17a) and (3.17b). In the same way as (3.18), we can also rewrite the volume integral of J_{Ω_m} as a boundary integral on Γ.

Saddle-Point Problem

We obtain the following saddle-point problem:

Seek $u_\mathrm{f} \in H^1(\Omega_\mathrm{f})$, $u_\mathrm{m} \in \mathcal{T}(\Omega_\mathrm{m})$, $\lambda \in H^{-\frac{1}{2}}(\Gamma)$:

$$
\begin{cases}
\int_{\Omega_\mathrm{f}} \left(\mathbf{M}_\mu^{-1}\nabla u_\mathrm{f}\right) \cdot \nabla v_\mathrm{f} \,\mathrm{d}\mathbf{x} & + \int_\Gamma \lambda\, v_\mathrm{f} \ \mathrm{d}S = \int_{\Omega_\mathrm{f}} j\, v_\mathrm{f} \,\mathrm{d}\mathbf{x} \\
\underset{\Gamma}{\int} \gamma_\mathrm{N} u_\mathrm{m}\, v_\mathrm{m} \,\mathrm{d}S - \int_\Gamma \lambda\, v_\mathrm{m} \,\mathrm{d}S = 0 \\
\int_\Gamma u_\mathrm{f}\, \chi \,\mathrm{d}S - \int_\Gamma u_\mathrm{m}\, \chi \,\mathrm{d}S & = 0
\end{cases}
$$

$$\forall v_\mathrm{f} \in H^1(\Omega_\mathrm{f}),\ \forall v_\mathrm{m} \in \mathcal{T}(\Omega_\mathrm{m}),\ \forall \chi \in H^{-\frac{1}{2}}(\Gamma).$$

$$(3.38)$$

For the discretization of (3.38), we suggest $u_\mathrm{f}, v_\mathrm{f} \in V^n(\mathcal{M}_\mathrm{f})$ of (1.14a) and $u_\mathrm{m}, v_\mathrm{m} \in \mathcal{T}^n(\Omega_\mathrm{m})$, as in Sections 3.1.1 and 3.2.1.

Conversely, the discretization of $\lambda \in H^{-\frac{1}{2}}(\Gamma)$ is a topic debated in the literature [73, Section 4]. In the spirit of *mortar element methods*, we opt for the Dirichlet traces on Γ of the trial space used to discretize one of the neighboring domains [73, p. B426], specifically the Lagrangian space $V^n(\mathcal{M}_\mathrm{f})$, given its higher number of degrees of freedom than $\mathcal{T}^n(\Omega_\mathrm{m})$. Note that this choice, while being the most common discretization strategy [73, Section 4.1], ignores the duality of λ.

Existence, Uniqueness, and Stability

For the Galerkin discretization of (3.38), we replace $H^1(\Omega_\mathrm{f})$ with the Lagrangian finite element space $V^n(\mathcal{M}_\mathrm{f})$ from (1.14a) and $\mathcal{T}(\Omega_\mathrm{m})$ with a finite-dimensional subspace $\mathcal{T}^n(\Omega_\mathrm{m})$, as in Section 3.1.1. For discretizing λ we use the traces of the finite element functions in $V^n(\mathcal{M}_\mathrm{f})$ on Γ.

In order to apply saddle-point theory to (3.38), let us consider the left-hand side of (3.38) and define the following bilinear form:

$$a_\mathrm{MF}\left[(u_\mathrm{f}, u_\mathrm{m}), (v_\mathrm{f}, v_\mathrm{m})\right] := \int_{\Omega_\mathrm{f}} \left(\mathbf{M}_\mu^{-1}\nabla u_\mathrm{f}\right) \cdot \nabla v_\mathrm{f} \,\mathrm{d}\mathbf{x} + \int_\Gamma \gamma_\mathrm{N} u_\mathrm{m}\, v_\mathrm{m} \,\mathrm{d}S. \quad (3.39\mathrm{a})$$

Let us also define

$$b_{\mathrm{MF}}[(u_{\mathrm{f}}, u_{\mathrm{m}}), \chi] := \int_{\Gamma} (u_{\mathrm{f}} - u_{\mathrm{m}}) \, \chi \, \mathrm{d}S. \qquad (3.39\mathrm{b})$$

We restrict ourselves to $d = 3$ and observe that, in this case,

$$a_{\mathrm{MF}}[(u_{\mathrm{f}}, u_{\mathrm{m}}), (v_{\mathrm{f}}, v_{\mathrm{m}})] = \int_{\Omega_{\mathrm{f}}} \left(\mathbf{M}_{\mu}^{-1} \nabla u_{\mathrm{f}}\right) \cdot \nabla u_{\mathrm{f}} \, \mathrm{d}\mathbf{x} + \int_{\Omega_{\mathrm{m}}} \|\nabla u_{\mathrm{m}}\|_{\ell^2}^2 \, \mathrm{d}\mathbf{x}. \qquad (3.40)$$

In the continuous case we have that

$$\ker b_{\mathrm{MF}} = \left\{ v_{\mathrm{f}} \in H^1(\Omega_{\mathrm{f}}), \, v_{\mathrm{m}} \in \mathcal{T}(\Omega_{\mathrm{m}}) \colon v_{\mathrm{f}} = v_{\mathrm{m}} \text{ on } \Gamma \right\} \qquad (3.41)$$

and ellipticity on the kernel is clear because a_{MF} induces a norm on $\ker b_{\mathrm{MF}}$ that is equivalent to the energy norm.

In the discrete case, since $V^n(\mathcal{M}_{\mathrm{f}})$ contains constant functions, the kernel of a_{MF} again contains only piecewise-constant functions inside Ω_{f}, combined with the zero function in Ω_{m}. Obviously, the intersection of this space with the discrete kernel $\ker^n b_{\mathrm{MF}}$ must be trivial. This amounts to ellipticity on the kernel in the discrete case.

The continuous inf-sup condition for b_{MF} is a consequence of the duality of $H^{\frac{1}{2}}(\Gamma)$ and $H^{-\frac{1}{2}}(\Gamma)$.

Finally, we discuss the discrete inf-sup condition for the concrete case of piecewise-linear Lagrangian finite elements on a tetrahedral mesh $\mathcal{M}_{\mathrm{f}}$ of Ω_{f}: $V^n(\mathcal{M}_{\mathrm{f}}) = \mathcal{S}_1^0(\mathcal{M}_{\mathrm{f}})$ of (1.14a). The $H^{-\frac{1}{2}}(\Gamma)$-norm of $\lambda^n \in V^n(\mathcal{M}_{\mathrm{f}})$ can be expressed as

$$\|\lambda^n\|_{H^{-\frac{1}{2}}(\Gamma)} := \sup_{v \in H^{\frac{1}{2}}(\Gamma)} \frac{\int_{\Gamma} Q^n \, v \, \lambda^n \, \mathrm{d}S}{\|v\|_{H^{\frac{1}{2}}(\Gamma)}} \leq C \sup_{v \in H^{\frac{1}{2}}(\Gamma)} \frac{\int_{\Gamma} Q^n \, v \, \lambda^n \, \mathrm{d}S}{\|Q^n \, v\|_{H^{\frac{1}{2}}(\Gamma)}} , \qquad (3.42)$$

where $Q^n \colon L^2(\Gamma) \to V^n|_{\Gamma}$ is the $L^2(\Gamma)$-*orthogonal projection operator* such that, given $u \in L^2(\Gamma)$,

$$Q^n \, u \in V^n|_{\Gamma} \colon \int_{\Gamma} (u - Q^n \, u) \, v^n \, \mathrm{d}S = 0 \quad \forall v^n \in V^n. \qquad (3.43)$$

Under mild assumptions on the surface mesh $\mathcal{M}_f|_\Gamma$, we have that $\|Q^n u_\Gamma\|_{H^1(\Gamma)} \leq C \|u_\Gamma\|_{H^1(\Gamma)} \ \forall u_\Gamma \in H^1(\Gamma), C \in \mathbb{R}^+$ independent of $V^n(\mathcal{M}_f)$ [19, 10, 22]. Appealing to interpolation between $L^2(\Gamma)$ and $H^1(\Gamma)$, we conclude with

$$\|Q^n u_\Gamma\|_{H^{\frac{1}{2}}(\Gamma)} \leq C \|u_\Gamma\|_{H^{\frac{1}{2}}(\Gamma)}, \tag{3.44}$$

which shows (3.42).

3.3.2 Maxwell's Equations

As for the DG-based coupling (Section 3.2), we treat the (here single) MMP discretization as a finite element with special functions. However, now we rely on the other main approach for imposing weak continuity on nonconforming meshes, which is the *multi-field domain decomposition method* [20].

For Maxwell's equations, the multi-field method aims at imposing the continuity of the tangential components trace (3.34) in a weak sense by means of a Lagrange multiplier

$$\boldsymbol{\lambda} := \boldsymbol{\gamma}_m \mathbf{v}, \quad \mathbf{v} \in \mathbf{H}_{loc}(\mathbf{curl}, \Omega), \quad \Omega \subseteq \mathbb{R}^3. \tag{3.45}$$

From (3.45) one can see that $\boldsymbol{\lambda}$ belongs to the dual space $\mathbf{H}^{-\frac{1}{2}}(\mathrm{div}_\Gamma, \Gamma)$ (see Section 1.3), which is consistent with (3.34) connecting traces in $\mathbf{H}^{-\frac{1}{2}}(\mathbf{curl}_\Gamma, \Gamma)$.

The rationale behind the multi-field method becomes clear if one applies the generalized Stokes' theorem in $\mathbf{H}(\mathbf{curl\,curl}, \Omega)$ [67, p. 59, Theorem 3.31] to the weak form of (1.3a) in Ω_f, which then leads to the boundary integral

$$\int_\Gamma \boldsymbol{\gamma}_m \mathbf{u}_f \cdot [\mathbf{n} \times (\mathbf{n} \times \mathbf{v}_f)] \, dS. \tag{3.46}$$

Substituting (3.34) into (3.46), we can understand the reason for (3.45). Then, relying on the definition of $\boldsymbol{\gamma}_m$ (1.9b), (3.46) can be simplified as the boundary integrals of the first line of (3.1b).

Hence, the multi-field coupling can be expressed by the following Lagrangian:

$$L(\mathbf{u}_f, \mathbf{u}_m, \phi_f, \phi_m, \boldsymbol{\lambda}) := J_{\Omega_f}(\mathbf{u}_f, \phi_f) + J_{\Omega_m}(\mathbf{u}_m, \phi_m) + \int_\Gamma \{\mathbf{n} \times [\mathbf{n} \times (\mathbf{u}_f - \mathbf{u}_m)]\} \cdot \boldsymbol{\lambda} \, dS, \tag{3.47}$$

where J_{Ω_f} and J_{Ω_m} are the same as in (3.24a) and (3.24b). In the same way as (3.25), we can also rewrite the volume integrals of J_{Ω_m} as boundary integrals on the single interface Γ and then, as in (3.26a), rename $\phi_m|_\Gamma$ as $\phi_f|_\Gamma$.

Saddle-Point Problem

We obtain the following saddle-point problem:

Seek $\mathbf{u}_f \in \mathbf{H}(\mathbf{curl}, \Omega_f)$, $\mathbf{u}_m \in \boldsymbol{\mathcal{T}}(\Omega_m)$, $\phi_f \in H^1_*(\Omega_f)$, $\boldsymbol{\lambda} \in \widetilde{\mathbf{H}}^{-\frac{1}{2}}(\text{div}_\Gamma, \Gamma)$:

$$
\begin{cases}
a_{MF}[(\mathbf{u}_f, \mathbf{u}_m), (\mathbf{v}_f, \mathbf{v}_m)] + b_{MF}[(\mathbf{v}_f, \mathbf{v}_m), (\phi_f, \boldsymbol{\lambda})] = \int_{\Omega_f} \mathbf{j} \cdot \mathbf{v}_f \, \mathrm{d}\mathbf{x} \\
b_{MF}[(\mathbf{u}_f, \mathbf{u}_m), (\psi_f, \boldsymbol{\chi})] \qquad\qquad\qquad\qquad = 0
\end{cases}
$$

$\forall \mathbf{v}_f \in \mathbf{H}(\mathbf{curl}, \Omega_f)$, $\forall \mathbf{v}_m \in \boldsymbol{\mathcal{T}}(\Omega_m)$, $\forall \psi_f \in H^1_*(\Omega_f)$, $\forall \boldsymbol{\chi} \in \widetilde{\mathbf{H}}^{-\frac{1}{2}}(\text{div}_\Gamma, \Gamma)$,

$$(3.48)$$

where

$$
a_{MF}[(\mathbf{u}_f, \mathbf{u}_m), (\mathbf{v}_f, \mathbf{v}_m)] := \int_{\Omega_f} \left[\left(\mathbf{M}_\mu^{-1} \nabla \times \mathbf{u}_f\right) \cdot (\nabla \times \mathbf{v}_f) - \omega^2 \left(\mathbf{M}_\epsilon \mathbf{u}_f\right) \cdot \mathbf{v}_f \right] \mathrm{d}\mathbf{x} -
$$

$$
\int_\Gamma \boldsymbol{\gamma}_m \mathbf{u}_m \cdot \mathbf{v}_m \, \mathrm{d}S, \qquad\qquad (3.49a)
$$

$$
b_{MF}[(\mathbf{u}_f, \mathbf{u}_m), (\psi_f, \boldsymbol{\chi})] := \int_{\Omega_f} \mathbf{u}_f \cdot \nabla \psi_f \, \mathrm{d}\mathbf{x} - \int_\Gamma (\mathbf{n} \cdot \mathbf{u}_m) \, \psi_f \, \mathrm{d}S +
$$

$$
\int_\Gamma \{\mathbf{n} \times [\mathbf{n} \times (\mathbf{u}_f - \mathbf{u}_m)]\} \cdot \boldsymbol{\chi} \, \mathrm{d}S. \qquad\qquad (3.49b)
$$

For the discretization of (3.48), we suggest $\mathbf{u}_f, \mathbf{v}_f \in \mathbf{V}^n(\mathcal{M}_f)$ of (1.14b), $\phi_f, \psi_f \in V^n(\mathcal{M}_f)$ of (1.14a), and $\mathbf{u}_m, \mathbf{v}_m \in \boldsymbol{\mathcal{T}}^n(\Omega_m)$, as in Sections 3.1.2 and 3.2.2.

Conversely, the discretization of $\boldsymbol{\lambda} \in \widetilde{\mathbf{H}}^{-\frac{1}{2}}(\text{div}_\Gamma, \Gamma)$ is a topic debated in the literature [73, Section 4]. In the spirit of *mortar element methods*, we opt for the tangential traces on Γ of the trial space used to discretize one of the neighboring domains [73, p. B426], specifically the Nédélec's space $\mathbf{V}^n(\mathcal{M}_f)$, given its higher number of degrees of freedom than $\boldsymbol{\mathcal{T}}^n(\Omega_m)$.

Note that this choice, while being the most common discretization strategy [73, Section 4.1], ignores the duality of $\boldsymbol{\lambda}$. This nonconforming discretization then

prevents us from extending the multi-field coupling approach to the case with multiple MMP domains. As a matter of fact, a Lagrange multiplier $\boldsymbol{\lambda}_{01} \in \widetilde{\mathbf{H}}^{-\frac{1}{2}}(\mathrm{div}_{\Gamma_{01}}, \Gamma_{01})$, which would impose continuity of tangential components traces between the MMP domains $\Omega_{\mathrm{m}}^0, \Omega_{\mathrm{m}}^1$, would have to be discretized by the tangential traces of either $\boldsymbol{\mathcal{T}}^n(\Omega_{\mathrm{m}}^0)$ or $\boldsymbol{\mathcal{T}}^n(\Omega_{\mathrm{m}}^1)$, the neighboring volume discretization spaces. While on $\Gamma_{\mathrm{f}0}$ and $\Gamma_{\mathrm{f}1}$ the Nédélec's space is the obvious natural decision, no easy choice exists on Γ_{01}.

This is a similar issue that afflicts the discretization of $\psi_{\mathrm{m}}^{n,01}$ for the DG-based coupling (Section 3.2.2). However, in that case only the normal continuity (1.12c) between MMP domains is affected, which is of lesser importance because it comes from a Gauge condition (second line of (1.3a)). On the other hand, the tangential continuity (1.12a) comes from the physically more relevant Ampère's law (first line of (1.3a)).

Remark 3.3.1. *However, numerical results for (scalar) Helmholtz equation in* $\mathbb{R}^2$ *solved by the multi-field coupling proved encouraging for the case of more than one Trefftz domain. These results are reported in Section 6.3 for* $\lambda_{01} \in \widetilde{H}^{-\frac{1}{2}}(\Gamma_{01})$ *discretized by the (Dirichlet) traces of both* $\mathcal{T}^n(\Omega_{\mathrm{m}}^0)$ *and* $\mathcal{T}^n(\Omega_{\mathrm{m}}^1)$.

3.4 DtN-based Coupling

3.4.1 Poisson's Equation

This coupling approach is a special case of the *Trefftz co-chain calculus* presented in Chapter 4, where Trefftz methods are coupled with any numerical method based on volume meshes that fits the framework of co-chain calculus. Obviously, the numerical method here is FEM.

(1.10a) is imposed in weak form by testing it with $\gamma_{\mathrm{N}} v_{\mathrm{m}}$, given $v_{\mathrm{m}} \in \mathcal{T}(\Omega_{\mathrm{m}})$ (compare with (3.35) and (3.36) in Section 3.3.1):

$$\int_{\Gamma} (u_{\mathrm{f}} - u_{\mathrm{m}}) \, \gamma_{\mathrm{N}} v_{\mathrm{m}} \, \mathrm{d}S = 0 \qquad \forall v_{\mathrm{m}} \in \mathcal{T}(\Omega_{\mathrm{m}}). \tag{3.50}$$

Saddle-Point Problem

Combining (3.50) with the variational form (3.1a), we end up with the following system:

$$
\begin{aligned}
&\text{Seek } u_\mathrm{f} \in H^1(\Omega_\mathrm{f}),\, u_\mathrm{m} \in \mathcal{T}(\Omega_\mathrm{m}): \\
&\begin{cases}
\int_{\Omega_\mathrm{f}} \left(\mathbf{M}_\mu^{-1} \nabla u_\mathrm{f} \right) \cdot \nabla v_\mathrm{f}\ \mathrm{d}\mathbf{x} - \int_\Gamma \gamma_\mathrm{N} u_\mathrm{m}\, v_\mathrm{f}\ \mathrm{d}S = \int_{\Omega_\mathrm{f}} j\, v_\mathrm{f}\ \mathrm{d}\mathbf{x} \\
\qquad - \int_\Gamma u_\mathrm{f}\, \gamma_\mathrm{N} v_\mathrm{m}\ \mathrm{d}S + \int_\Gamma u_\mathrm{m}\, \gamma_\mathrm{N} v_\mathrm{m}\ \mathrm{d}S = 0
\end{cases} \\
&\forall v_\mathrm{f} \in H^1(\Omega_\mathrm{f}),\, \forall v_\mathrm{m} \in \mathcal{T}(\Omega_\mathrm{m}).
\end{aligned}
\tag{3.51}
$$

The Galerkin discretization of (3.51) is straightforward: as done before, we replace $H^1(\Omega_\mathrm{f})$ with $V^n(\mathcal{M}_\mathrm{f})$ of (1.14a) and $\mathcal{T}(\Omega_\mathrm{m})$ with a finite-dimensional subspace $\mathcal{T}^n(\Omega_\mathrm{m})$.

Remark 3.4.1. *(3.51) can also be derived by finding a stationary point of the functional*

$$
\mathrm{L}(u_\mathrm{f}, u_\mathrm{m}) := \mathrm{J}_{\Omega_\mathrm{f}}(u_\mathrm{f}) + \mathrm{J}_{\Omega_\mathrm{m}}(u_\mathrm{m}) - \int_\Gamma u_\mathrm{f}\, \gamma_N u_\mathrm{m}\ \mathrm{d}S,
\tag{3.52}
$$

where $\mathrm{J}_{\Omega_\mathrm{f}}$ and $\mathrm{J}_{\Omega_\mathrm{m}}$ are the same as in (3.17a) and (3.17b).

Existence, Uniqueness, and Stability

The analysis of (3.51) on both the continuous and discrete levels is based on splitting $u_\mathrm{f}, v_\mathrm{f} \in H^1(\Omega_\mathrm{f})$ as

$$
\begin{cases}
u_\mathrm{f} = u_\mathrm{f}^\star + \pi \\
v_\mathrm{f} = v_\mathrm{f}^\star + \tau
\end{cases} : u_\mathrm{f}^\star, v_\mathrm{f}^\star \in H_\star^1(\Omega_\mathrm{f}) := \left\{ w \in H^1(\Omega_\mathrm{f}) : \int_{\Omega_\mathrm{f}} w\, \mathrm{d}\mathbf{x} = 0 \right\},\ \pi, \tau \in \mathbb{R},
\tag{3.53}
$$

which leads to the following saddle-point problem:

Seek $u_f^\star \in H_\star^1(\Omega_f)$, $u_m \in \mathcal{T}(\Omega_m)$, $\pi \in \mathbb{R}$:

$$
\begin{cases}
\int_{\Omega_f} \left(\mathbf{M}_\mu^{-1}\nabla u_f^\star\right) \cdot \nabla v_f^\star \, \mathrm{d}\mathbf{x} - \int_\Gamma \gamma_N u_m \, v_f^\star \, \mathrm{d}S &= \int_{\Omega_f} f \, v_f^\star \, \mathrm{d}\mathbf{x} \\
\quad - \int_\Gamma u_f^\star \gamma_N v_m \, \mathrm{d}S + \int_\Gamma u_m \, \gamma_N v_m \, \mathrm{d}S - \int_\Gamma \pi \, \gamma_N v_m \, \mathrm{d}S = 0 \\
\quad\quad - \int_\Gamma \gamma_N u_m \, \mathrm{d}S &= \int_{\Omega_f} f \, \mathrm{d}\mathbf{x}
\end{cases}
$$

$\forall v_f^\star \in H_\star^1(\Omega_f)$, $\forall v_m \in \mathcal{T}(\Omega_m)$.

$$(3.54)$$

Galerkin discretization of (3.54) is straightforward: as in Sections 3.1.1, 3.2.1, and 3.3.1, we replace $H^1(\Omega_f)$ with the Lagrangian finite element space from (1.14a) and $\mathcal{T}(\Omega_m)$ with a finite-dimensional subspace $\mathcal{T}^n(\Omega_m)$.

To apply saddle-point theory to (3.51), let us define the following operators:

$$
\mathrm{a_{DtN}}[(u_f^\star, u_m), (v_f^\star, v_m)] := \int_{\Omega_f} \left(\mathbf{M}_\mu^{-1}\nabla u_f^\star\right) \cdot \nabla v_f^\star \, \mathrm{d}\mathbf{x} - \int_\Gamma \gamma_N u_m \, v_f^\star \, \mathrm{d}S -
$$

$$
\int_\Gamma u_f^\star \, \gamma_N v_m \, \mathrm{d}S + \int_\Gamma u_m \, \gamma_N v_m \, \mathrm{d}S, \tag{3.55a}
$$

$$
\mathrm{b_{DtN}}(u_m, \pi) := -\int_\Gamma \gamma_N u_m \, \pi \, \mathrm{d}S. \tag{3.55b}
$$

For $u_m \in \ker \mathrm{b_{DtN}}$, we have that $\int_\Gamma \gamma_N u_m \, \mathrm{d}S = 0$, which implies $\nabla u_m(\mathbf{x}) = \mathcal{O}(\|\mathbf{x}\|^{-2})$ for $\|\mathbf{x}\| \to \infty$. As a consequence,

$$
\mathrm{a_{DtN}}[(u_f^\star, u_m), (v_f^\star, v_m)] = \int_{\Omega_f} \left(\mathbf{M}_\mu^{-1}\nabla u_f^\star\right) \cdot \nabla u_f^\star \, \mathrm{d}\mathbf{x} + \int_{\Omega_m} \|\nabla u_m\|_{\ell^2}^2 \, \mathrm{d}\mathbf{x}. \tag{3.56}
$$

This proves ellipticity on the kernel in both the continuous and discrete settings: the variational problems are uniformly stable. The inf-sup condition for $\mathrm{b_{DtN}}$ of (3.55b) is trivial considering that $\pi \in \mathbb{R}$ and $\int_\Gamma \gamma_N u_m \, \mathrm{d}S \neq 0$ for some $u_m \in \mathcal{T}(\Omega_m)$.

Remark 3.4.2. *Summing up, mesh-independent stability can be confirmed for the DtN-based coupling from Section 3.4.1 and the multi-field approach from*

Section 3.3.1, whereas it remains elusive for the PDE-constrained least-squares technique examined in Section 3.1.1. However, numerical tests for Poisson's problem (Section 6.1) do not confirm a superior performance of the two former approaches compared to the latter.

3.4.2 Maxwell's Equations

This coupling approach is a special case of the *Trefftz co-chain calculus* presented in Chapter 4, where Trefftz methods are coupled with any numerical method based on volume meshes that fits the framework of co-chain calculus. Obviously, the numerical method here is FEM.

As mentioned in Remark 3.2.1, instead of the continuity between tangential traces implied by (1.12a), we take into account the continuity of the tangential components trace. (3.34) is then imposed in weak form by testing it with $\boldsymbol{\gamma}_m \mathbf{v}_m$, given $\mathbf{v}_m \in \boldsymbol{\mathcal{T}}(\Omega_m)$ (compare with (3.45) and (3.46) in Section 3.3.2):

$$\int_\Gamma \{[\mathbf{n} \times (\mathbf{n} \times \mathbf{u}_f)] - [\mathbf{n} \times (\mathbf{n} \times \mathbf{u}_m)]\} \cdot \boldsymbol{\gamma}_m \mathbf{v}_m \, \mathrm{d}S = 0 \Longrightarrow$$

$$\int_\Gamma (\mathbf{u}_f - \mathbf{u}_m) \cdot \boldsymbol{\gamma}_m \mathbf{v}_m \, \mathrm{d}S = 0 \qquad \forall \mathbf{v}_m \in \boldsymbol{\mathcal{T}}(\Omega_m), \tag{3.57}$$

which holds because of the definition of $\boldsymbol{\gamma}_m$ (1.9b).

Saddle-Point Problem

Combining (3.57) with the (symmetrized) variational form (3.1b), we end up with the following system:

Seek $\mathbf{u}_f \in \mathbf{H}(\mathbf{curl}, \Omega_f)$, $\mathbf{u}_m \in \boldsymbol{\mathcal{T}}(\Omega_m)$, $\phi_f \in H^1_*(\Omega_f)$:

$$\begin{cases} a_{\mathrm{DtN}}[(\mathbf{u}_f, \mathbf{u}_m), (\mathbf{v}_f, \mathbf{v}_m)] + b_{\mathrm{DtN}}[(\mathbf{v}_f, \mathbf{v}_m), \phi_f] = \int_{\Omega_f} \mathbf{j} \cdot \mathbf{v}_f \, \mathrm{d}\mathbf{x} \\ b_{\mathrm{DtN}}[(\mathbf{u}_f, \mathbf{u}_m), \psi_f] \qquad\qquad\qquad\qquad = 0 \end{cases} \tag{3.58}$$

$$\forall \mathbf{v}_f \in \mathbf{H}(\mathbf{curl}, \Omega_f), \ \forall \mathbf{v}_m \in \boldsymbol{\mathcal{T}}(\Omega_m), \ \forall \psi_f \in H^1_*(\Omega_f),$$

where

$$a^{\mathrm{DtN}}[(\mathbf{u}_f, \mathbf{u}_m), (\mathbf{v}_f, \mathbf{v}_m)] := \int_{\Omega_f} \left[\left(\mathbf{M}_\mu^{-1} \nabla \times \mathbf{u}_f\right) \cdot (\nabla \times \mathbf{v}_f) - \omega^2 \left(\mathbf{M}_\epsilon \mathbf{u}_f\right) \cdot \mathbf{v}_f \right] \mathrm{d}\mathbf{x} +$$

$$\int_\Gamma \mathbf{u}_\mathrm{f} \cdot \boldsymbol{\gamma}_\mathrm{m} \mathbf{v}_\mathrm{m} \,\mathrm{d}S + \int_\Gamma \boldsymbol{\gamma}_\mathrm{m} \mathbf{u}_\mathrm{m} \cdot \mathbf{v}_\mathrm{f} \,\mathrm{d}S - \int_\Gamma \boldsymbol{\gamma}_\mathrm{m} \mathbf{u}_\mathrm{m} \cdot \mathbf{v}_\mathrm{m} \,\mathrm{d}S,$$

$$\tag{3.59a}$$

$$\mathrm{b}^\mathrm{DtN}[(\mathbf{u}_\mathrm{f}, \mathbf{u}_\mathrm{m}), \psi_\mathrm{f}] := \int_{\Omega_\mathrm{f}} \mathbf{u}_\mathrm{f} \cdot \nabla \psi_\mathrm{f} \,\mathrm{d}\mathbf{x} - \int_\Gamma (\mathbf{n} \cdot \mathbf{u}_\mathrm{m}) \, \psi_\mathrm{f} \,\mathrm{d}S. \tag{3.59b}$$

The Galerkin discretization of (3.58) is straightforward: as done before, we replace $\mathbf{H}(\mathbf{curl}, \Omega_\mathrm{f})$ with $\mathbf{V}^n(\mathcal{M}_\mathrm{f})$ of (1.14b), $H^1(\Omega_\mathrm{f})$ with $V^n(\mathcal{M}_\mathrm{f})$ of (1.14a), and $\mathcal{T}(\Omega_\mathrm{m})$ with a finite-dimensional subspace $\mathcal{T}^n(\Omega_\mathrm{m})$.

Remark 3.4.3. *(3.58) can also be derived by finding a stationary point of the functional*

$$\mathrm{L}(\mathbf{u}_\mathrm{f}, \mathbf{u}_\mathrm{m}, \phi_\mathrm{f}, \phi_\mathrm{m}) := \mathrm{J}_{\Omega_\mathrm{f}}(\mathbf{u}_\mathrm{f}, \phi_\mathrm{f}) + \mathrm{J}_{\Omega_\mathrm{m}}(\mathbf{u}_\mathrm{m}, \phi_\mathrm{m}) + \int_\Gamma \mathbf{u}_\mathrm{f} \cdot \boldsymbol{\gamma}_m \mathbf{u}_\mathrm{m} \,\mathrm{d}S, \tag{3.60}$$

where $\mathrm{J}_{\Omega_\mathrm{f}}$ and $\mathrm{J}_{\Omega_\mathrm{m}}$ are the same as in (3.24a) and (3.24b) and ϕ_m disappears by setting $\phi_\mathrm{m}|_\Gamma = \phi_\mathrm{f}|_\Gamma$ as in (3.26a).

4 Trefftz Co-chain Calculus

Here we propose a comprehensive approach to obtain systems of equations that discretize linear stationary or time-harmonic elliptic problems in unbounded domains. This is achieved by coupling any numerical method that fits *co-chain calculus* (Section 4.1) with a Trefftz method. Specifically, in Section 4.2 we present the formalism of co-chain calculus, while Section 4.3 illustrates its coupling with a Trefftz method. Finally, Section 4.4 replaces the equations for the exterior problem with a simpler, but equivalent expression, given a condition on the topology of the Trefftz domain that can always be satisfied.[1]

The coupling proposed here between co-chain calculus and Trefftz functions can be seen as a generalization of the DtN-based coupling presented in Section 3.4 and was developed during a research stay at the University of Padova managed by Prof. F. Moro, whose support we gratefully acknowledge. Our collaboration culminated, together with Prof. L. Codecasa, in [26], which also specializes Sections 4.2 to 4.4 for MMP and the *cell method* [83], another technique based on volume meshes like FEM,[2] and reports numerical results for this coupling. These results are obtained by solving iteratively the Schur complement of the coupling systems: MMP degrees of freedom, thanks to their exponential convergence (Sections 2.3 and 2.4), are so low that they can be eliminated.

4.1 Co-chain Calculus

The framework of co-chain calculus [51, 52] allows for a unified treatment of a wide class of finite element and finite volume schemes, building on the

---

[1]This condition generalizes the concept of simply-connected domains introduced in Remark 1.2.1.

[2]The cell method is coupled with BEM in a way similar to Trefftz co-chain calculus in [68, 69] for, respectively, magnetostatic and eddy-current problems.

foundation established by other works like [17]. Co-chain calculus is the generalization of both *Finite Element Exterior Calculus* (FEEC) [6] and *Discrete Exterior Calculus* (DEC) [56, 77]. The degrees of freedom of the former are coefficients of an expansion in terms of piecewise polynomials built on a mesh: what one obtains is a function approximating the unknown in the chosen functional space, in the way of FEM. Conversely, DEC operates on values of the unknown on entities of (primal and dual) meshes, something more akin to finite difference or finite volume methods.

The starting point of co-chain calculus is a linear stationary or time-harmonic elliptic boundary value problem, more general than (1.3), expressed in terms of differential forms and *Hodge operators* (see Section 4.2). In particular, we distinguish between *equilibrium equations*, stated by means of the exterior derivative, and *constitutive equations*, involving Hodge operators. In the discrete setting, based on meshes, Hodge operators are approximated by matrices, whose construction is done differently in FEEC and DEC, as discussed in [52, Section 4]. Indeed, the discrete matrix forms of co-chain calculus only need to respect a few algebraic requirements, independent of the details of the approximation. These are only addressed when the framework of co-chain calculus is specialized into a numerical method.

Moreover, in order to include both FEEC and DEC, the discrete formalism of co-chain calculus is based on both a primary and a secondary mesh on a bounded domain. Given a numerical method, if its degrees of freedom are defined on either the primary or secondary mesh, we disregard the other mesh and fit the method into FEEC. Conversely, some degrees of freedom may be represented on the primary mesh and others on the secondary mesh. In this case, a bijective relationship between the two types of unknowns is needed, which can be achieved by using a secondary mesh *dual* to the primary mesh. This leads to numerical schemes fitting the framework of DEC, which are called *generalized finite volume methods* in [52], *generalized finite differences* in [17], and *cell method* in [83].

4.2 Formalism

We write $\Lambda^l(\mathbb{R}^n)$ for the space of differential forms of order l, $0 \leq l \leq n$, in $\mathbb{R}^n$, $n \in \mathbb{N}^*$ [6, p. 13, Section 2.2].

The statement of an elliptic boundary value problem is composed of two sets of equations. One is the set of equilibrium equations

$$\begin{cases} \mathrm{d}u = (-1)^l \, \boldsymbol{\sigma}, \\ \mathrm{d}\mathbf{j} = \psi, \end{cases} \tag{4.1a}$$

connecting the differential forms $u \in \Lambda^{l-1}(\mathbb{R}^n)$, $\boldsymbol{\sigma} \in \Lambda^l(\mathbb{R}^n)$, $\mathbf{j} \in \Lambda^m(\mathbb{R}^n)$, $\psi \in \Lambda^{m+1}(\mathbb{R}^n)$ for $l \in \{1, \ldots, n\}$ and $m := n - l$. The other set is formed by the constitutive equations

$$\begin{cases} \mathbf{j} = \star_\alpha \boldsymbol{\sigma}, \\ \psi = \star_\gamma u \,. \end{cases} \tag{4.1b}$$

The symbols $\star_\alpha$ and $\star_\gamma$ indicate Hodge operators, which supply linear mappings of l-forms into m-forms [6, p. 12]. These are induced by the Riemannian metrics α and γ: if $\mathbb{R}^n$ is equipped with Cartesian coordinates, these metrics can be represented by Hermitian positive-definite matrix fields.

The model problem is completed by the condition at infinity [64, p. 259, Theorem 8.9] (compare with (1.1b))

$$\|u(\mathbf{x})\| = \begin{cases} c\log\|\mathbf{x}\| + \mathcal{O}(\|\mathbf{x}\|^{-1}) & \text{if } n = 2, \ c \in \mathbb{R} \\ \mathcal{O}(\|\mathbf{x}\|^{2-n}) & \text{if } n \geq 3 \end{cases} \quad \text{for } \|\mathbf{x}\| \to \infty \text{ uniformly.} \tag{4.2}$$

For the sake of simplicity, we consider a bounded domain $\Omega_\star$ such that, in the complement $\mathbb{R}^n \setminus \Omega_\star$, we have constant $\alpha, \gamma \in \mathbb{C}$. Let us also introduce $\Omega \supseteq \Omega_\star$, in whose complement $\mathbb{R}^n \setminus \Omega$ we are given a known nonzero excitation $(l-1)$-form w such that $u|_{\mathbb{R}^n \setminus \Omega} = v + w$, with $v, w \in \Lambda^{l-1}(\mathbb{R}^n \setminus \Omega)$ and v solving the homogeneous problem. The field w will enter the right-hand side of the system.

Furthermore, we assume that $\gamma = 0$ in $\mathbb{R}^n \setminus \Omega$, which implies $\psi|_{\mathbb{R}^n \setminus \Omega} = 0$ and $\mathrm{d}\mathbf{j}|_{\mathbb{R}^n \setminus \Omega} = 0$ from (4.1a) and (4.1b).

Next, we eliminate all other variables except for u in Ω:

$$\mathrm{d}\left(\star_\alpha \mathrm{d}u\right) = (-1)^l \, \mathrm{d}\left(\star_\alpha \boldsymbol{\sigma}\right) = (-1)^l \, \mathrm{d}\mathbf{j} = (-1)^l \, \psi = (-1)^l \star_\gamma u \,, \qquad (4.3)$$

which can be rewritten as[3]

$$(-1)^{l-1} \, \mathrm{d}\left(\star_\alpha \mathrm{d}u\right) + \star_\gamma u = 0 \,. \qquad (4.5)$$

Multiplication with $\eta \in \Lambda^{l-1}(\Omega)$ and integration on Ω yields

$$\int_\Omega \left[(-1)^{l-1} \, \mathrm{d}\left(\star_\alpha \mathrm{d}u\right) + \star_\gamma u \right] \wedge \eta = 0 \quad \forall \eta \in \Lambda^{l-1}(\Omega). \qquad (4.6)$$

Taking the $\wedge$-product with η and integrating by parts [52, p. 254, (6)], we then obtain the weak formulation

$$\int_\Omega \left(\star_\alpha \mathrm{d}u \wedge \mathrm{d}\eta + \star_\gamma u \wedge \eta\right) + (-1)^{l-1} \int_\Gamma \mathbf{t}\left(\star_\alpha \mathrm{d}u\right) \wedge \mathbf{t}\,\eta = 0 \quad \forall \eta \in \Lambda^{l-1}(\Omega), \,\, (4.7)$$

where $\mathbf{t} \colon \Lambda^l(\Omega) \to \Lambda^l(\Gamma)$ is the (tangential, Dirichlet) trace of l-forms for any $l \in \{1, \dots, n\}$ on $\Gamma := \partial\Omega$.

4.3 Coupling through an $(l-1)$-Form

We discretize Hodge operators inside Ω with meshes (approximation of constitutive equations), while we use Trefftz functions in the complement $\Omega_\mathrm{m} := \mathbb{R}^3 \setminus \Omega$, i.e. functions that belong to the Trefftz space (see Section 2.1)

$$\mathcal{T}(\Omega_\mathrm{m}) := \Big\{ v \in \Lambda^{l-1}(\Omega_\mathrm{m}) \colon \,\, \mathrm{d}\left(\star_\alpha \mathrm{d}v\right) = 0, \,\, \alpha \in \mathbb{C},$$
$$v \text{ satisfies the condition at infinity (4.2)} \Big\}. \qquad (4.8)$$

---

[3]If we take $n = 3$ ($\mathbb{R}^3$), $l = 2$, $m = 1$, and rename $u \in \Lambda^1(\mathbb{R}^3)$ as $\mathbf{u} \colon \mathbb{R}^3 \to \mathbb{C}^3$ and $\star_\alpha, \star_\gamma$ as $\mathbf{M}_\mu^{-1}, -\omega^2 \mathbf{M}_\epsilon \colon \mathbb{R}^3 \to \mathbb{C}^{3,3}$, we obtain the ungauged version of (1.3):

$$\nabla \times \left(\mathbf{M}_\mu^{-1} \nabla \times \mathbf{u}\right) - \omega^2 \mathbf{M}_\epsilon \, \mathbf{u} = \mathbf{0} \,, \qquad (4.4)$$

where the right-hand side $\mathbf{j}$ is replaced by a known offset function as in Sections 2.3.2, 2.4, 6.3, and 6.6.

Interface conditions are required on Γ between Ω and Ω_m, given Lemma 1.3.1:

$$\mathbf{t}\,u|_\Omega = \mathbf{t}\,u|_{\Omega_\mathrm{m}}, \tag{4.9a}$$

$$\mathbf{t}\left(\star_\alpha \mathrm{d}u|_\Omega\right) = \mathbf{t}\left(\star_\alpha \mathrm{d}u|_{\Omega_\mathrm{m}}\right). \tag{4.9b}$$

From now on, with a small abuse of notation, we refer to $u|_\Omega$ as u. We also write $u|_{\Omega_\mathrm{m}} \coloneqq v + w$, where $v \in \mathcal{T}(\Omega_\mathrm{m})$ and w is the known excitation $(l-1)$-form.

We then plug (4.9b) into (4.7) and impose (4.9a) weakly with test functions in $\mathcal{T}(\Omega_\mathrm{m})$ to obtain the system for the coupling:

Seek $u \in \Lambda^{l-1}(\Omega)$, $v \in \mathcal{T}(\Omega_\mathrm{m})$:

$$\begin{cases} \int_\Omega \left(\star_\alpha \mathrm{d}u \wedge \mathrm{d}\eta + \star_\gamma u \wedge \eta\right) + (-1)^{l-1} \int_\Gamma \mathbf{t}\left(\star_\alpha \mathrm{d}v\right) \wedge \mathbf{t}\,\eta = (-1)^l \int_\Gamma \mathbf{t}\left(\star_\alpha \mathrm{d}w\right) \wedge \mathbf{t}\,\eta \\ (-1)^{l-1} \int_\Gamma \mathbf{t}\left(\star_\alpha \mathrm{d}\zeta\right) \wedge \mathbf{t}\,u - (-1)^{l-1} \int_\Gamma \mathbf{t}\left(\star_\alpha \mathrm{d}\zeta\right) \wedge \mathbf{t}\,v = (-1)^{l-1} \int_\Gamma \mathbf{t}\left(\star_\alpha \mathrm{d}\zeta\right) \wedge \mathbf{t}\,w \\ \forall \eta \in \Lambda^{l-1}(\Omega),\ \forall \zeta \in \mathcal{T}(\Omega_\mathrm{m}). \end{cases} \tag{4.10}$$

We choose primary and secondary discretization meshes which can be unrelated [52, p. 250, Definition 2.2]. From now on, quantities linked to the secondary mesh are tagged by a tilde. Then, with the discrete counterpart of the integration by parts formula used in (4.7), we can rewrite (4.10) in abstract algebraic form

$$\left[\left(\mathbf{D}^{l-1}\right)^\mathsf{H}\mathbf{M}_\alpha^l\mathbf{D}^{l-1} + \mathbf{M}_\gamma^{l-1}\right]\vec{\mathbf{u}} + (-1)^{l-1}\left(\mathbf{T}_\Gamma^{l-1}\right)^\mathsf{H}\widetilde{K}_{m,\Gamma}^{l-1}\mathbf{P}_\Gamma\vec{\mathbf{v}} = (-1)^l\left(\mathbf{T}_\Gamma^{l-1}\right)^\mathsf{H}\widetilde{K}_{m,\Gamma}^{l-1}\vec{\boldsymbol{\omega}}$$
$$(-1)^{l-1}\mathbf{P}_\Gamma^\mathsf{H}\left(\widetilde{\mathbf{K}}_{m,\Gamma}^{l-1}\right)^\mathsf{H}\mathbf{T}_\Gamma^{l-1}\vec{\mathbf{u}} - \qquad \mathbf{M}_\mathrm{m}\vec{\mathbf{v}} \qquad = (-1)^{l-1}\mathbf{P}_\Gamma^\mathsf{H}\left(\widetilde{\mathbf{K}}_{m,\Gamma}^{l-1}\right)^\mathsf{H}\vec{\mathbf{w}} \tag{4.11}$$

using the following terms:

- The *exterior-derivative* matrix $\mathbf{D}^{l-1} \in \{-1, 0, 1\}^{N_l, N_{l-1}}$, with N_l number of l-dimensional entities of the primary mesh, is the incidence matrix between oriented l- and $(l-1)$-dimensional entities.

- *Mass* matrices $\mathbf{M}_\alpha^l \in \mathbb{C}^{N_l, N_l}$ and $\mathbf{M}_\gamma^{l-1} \in \mathbb{C}^{N_{l-1}, N_{l-1}}$ need to be square, Hermitian, and positive-definite [52, p. 254]. They can be viewed as discrete Hodge operators.

- We use a vector notation for the coefficient vector $\vec{\mathbf{u}} \in \mathbb{C}^{N_{l-1}}$, whose entries are related to integrals of $u \in \Lambda^{l-1}(\Omega)$ over the $(l-1)$-dimensional entities of the primary mesh. These integrals are regarded as *degrees of freedom.*

- The *trace* matrix $\mathbf{T}_{\Gamma}^{l-1} \in \{0,1\}^{N_{l-1}^{\mathrm{bnd}}, N_{l-1}}$, with N_{l-1}^{bnd} number of $(l-1)$-dimensional primary mesh entities $\subset \Gamma$, selects the degrees of freedom on Γ.

- The *pairing* matrix $\widetilde{\mathbf{K}}_{m,\Gamma}^{l-1} \in \mathbb{C}^{N_{l-1}^{\mathrm{bnd}}, \widetilde{N}_m^{\mathrm{bnd}}}$ is a discrete representative of the $\wedge$-product $\int_{\Gamma} f \wedge g$, $f \in \Lambda^{l-1}(\Omega)$, $g \in \Lambda^m(\Omega)$. Pairing matrices need to fulfill the algebraic relationship [52, p. 254]

$$\widetilde{\mathbf{K}}_m^l = (-1)^{lm} \left(\mathbf{K}_l^m\right)^{\mathsf{H}} \iff \mathbf{K}_l^m = (-1)^{lm} \left(\widetilde{\mathbf{K}}_m^l\right)^{\mathsf{H}} \qquad (4.12)$$

  for any $l \in \{1, \ldots, n\}$, $m \coloneqq n - l$.

- We call $\mathbf{P}_{\Gamma} \in \mathbb{C}^{\widetilde{N}_m^{\mathrm{bnd}}, N_{\mathrm{m}}}$ *Dirichlet-to-Neumann* matrix, with N_{m} dimension of the discrete Trefftz space $\mathcal{T}_n(\Omega_{\mathrm{m}}) \in \mathcal{T}(\Omega_{\mathrm{m}})$. Comparing (4.10) and (4.11), it stands clear that the role of $\mathbf{P}_{\Gamma}$ is to connect the discrete representations of v and $\star_\alpha \mathrm{d}v$ (the latter expressed only by degrees of freedom on Γ).

- $\vec{\mathbf{v}} \in \mathbb{C}^{N_{\mathrm{m}}}$ is the vector of expansion coefficients of $v \in \mathcal{T}_n(\Omega_{\mathrm{m}})$ with respect to a basis of the discrete Trefftz space.

- $\vec{\mathbf{w}} \in \mathbb{C}^{N_{l-1}^{\mathrm{bnd}}}$ and $\vec{\boldsymbol{\omega}} \in \mathbb{C}^{\widetilde{N}_m^{\mathrm{bnd}}}$ are known vectors determined by integrals of the excitation $(l-1)$-form w on $(l-1)$-entities of the primary mesh and by $\star_\alpha \mathrm{d}w$ on m-entities of the secondary mesh, respectively.

- $\mathbf{M}_{\mathrm{m}} \in \mathbb{C}^{N_{\mathrm{m}}, N_{\mathrm{m}}}$ is the *energy* matrix in Ω_{m}, another discrete Hodge operator. This interpretation is clarified below.

We deduce an expression with the energy matrix in Ω_{m} based on the discrete form of (4.7), which is also given in [52, p. 255, *Primary elimination*, (12)]. There, the left-hand side of the resulting linear system is

$$\left[\left(\mathbf{D}^{l-1}\right)^{\mathsf{H}} \mathbf{M}_\alpha^l \mathbf{D}^{l-1} + \mathbf{M}_\gamma^{l-1} + \left(\mathbf{T}_{\Gamma}^{l-1}\right)^{\mathsf{H}} \mathbf{M}_{\beta,\Gamma}^{l-1} \mathbf{T}_{\Gamma}^{l-1}\right] \vec{\mathbf{u}}, \qquad (4.13)$$

where $\mathbf{M}_{\beta,\Gamma}^{l-1}$ is an abstract *boundary-energy* term related to the DtN opera-
tor.

To arrive at an expression involving $\mathbf{M}_{\mathrm{m}} \in \mathbb{C}^{N_{\mathrm{m}},N_{\mathrm{m}}}$, we note that the total
number of degrees of freedom of the Trefftz discretization, N_{m}, is generally
low because, under certain conditions, Trefftz methods enjoy exponential con-
vergence (Sections 2.3 and 2.4). Thus, $\mathbf{M}_{\mathrm{m}}$ can easily be inverted by Gaussian
elimination, and we can write the Schur complement of (4.11):

$$\left[\left(\mathbf{D}^{l-1}\right)^{\mathsf{H}}\mathbf{M}_{\alpha}^{l}\mathbf{D}^{l-1} + \mathbf{M}_{\gamma}^{l-1} + \left(\mathbf{T}_{\Gamma}^{l-1}\right)^{\mathsf{H}}\widetilde{\mathbf{K}}_{m,\Gamma}^{l-1}\mathbf{P}_{\Gamma}\mathbf{M}_{\mathrm{m}}^{-1}\mathbf{P}_{\Gamma}^{\mathsf{H}}\left(\widetilde{\mathbf{K}}_{m,\Gamma}^{l-1}\right)^{\mathsf{H}}\mathbf{T}_{\Gamma}^{l-1}\right]\vec{\mathbf{u}} =$$
$$(-1)^{l}\left(\mathbf{T}_{\Gamma}^{l-1}\right)^{\mathsf{H}}\widetilde{\mathbf{K}}_{m,\Gamma}^{l-1}\vec{\boldsymbol{\omega}} + \left(\mathbf{T}_{\Gamma}^{l-1}\right)^{\mathsf{H}}\widetilde{\mathbf{K}}_{m,\Gamma}^{l-1}\mathbf{P}_{\Gamma}\mathbf{M}_{\mathrm{m}}^{-1}\mathbf{P}_{\Gamma}^{\mathsf{H}}\left(\widetilde{\mathbf{K}}_{m,\Gamma}^{l-1}\right)^{\mathsf{H}}\vec{\mathbf{w}}.$$
$$(4.14)$$

We can now compare the left-hand side of (4.14) with the generic discrete
system (4.13), write

$$\mathbf{M}_{\beta,\Gamma}^{l-1} \equiv \widetilde{\mathbf{K}}_{m,\Gamma}^{l-1}\mathbf{P}_{\Gamma}\mathbf{M}_{\mathrm{m}}^{-1}\mathbf{P}_{\Gamma}^{\mathsf{H}}\left(\widetilde{\mathbf{K}}_{m,\Gamma}^{l-1}\right)^{\mathsf{H}}, \tag{4.15}$$

and associate the boundary-energy term of (4.14) with the energy in Ω_{m}: both
matrices are discrete Hodge operators, like mass matrices $\mathbf{M}_{\alpha}^{l}, \mathbf{M}_{\gamma}^{l-1}$. More
details on this association are given in the next paragraph.

Remark 4.3.1. *The system* (4.10) *can also be derived by finding a stationary
point of the functional (compare with* (3.52) *and* (3.60))

$$\mathrm{L}(u,v) := \frac{1}{2}\int_{\Omega}\left(\star_{\alpha}\mathrm{d}u \wedge \mathrm{d}u + \star_{\gamma}u \wedge u\right) + \frac{1}{2}\int_{\Omega_{\mathrm{m}}}\star_{\alpha}\mathrm{d}\left(v+w\right) \wedge \mathrm{d}\left(v+w\right) +$$
$$(-1)^{l-1}\int_{\Gamma}\mathbf{t}\left[\star_{\alpha}\mathrm{d}\left(v+w\right)\right] \wedge \mathbf{t}\,u\,,$$
$$(4.16)$$

with $u \in \Lambda^{l-1}(\Omega)$ *and* $v, w \in \mathcal{T}(\Omega_{\mathrm{m}})$, *where* w *is the known excitation* $(l-1)$-
form.

The first integral in (4.16) *expresses the energy of* (4.5) *in* Ω, *the second the
energy in* Ω_{m} *(given* $\gamma = 0$ *in* Ω_{m}). *From the conditions for a stationary point*

of L, *we obtain the coupled problem in variational form*

Seek $u \in \Lambda^{l-1}(\Omega), \; v \in \mathcal{T}(\Omega_{\mathrm{m}})$:

$$
\begin{cases}
\displaystyle\int_{\Omega} (\star_\alpha \mathrm{d}u \wedge \mathrm{d}\eta + \star_\gamma u \wedge \eta) + (-1)^{l-1} \int_{\Gamma} \mathbf{t}\,(\star_\alpha \mathrm{d}v) \wedge \mathbf{t}\,\eta = (-1)^l \int_{\Gamma} \mathbf{t}\,(\star_\alpha \mathrm{d}w) \wedge \mathbf{t}\,\eta \\[2mm]
(-1)^{l-1} \displaystyle\int_{\Gamma} \mathbf{t}\,(\star_\alpha \mathrm{d}\zeta) \wedge \mathbf{t}\,u + \int_{\Omega_{\mathrm{m}}} \star_\alpha \mathrm{d}\zeta \wedge \mathrm{d}v \quad = \int_{\Omega_{\mathrm{m}}} \star_\alpha \mathrm{d}\zeta \wedge \mathrm{d}w
\end{cases}
$$

$$\forall \eta \in \Lambda^{l-1}(\Omega), \; \forall \zeta \in \mathcal{T}(\Omega_{\mathrm{m}}).$$

$$(4.17)$$

The same expression as (4.10) *is obtained by noticing that*

$$
\int_{\Omega_{\mathrm{m}}} \star_\alpha \mathrm{d}\zeta \wedge \mathrm{d}v = -(-1)^{l-1} \int_{\Gamma} \mathbf{t}\,(\star_\alpha \mathrm{d}\zeta) \wedge \mathbf{t}\,v , \tag{4.18a}
$$

$$
\int_{\Omega_{\mathrm{m}}} \star_\alpha \mathrm{d}\zeta \wedge \mathrm{d}w = -(-1)^{l-1} \int_{\Gamma} \mathbf{t}\,(\star_\alpha \mathrm{d}\zeta) \wedge \mathbf{t}\,w , \tag{4.18b}
$$

which hold by integration by parts because of $v, w \in \mathcal{T}(\Omega_{\mathrm{m}})$. (4.18a) *shows that* $\mathbf{M}_{\mathrm{m}}$, *which is its discrete representation, is a Hermitian positive-definite matrix and therefore invertible, which ensures that the Schur complement system* (4.14) *exists.*

4.4 Coupling through an $(m-1)$-Form

We conclude by exploiting $\mathrm{d}\mathbf{j} = 0$ in Ω_{m} to switch to a potential representation; Ω_{m} is supposed to have trivial topology, i.e. m-th Betti number $\beta_m(\Omega_{\mathrm{m}}) = 0$ [53, p. 246, Theorem 2.1], given $m := n - l$. From (4.17) we derive a hybrid system for $u \in \Lambda^{l-1}(\Omega)$ and $\mathbf{j} \in \Lambda^m(\Omega_{\mathrm{m}})$ (with an abuse of notation) and introduce a potential form $\pi \in \Lambda^{m-1}(\Omega_{\mathrm{m}})$, which replaces the unknown $v \in \mathcal{T}(\Omega_{\mathrm{m}}) \in \Lambda^{l-1}(\Omega_{\mathrm{m}})$ in the exterior problem.[4]

---

[4]In the case of $n = 3$, the unknown $v \in \Lambda^1(\Omega_{\mathrm{m}})$ is replaced by $\pi \in \Lambda^0(\Omega_{\mathrm{m}})$, i.e. a vector function is replaced by (the gradient of) a scalar function (magnetic scalar potential, see Remark 1.2.1). The problem becomes equivalent to Section 1.1.4.

Based on (4.1a) and (4.1b), we can write that $\star_\alpha \mathrm{d}v = (-1)^l \mathbf{j}$ in Ω_{m}. (4.17) can therefore be rewritten as

Seek $u \in \Lambda^{l-1}(\Omega)$, $\mathbf{j} \in \mathcal{T}(\Omega_{\mathrm{m}})$:

$$\begin{cases} \int\limits_{\Omega} (\star_\alpha \mathrm{d}u \wedge \mathrm{d}\eta + \star_\gamma u \wedge \eta) - \int\limits_{\Gamma} \mathbf{t}\,\mathbf{j} \wedge \mathbf{t}\,\eta \;=(-1)^l \int\limits_{\Gamma} \mathbf{t}\,(\star_\alpha \mathrm{d}w) \wedge \mathbf{t}\,\eta \\[2mm] \qquad\qquad -\int\limits_{\Gamma} \mathbf{t}\,\boldsymbol{\iota} \wedge \mathbf{t}\,u + \int\limits_{\Omega_{\mathrm{m}}} \boldsymbol{\iota} \wedge \star_{\alpha^{-1}}\mathbf{j} = (-1)^l \int\limits_{\Omega_{\mathrm{m}}} \boldsymbol{\iota} \wedge \mathrm{d}w \end{cases} \tag{4.19}$$
$$\forall \eta \in \Lambda^{l-1}(\Omega),\ \forall \boldsymbol{\iota} \in \mathcal{T}(\Omega_{\mathrm{m}}),$$

where $\mathbf{j}, \boldsymbol{\iota}$ belong to the same Trefftz space (4.8), after applying the transformation $v \to (-1)^l \star_\alpha \mathrm{d}v$ for functions $v \in \mathcal{T}(\Omega_{\mathrm{m}})$.

Let us now take $\pi, \tau \in \Lambda^{m-1}(\Omega_{\mathrm{m}})$ such that, in Ω_{m}, $\mathbf{j} = \star_\alpha \mathrm{d}\pi$ and $\boldsymbol{\iota} = \star_\alpha \mathrm{d}\tau$. This means that the new Trefftz space of functions that solve the exterior problem exactly is

$$\mathcal{T}(\Omega_{\mathrm{m}}) := \Big\{ v \in \Lambda^{m-1}(\Omega_{\mathrm{m}}) \colon\ \mathrm{d}\left(\star_\alpha \mathrm{d}v\right) = 0\,,\ \ \alpha \in \mathbb{C},$$
$$v \text{ satisfies the condition at infinity } (4.2) \Big\}, \tag{4.20}$$

where $(m-1)$-forms are used instead of $(l-1)$-forms as in (4.8).

System (4.19) finally becomes

Seek $u \in \Lambda^{l-1}(\Omega)$, $\pi \in \mathcal{T}(\Omega_{\mathrm{m}})$:

$$\begin{cases} \int\limits_{\Omega} (\star_\alpha \mathrm{d}u \wedge \mathrm{d}\eta + \star_\gamma u \wedge \eta) - \int\limits_{\Gamma} \mathbf{t}\,(\star_\alpha \mathrm{d}\pi) \wedge \mathbf{t}\,\eta = (-1)^l \int\limits_{\Gamma} \mathbf{t}\,(\star_\alpha \mathrm{d}w) \wedge \mathbf{t}\,\eta \\[2mm] \qquad -\int\limits_{\Gamma} \mathbf{t}\,(\star_\alpha \mathrm{d}\tau) \wedge \mathbf{t}\,u + \int\limits_{\Omega_{\mathrm{m}}} \star_\alpha \mathrm{d}\tau \wedge \mathrm{d}\pi \;=(-1)^l \int\limits_{\Omega_{\mathrm{m}}} \star_\alpha \mathrm{d}\tau \wedge \mathrm{d}w \end{cases}$$
$$\forall \eta \in \Lambda^{l-1}(\Omega),\ \forall \tau \in \mathcal{T}(\Omega_{\mathrm{m}}),$$
$$\tag{4.21}$$

where we can replace the integrals in Ω_{m} with integrals on Γ, similarly to (4.18).

5 Implementation

The code implementing the FEM–MMP coupling for the numerical experiments of this work is written in `C++`. `CMake` v3.14.5 [1] takes care of the build process, including the dependencies of the code. We use `Boost` v1.71.0 [34] for its `program_options` and `unit_test_framework` libraries, `Eigen` v3.3.7 [44] for linear algebra, and `HyDi` [24] for the FEM component.

`HyDi`, which can handle `Hybrid` nonconforming meshes and `Discontinuous` finite elements, is a template-based `C++14` library, parallelized with `C++11` multithreading, that is used as in-house simulation software at the multinational ABB. It was written during the PhD project of R. Casagrande at ETH Zurich [23, p. 147, Chapter 6] in collaboration with Ch. Winkelmann (ABB Corporate Research Center): we gratefully acknowledge their contribution.

On top of `HyDi`, we introduce new libraries (for a comprehensive list, see Section 5.1), generally independent of other `HyDi` libraries. They take care of computing

- local matrices on the mesh entities that, when assembled together, form a block of the coupling system, and

- multipoles (Section 2.2).

Blocks of the coupling systems can be purely FEM, mixed FEM–MMP, or purely MMP. They are assembled following the *strategy pattern* [38, p. 349]: an object with a method that returns the local matrix of the block is passed to a *context class* that assembles the block by calling such method for each entity of the mesh. The loop of the *assembly process* [58, p. 37] is then parallelized using threads of the `C++` *Standard Template Library* [81]. *Mutex* must be enforced on the entries of the blocks to prevent *race conditions* when summing contributions from neighboring mesh entities [7, p. 59, Chapter 4].

Multipoles are child classes of a common virtual interface templated with respect to the type of the returned evaluations. This type is specialized as

`double` or `std::complex<double>` depending on whether the multipole has Hankel functions of the first kind [64, p. 280] as radial dependence. Objects of class multipole with different centers or orders are then stored in a *container class* [38, p. 183] forming the expansion.

The implementation of multipoles depends on four libraries for

1. (vector) spherical harmonics [64, p. 250],

2. Bessel and Hankel functions of the first kind [64, p. 278, (9.7)] taking a complex argument,

3. the exact multipole expansion of *Mie theory* (see Section 6.6.1), and

4. *layered dipoles* (see Section 6.6.2).

For the spherical harmonics, we rely on [62]: these functions are hardcoded for efficiency up to order $\ell = 4$ and, for higher orders, computed through the associated Legendre polynomials [64, p. 255], for which a recurrence relation holds [64, p. 269, Exercise 8.8]. The *automatic differentiation* module of `Eigen` [44] applied to [62] returns the derivatives needed by the *vector* spherical harmonics.[1]

Bessel functions of complex arguments are implemented by [35], while Mie theory by [70]. The former are needed in case we work with complex wavenumbers [43, p. 422, (9.165)].

We acknowledge U. Koch, researcher at the Institute of Electromagnetic Fields of ETH Zurich (D-ITET), for his `C++` implementation of layered dipoles [60, p. 128, Section 6.3.2]. This kind of multipoles includes *Sommerfeld integrals*, which present singularities that require integration over complex contours [31, p. 111, Section 2.7].

In addition to the assembly process that builds the linear system for the coupling, solving such systems constitutes the other bottleneck of a coupled FEM–MMP implementation. However, these systems, formed by large, sparse blocks (pure FEM) and small, dense ones (pure MMP) present nontrivial sparsity patterns (see Figure 5.1) that do not lead to obvious preconditioners for iterative

---

[1]The Auto Diff module of `Eigen` cannot be applied to the spherical harmonics provided by `Boost` [34].
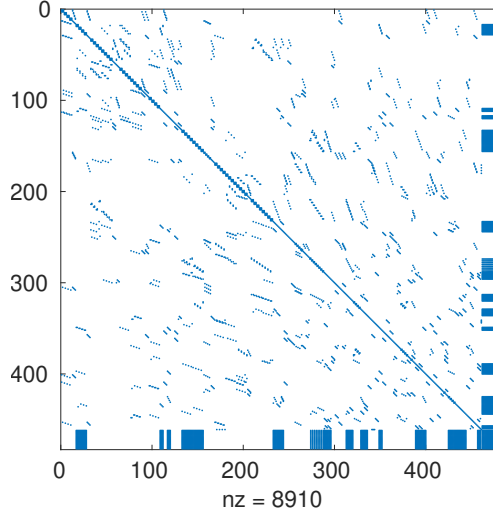
Figure 5.1: Sample matrix of the DtN-based coupling for a 2D scattering experiment. The top-left large, sparse block is for pure FEM, the bottom-right small, dense one for pure MMP. The off-diagonal, symmetric blocks have nonzero rows/columns for FEM degrees of freedom that are associated to intersections of $\mathcal{M}_f$ with Γ.

solvers [58, p. 605, Section 13.2]. *LU decomposition* [58, p. 587, Section 13.1.1] is therefore the algorithm of choice.[2]

To this aim, we use the `PARDISO` v6.0 library [76] that is parallelized on *symmetric multiprocessor systems* (i.e. with a shared memory). A modified `Eigen` wrapper converts the matrices stored with `Eigen` data structures to a format compatible with `PARDISO`.

5.1 Libraries

The new libraries that implement the FEM–MMP coupling are:

- `coupling`, a header-only library containing `BlockInstruct` template classes: each encodes the instructions to build a block of the left-hand

---

[2]Iterative solvers are only used in our work [26]: more details in Chapter 4.

side of the linear system for a coupling strategy (Chapter 3). They inherit from one among `BlockInstruct_A_FEM_MMP`, `BlockInstruct_A_MMP_FEM`, or `BlockInstruct_A_MMP`, depending on whether they have FEM test functions and MMP trial functions, the other way around, or express pure MMP blocks (pure FEM blocks are implemented by `HyDi` – see *integrators* below). `BlockInstruct_A` is the base class of these three types.[3] The DG-based coupling, being arguably the most difficult strategy to implement out of Chapter 3, has the largest number of `BlockInstruct` classes, also to consider the differences between its scalar (Section 1.1.1) and vector implementations (Section 1.1.3).

- `matching` is a sublibrary of `coupling`, also header-only, with the instructions to assemble (rectangular) blocks for the collocation method: test functions are Dirac delta functions [43, p. 45, Section 1.5] centered in selected matching points. These points are generally many more than the number of degrees of freedom of the trial space.

- `expansion` stores template classes derived from base `Multipole` in header files and the specializations of their methods, depending on whether they return `double` or `std::complex<double>`, in corresponding source files. The template class `Expansion` constitutes the container of objects of derived types from `Multipole`.

- `spherharm` is a sublibrary of `expansion` implementing real and complex spherical harmonics and corresponding vector spherical harmonics, which are based on the derivatives of the former.

- `extra` contains all the routines that do not belong to any of the above libraries. Specifically,

  - some code to find equispaced points on the surface of a rectangular prism, which are potential centers of multipole expansions in $\mathbb{R}^3$,

  - utilities to concatenate `Eigen` sparse matrices or eliminate their empty rows/columns, and

  - a `struct` organizing the electromagnetic parameters of a numerical example (Section 5.2).

---

[3]On the other hand, `BlockInstruct_b` is the base class for the instructions to assemble subvectors forming the right-hand side of the coupling system.

Moreover, there are two sets of new classes that enrich existing `HyDi` libraries; namely,

1. *integrators*, which contains instructions for pure FEM blocks that were not expected by `HyDi`: for example, the boundary integral $\int_\Gamma [\mathbf{n} \times (\mathbf{n} \times \mathbf{u}_\mathrm{f})] \cdot \boldsymbol{\lambda} \, \mathrm{d}S$ of (3.47) for the multi-field coupling; and

2. new classes derived from `hydi::fem::IGridFunction`: for example, to evaluate a linear combination of multipoles on a mesh for visualization purposes.

A *unit test framework* [23, p. 150, Section 6.2] checks that the new libraries, especially the vector spherical harmonics, return the expected results.

5.2 Executables

Here we provide the `CMake` targets to compile the executables for the numerical experiments in the next Chapter 6:

- `CT_Magnetostatics_2D` for Section 6.1.1, with codes in folder `ConvergenceTests/Magnetostatics_2D`;

- `CT_Magnetostatics_2D_Alt` for Section 6.1.2, with codes in folder `ConvergenceTests/Magnetostatics_2D_Alt`;

- `CT_Electrostatics` for Section 6.2, with codes in folder `ConvergenceTests/Electrostatics`;

- `CT_Scattering_2D` for Section 6.3.1 (one MMP domain), with codes in folder `ConvergenceTests/Scattering_2D`;

- `2D_Scattering` for Section 6.3.2 (more than one MMP domain), with codes in folder `2D_Scattering`;

- `CT_Magnetostatics` for Section 6.4.1, with codes in folder `ConvergenceTests/Magnetostatics`;

- `3D_Inductor` for Section 6.4.2, with codes in folder `3D_Inductor`;

- `Eddy` for Section 6.5, with codes in folder `Eddy`;

- `CT_Scattering` for Section 6.6.1 (one MMP domain), with codes in folder `ConvergenceTests/Scattering`;

- `3D_Scattering` for Section 6.6.2 (more than one MMP domain), with codes in folder `3D_Scattering`; and

- `NanoParticle` for Section 6.6.2 (*layered dipoles*), with codes in folder `NanoParticle`.

Meshes are stored in a subfolder called `mesh`; when a target is executed, symbolic links to the required meshes are automatically created by `CMake` in the target folder of the build directory. A text file called `config.ini` is also linked in the target folder and can be edited to specify configuration options with the format `name_of_option = value`, given the `Boost/program_options` library [34].

For each coupling strategy, you need to append a suffix to the above targets; namely,

1. `_LS` for the PDE-constrained least-squares coupling (Section 3.1),

2. `_DG` for the DG-based coupling (Section 3.2),

3. `_mortar` for the multi-field coupling (Section 3.3), and

4. `_DtN` for the DtN-based coupling (Section 3.4).

6 Numerical Experiments

Throughout we use piecewise-linear Lagrangian finite elements for scalar variables, i.e. $V^n(\mathcal{M}_\mathrm{f}) = \mathcal{S}_1^0(\mathcal{M}_\mathrm{f})$ from (1.14a), and lowest-order $\mathbf{H}(\mathbf{curl}, \Omega_\mathrm{f})$-conforming edge elements of the first family due to Nédélec for vector variables, i.e. $\mathbf{V}^n(\mathcal{M}_\mathrm{f}) = \mathcal{R}^1(\mathcal{M}_\mathrm{f})$ from (1.14b). Meshes $\mathcal{M}_\mathrm{f}$ of Ω_f are composed of

- triangles [18, p. 61, Defintion 5.1] in 2D, and generated using `Gmsh` v4.4.1 [40], or

- tetrahedra [67, p. 112, Section 5.3] in 3D, and generated using `COMSOL` v5.3a [33].

To study the convergence we employ uniform h-refinement of $\mathcal{M}_\mathrm{f}$ and p-refinement of the Trefftz (MMP) approximations, in the sense that we increase the number of multipoles. The p-refinement of the multipoles forming $\mathcal{T}^n(\Omega_\mathrm{m}^i)$, $i = 0, 1$, is linked to the h-refinement of $\mathcal{M}_\mathrm{f}$; specifically, to the logarithm of the number of intersections of the mesh entities of $\mathcal{M}_\mathrm{f}$ on $\Gamma_{\mathrm{f}i}$. This choice is motivated by the exponential convergence of the MMP approximation error (see Sections 2.3 and 2.4).

We monitor the following errors:

- The volume errors in the bounded domains $\Omega_\mathrm{f}, \Omega_\mathrm{m}^1$. These are the relative $\mathbf{L}^2(\Omega_\mathrm{f})$- and $\mathbf{L}^2(\Omega_\mathrm{m}^1)$-errors (or L^2, if scalar) of the FEM and MMP (in Ω_m^1) approximations compared to the reference solution $\mathbf{u}$, i.e.

$$\left\| \mathbf{u} - \sum_{j=1}^{N_\mathrm{f}} \alpha_\mathrm{f}^j \, \mathbf{v}_\mathrm{f}^j(\mathbf{x}) \right\|_{\mathbf{L}^2(\Omega_\mathrm{f})} \Bigg/ \|\mathbf{u}\|_{\mathbf{L}^2(\Omega_\mathrm{f})} \text{ and}$$

$$\left\| \mathbf{u} - \sum_{j=1}^{N_\mathrm{m}^1} \alpha_\mathrm{m}^{j,1} \, \mathbf{v}_\mathrm{m}^{j,1}(\mathbf{x}) \right\|_{\mathbf{L}^2(\Omega_\mathrm{m}^1)}^2 \Bigg/ \|\mathbf{u}\|_{\mathbf{L}^2(\Omega_\mathrm{m}^1)}, \tag{6.1}$$

with $\alpha_f^j, \alpha_m^{j,1} \in \mathbb{C}$, $\mathbf{v}_f^j \in \mathbf{V}^n(\mathcal{M}_f)$, $\mathbf{v}_m^{j,1} \in \boldsymbol{\mathcal{T}}^n(\Omega_m^1)$, and N_f, N_m^1 numbers of degrees of freedom of the discrete spaces $\mathbf{V}^n(\mathcal{M}_f)$ and $\boldsymbol{\mathcal{T}}^n(\Omega_m^1)$, respectively.

Remark 6.0.1. *On the bounded MMP domain Ω_m^1 we define an auxiliary volume mesh for the numerical quadrature of the error (6.1). However, on top of $\mathcal{M}_f$, only a mesh on the hypersurface Γ_{01} is really necessary for the coupling, in order to compute the numerical integrals on that interface. Specifically, throughout we mesh Γ_{01} (and any curved surface) by simple polygonal/polyhedral approximations. Of course, if only one (unbounded) MMP domain Ω_m is considered, then only the mesh $\mathcal{M}_f$ is needed (and no other volume error than $\mathbf{L}^2(\Omega_f)$ is computed).*

- The boundary error on $\partial\Omega_m^0 = \Gamma_{f0} \cup \Gamma_{01}$, union of the interfaces between the unbounded domain Ω_m^0 and the other (bounded) domains Ω_f, Ω_m^1. This is the relative $\mathbf{L}^2(\partial\Omega_m^0)$-error of the MMP solution in Ω_m^0 compared to the reference solution.

We can ignore the impact of numerical integration for FEM because we use a local Gaussian quadrature rule that is exact for polynomials of degree 2 (order 3).

In the following, when lengths are reported, the implicit measurement unit is meter[1] for consistency with the electromagnetic parameters $\mathbf{M}_\mu, \mathbf{M}_\epsilon, \omega, \mathbf{j}$.

6.1 2D Diffusion

6.1.1 2D Diffusion with Exact Solution

We solve $-\nabla^2 u = j$ in $\mathbb{R}^2$, with piecewise constant source j, $|j| = 1.05 \cdot 10^6$ in $\Omega_\star$ and $= 0$ elsewhere. $\Omega_\star$ is formed by two disks, with j having a different sign in each of them. The geometry is shown in Figure 6.1; the coupling boundary Γ is artificial.

The exact solution is given by the fundamental solution of 2D Poisson's equation integrated with Gaussian quadrature of degree 2 (order 3). Multipole

---

[1]Except for the 2D diffusion case (Section 6.1), which is dimensionless.
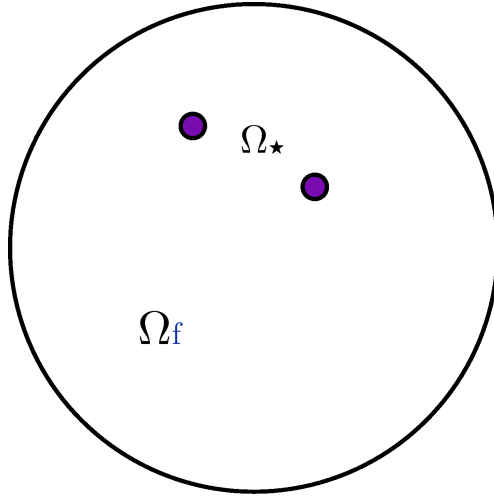
Figure 6.1: Geometry of Ω_{f}. The violet disks of radius 0.1 are $\Omega_{\star}$, the area where $j \neq 0$: in one it is $= 1.05 \cdot 10^6$, in the other $= -1.05 \cdot 10^6$. They are centered at $(0.5, 0.5)^{\top}$ and $(-0.5, 1)^{\top}$. The black circle centered in the origin with radius 2 is the artificial coupling boundary Γ.
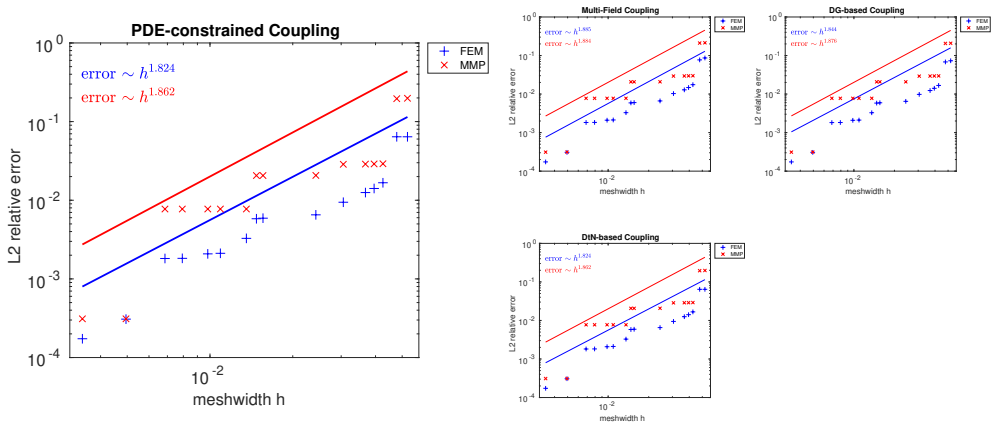
Figure 6.2: h-refinement log-log error plots for 2D diffusion with exact solution.

expansions are uniformly positioned on a circle of radius 1 centered in the origin. We only use multipole expansions of order 1.

Numerical Results

Figure 6.2 shows h-refinement convergence plots for all coupling approaches, which lead to very similar plots. We can clearly identify a quadratic convergence of the FEM and MMP errors in terms of the meshwidth.

Figure 6.3 shows surface plots of the total relative L^2-error for all coupling approaches. The error decreases with h (algebraic convergence) and is generally independent of the number of multipoles. This is due to the fact that the exact solution is so easy to approximate in the MMP domain that it can already be represented by very few multipoles. However, the error also becomes worse with the coarsest meshes and the highest number of multipoles considered: the FEM error dominates.
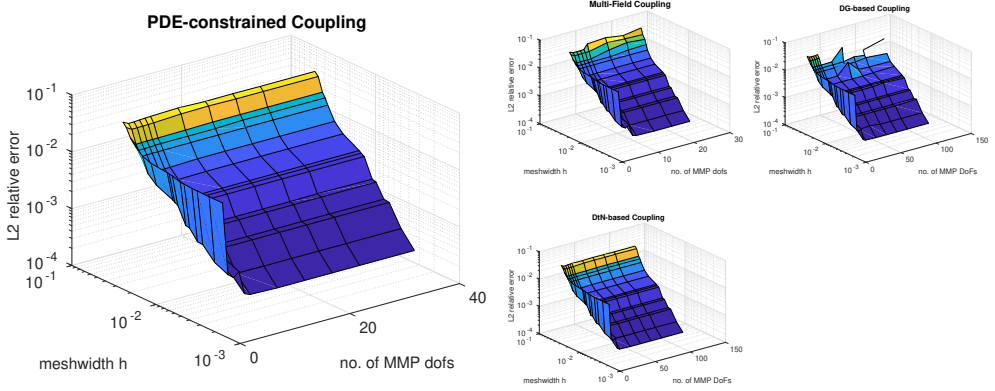
Figure 6.3: Meshwidth h vs. MMP degrees of freedom for 2D diffusion with exact solution: total relative error.

6.1.2 2D Diffusion with Jumping Coefficients

We solve $-\nabla \cdot (\kappa \nabla u) = j$ in $\mathbb{R}^2$, with $\kappa = \frac{1}{10}$, $j = 1.05 \cdot 10^6$ in $\Omega_\star$ and $\kappa = 1$, $j = 0$ elsewhere. $\Omega_\star$ is the U-shaped region displayed in Figure 6.4. For want of an exact solution, as reference we rely on the numerical solution provided by a mesh substantially more refined than the finest mesh used in the convergence study. However, local mesh refinement at the corners of the U-shaped region inside Ω_f is needed because the solution is not smooth there: the meshwidth goes like $h_0 + r^3$, with h_0 minimum meshwidth and r distance from the closest corner.

All types of meshes employed are shown in Figure 6.4: we consider three examples where the boundary Γ has different positions and shapes.

With Γ at the discontinuities of κ and j, multipoles are uniformly positioned along the skeleton inside Ω_f (see Figure 6.4a). With Γ at a positive distance from $\Omega_\star$, that is, in the case of an artificial coupling boundary, multipoles are uniformly positioned along a line following the skeleton of $\Omega_f \setminus \Omega_\star$, which is positioned at a distance of 0.15 from $\partial\Omega_\star$ (see Figures 6.4b and 6.4c). We only use multipoles of order 0 (fundamental solutions of $-\nabla^2 u = 0$).

Given the different boundaries Γ, for a fair comparison the MMP error has not been computed as a boundary error, but on coarser meshes encompassing

(a) Geometry of $\Omega_f = \Omega_\star$. Γ coincides with the discontinuities of κ and j.

(b) Geometry of $\Omega_f \supset \Omega_\star$ that has different κ and j. Γ lies at a positive distance from $\Omega_\star$ and is polygonal.

(c) Geometry of $\Omega_f \supset \Omega_\star$ that has different κ and j. Γ lies at a positive distance from $\Omega_\star$ and is C^1.
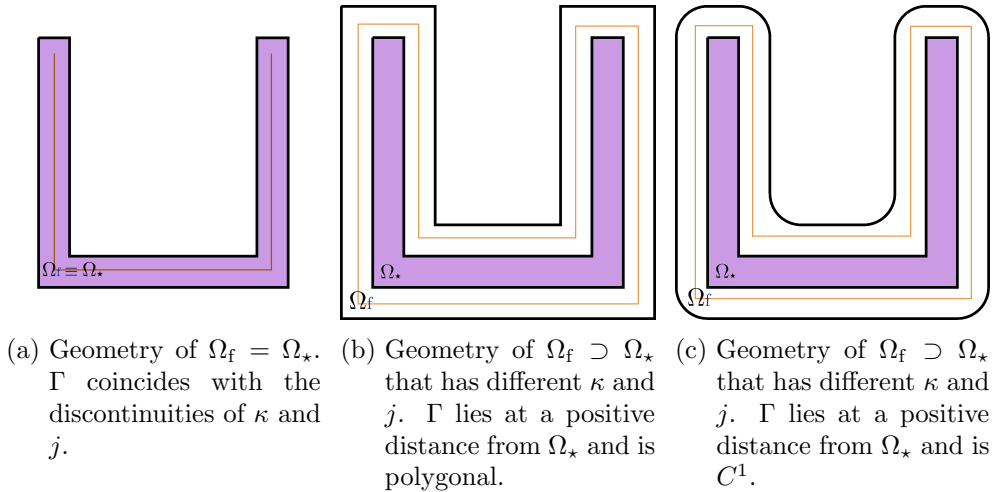
Figure 6.4: The violet U-shape, which fits into $[-1,1]^2$, is $\Omega_\star$ with $\kappa = \frac{1}{10}$ and $j = 1.05 \cdot 10^6$. The other part of the geometry is characterized by $\kappa = 1$ and $j = 0$. The brown line is the curve along which multipoles are positioned uniformly.

the area around Ω_f bounded by $[-4,4]^2$.

Numerical Results

Figure 6.5 shows DoF-refinement convergence plots for all coupling approaches, given Γ at the discontinuities. We can identify algebraic convergence of the FEM and MMP errors, but with quite different rates depending on the coupling approach.

Figures 6.6 and 6.7 show DoF-refinement convergence plots for all coupling approaches, given Γ at a positive distance from $\Omega_\star$, either with or without corners. We can clearly identify algebraic convergence of the FEM and MMP errors.
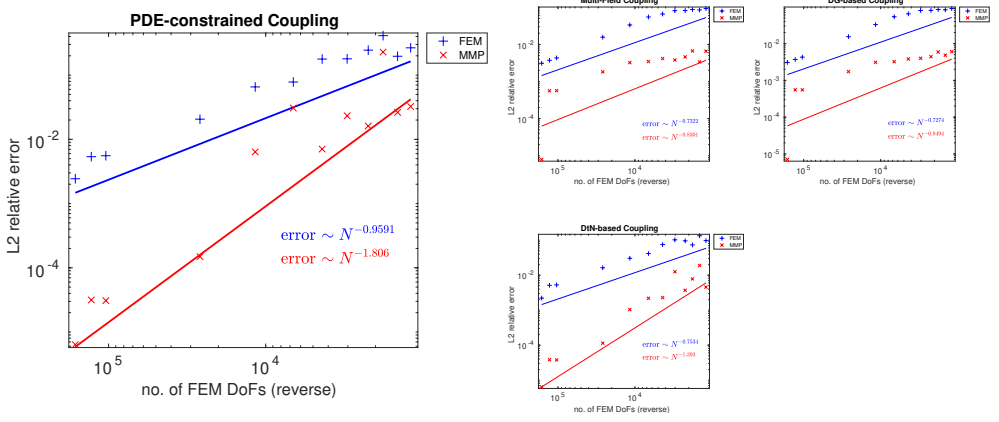
Figure 6.5: DoF-refinement log-log error plots for 2D diffusion with jumping coefficients. Γ coincides with the discontinuities of κ and j (see Figure 6.4a).
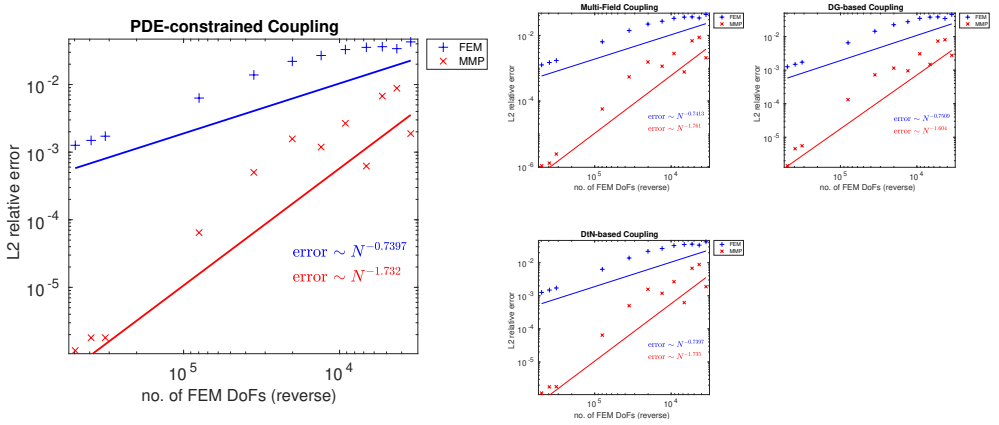
Figure 6.6: h-refinement log-log error plots for 2D diffusion with jumping coefficients. Γ lies at a positive distance from $\Omega_\star$ and is polygonal (see Figure 6.4b).
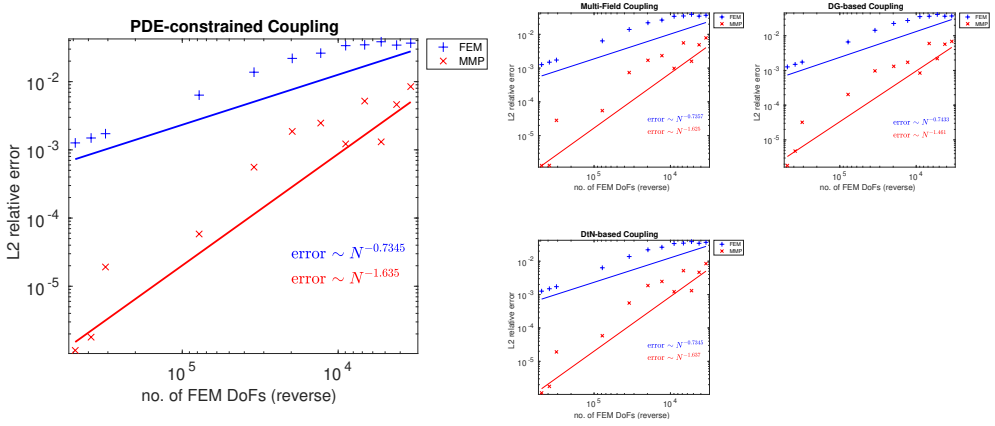
Figure 6.7: DoF-refinement log-log error plots for 2D diffusion with jumping coefficients. Γ lies at a positive distance from $\Omega_\star$ and is C^1 (see Figure 6.4c).

6.2 Electrostatics

We solve $-\nabla^2 u = j$ in $\mathbb{R}^2$, with $j = \frac{3}{4\pi}\,\mathrm{C\,m^{-3}}$ in $\Omega_\star$ and $= 0$ elsewhere. $\Omega_\star$ is formed by a sphere of radius 1 centered at $(0, 0, 0.5)^\top$. The geometry is shown in Figure 6.8; the coupling boundary Γ is artificial.

The exact solution is given by an exact integration inside $\Omega_\star$ and the fundamental solution of 3D Poisson's equation (integrated with Gaussian quadrature of order 3) outside. Multipole expansions are uniformly positioned on a circle of radius 1 centered in the origin and lying on the XY-plane. We only use multipole expansions of order 1.

Numerical Results

Figure 6.9 shows h-refinement convergence plots for all coupling approaches, which lead to very similar plots. We can identify algebraic convergence of the FEM and MMP errors.
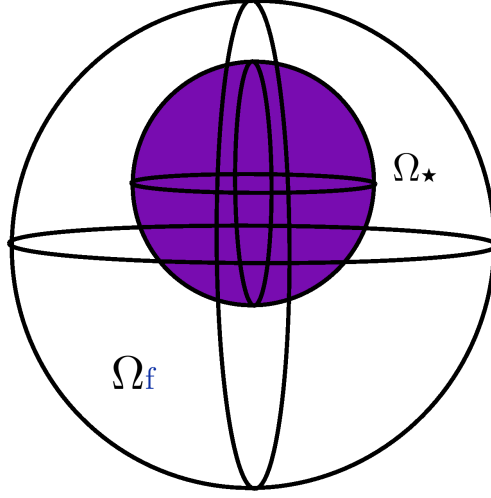
Figure 6.8: Cross-section of 3D geometry of Ω_{f} along the XZ-plane. The violet sphere of radius 1 is $\Omega_\star$, the volume where $q \neq 0$. It is centered at $(0,0,0.5)^\top$. The large sphere centered in the origin with radius 2 is the artificial coupling boundary Γ.
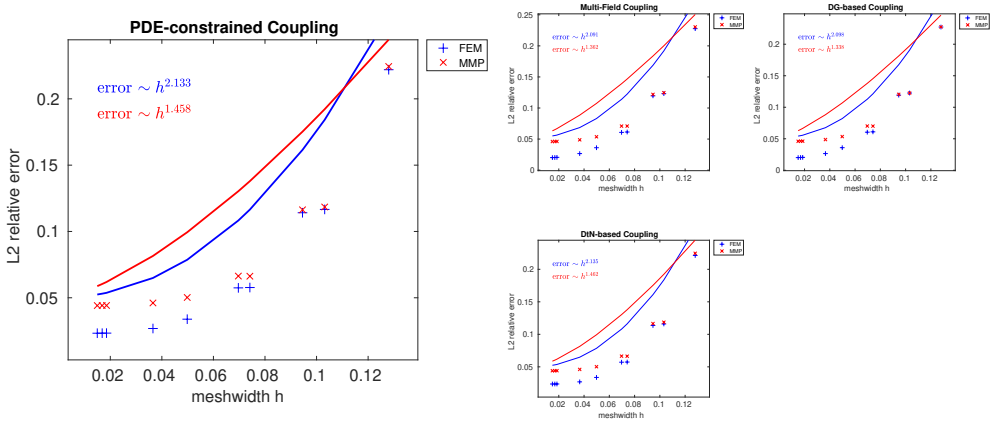
Figure 6.9: h-refinement log-log error plots for electrostatics.
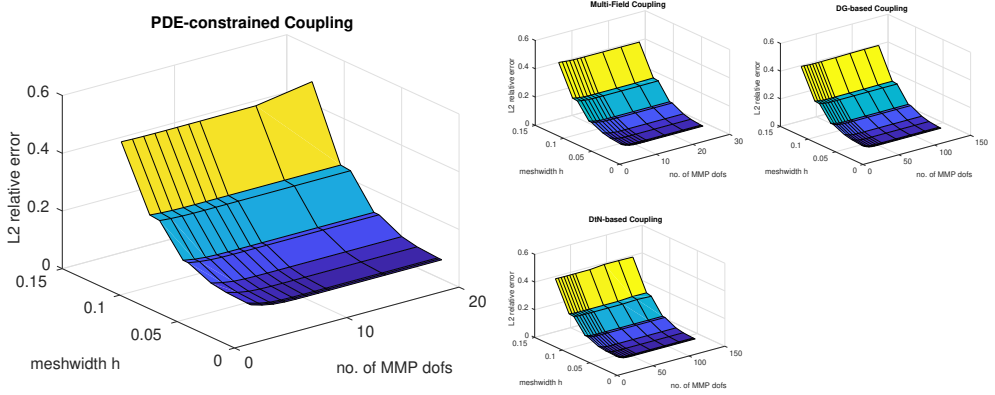
Figure 6.10: Meshwidth h vs. MMP degrees of freedom for electrostatics: total relative error.

Figure 6.10 shows surface plots of the total relative L^2-error for all coupling approaches. The error decreases with h (algebraic convergence) and is generally independent of the number of multipoles.

6.3 2D Scattering

6.3.1 2D Scattering with Exact Solution

We solve $\nabla \cdot \left(\mu^{-1} \nabla u \right) + \omega^2 \epsilon\, u = 0$ in $\mathbb{R}^2$ subject to the Sommerfeld radiation condition (1.2b) with piecewise-constant permeability $\mu = 100\,\mu_0$ in a unit disk centered in the origin, which we dub $\Omega_\bullet$, and $\mu = \mu_0 = 4\pi \cdot 10^{-7}\,\mathrm{H\,s^{-1}}$ (permeability of free space) elsewhere. ϵ and ω are everywhere equal to $\epsilon_0 = 8.85 \cdot 10^{-12}\,\mathrm{F\,m^{-1}}$ (permittivity of free space) and $23.56 \cdot 10^7\,\mathrm{rad\,s^{-1}}$, respectively. Wavenumbers are therefore $k_\bullet = 10\,k_0$ in $\Omega_\bullet$ and $k_0 = 0.79\,\mathrm{rad\,m^{-1}}$ elsewhere.

We assume that u is subject to an excitation by an incident plane wave propagating along the x-axis outside $\Omega_\bullet$, i.e.

$$u = u_{\mathrm{inc}} + u_{\mathrm{ref}} \text{ in } \mathbb{R}^2 \setminus \Omega_\bullet, \quad u_{\mathrm{inc}} := \exp(\imath k_0 x), \tag{6.2}$$

where u_{ref} represents the unknown reflected potential and x in u_{inc} the first Cartesian coordinate. This problem has an exact solution that can be derived using *Mie theory* [16, Chapter 4, pp. 82–101] in 2D:

$$u = u_{\text{inc}} + u_{\text{ref}} = \sum_{\ell=-\infty}^{\infty} \imath^\ell J_\ell(k_0 r) \mathrm{e}^{\imath \ell \theta} + \sum_{\ell=-\infty}^{\infty} A_\ell H_\ell^{(1)}(k_0 r) \mathrm{e}^{\imath \ell \theta} \quad \text{in } \mathbb{R}^2 \setminus \Omega_\bullet,$$

$$u = \quad u_{\text{tra}} \quad = \sum_{\ell=-\infty}^{\infty} B_\ell J_\ell(k_\bullet r) \mathrm{e}^{\imath \ell \theta} \quad \text{in } \Omega_\bullet.$$

$$(6.3)$$

Here u_{inc} is the *Jacobi–Anger expansion* of the exciting plane wave [32, p. 33, (2.46)], given J_ℓ and $H_\ell^{(1)}$ Bessel and Hankel functions of the first kind and $r \in [0, \infty)$, $\theta \in [0, 2\pi)$ canonical polar coordinate system in $\mathbb{R}^2$. u_{tra} is the unknown transmitted potential.

Coefficients A_ℓ, B_ℓ in (6.3) are

$$A_\ell = \imath^\ell \frac{\mu_\bullet^{-1} k_\bullet J_\ell(k_0 r_\bullet) J_\ell'(k_\bullet r_\bullet) - \mu_0^{-1} k_0 J_\ell(k_\bullet r_\bullet) J_\ell'(k_0 r_\bullet)}{\mu_0^{-1} k_0 H_\ell^{'(1)}(k_0 r_\bullet) J_\ell(k_\bullet r_\bullet) - \mu_\bullet^{-1} k_\bullet H_\ell^{(1)}(k_0 r_\bullet) J_\ell'(k_\bullet r_\bullet)},$$

$$B_\ell = \frac{A_\ell H_\ell^{(1)}(k_0 r_\bullet) + \imath^\ell J_\ell(k_0 r_\bullet)}{J_\ell(k_\bullet r_\bullet)}.$$

$$(6.4)$$

$r_\bullet$ is the radius of the disk $\Omega_\bullet$, here $= 1\,\mathrm{m}$.

For our numerical tests, we consider the terms in the expansions of (6.3) for $\ell = 0, \ldots, 20$, identify $\Omega_\bullet$ with Ω_{f} and $\mathbb{R}^2 \setminus \Omega_\bullet$ with a single MMP domain Ω_{m}, and therefore set $\Gamma := \partial \Omega_{\text{f}} \cap \partial \Omega_{\text{m}}$ on the physical boundary of the disk. Given that we use triangular meshes, Γ is actually a polygonal approximation of a circle.

$\mathcal{T}^n(\Omega_{\text{m}})$ is generated by a single multipole expansion centered in the origin.

Numerical Results

Figure 6.11 shows *h*-refinement convergence plots for all coupling approaches, which yield very similar results. We can clearly see algebraic convergence of the FEM and MMP errors with rate 2.
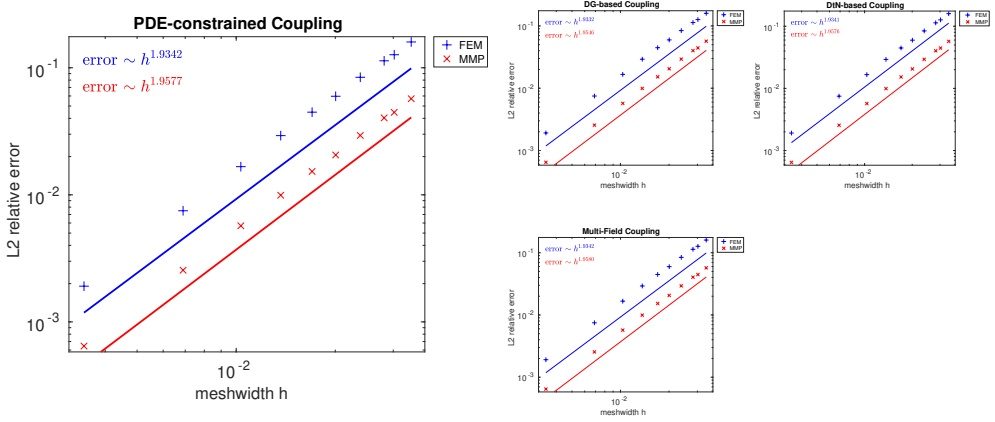
Figure 6.11: *h*-refinement log-log error plots for 2D scattering with exact solution. Parameters are $\mu_\bullet = 100\,\mu_0$ and $\omega = 23.56 \cdot 10^7\,\mathrm{rad\,s^{-1}}$.
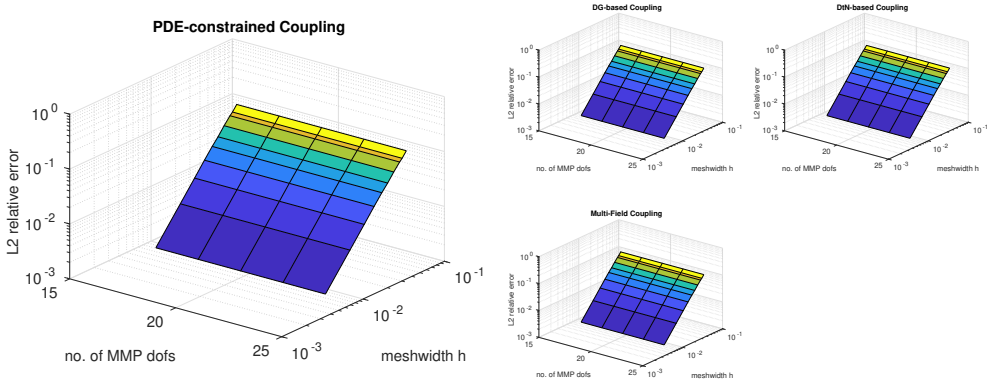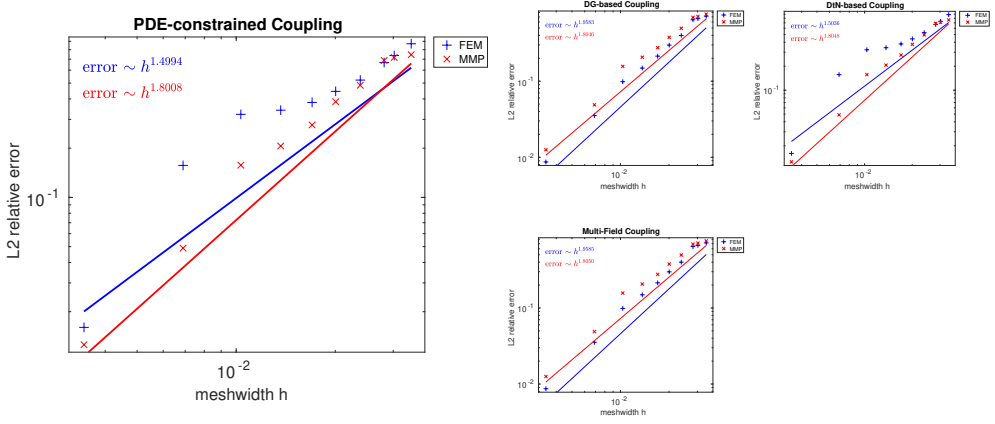

Figure 6.12: Meshwidth *h* vs. MMP degrees of freedom for 2D scattering with exact solution: total relative error. Parameters are $\mu_\bullet = 100\,\mu_0$ and $\omega = 23.56 \cdot 10^7\,\mathrm{rad\,s^{-1}}$.

Figure 6.13: h-refinement log-log error plots for 2D scattering with exact solution. Parameters are $\mu_\bullet = 100\,\mu_0$ and $\omega = 23.56 \cdot 10^8\,\mathrm{rad\,s^{-1}}$.

Figure 6.12 shows surface plots of the total relative L^2-error for all coupling approaches. The error decreases with h (algebraic convergence) and is generally independent from the number of multipoles: the FEM error dominates. This is a consequence of the exponential convergence of MMP (Section 2.3): the exact solution is so easy to approximate in the MMP domain that it can already be represented by a multipole expansion of the lowest considered order, which is 8, leading to 17 terms of the expansion – see (2.3).

We have also considered different material parameters, leading to similar convergence rates. For example, Figure 6.13 shows h-refinement convergence plots for $\mu_\bullet = 2.5281\,\mu_0$ and $\omega = 23.56 \cdot 10^8\,\mathrm{rad\,s^{-1}}$, which entails $k_\bullet = 1.59\,k_0$ and $k_0 = 7.86\,\mathrm{rad\,m^{-1}}$. Datapoints are slightly noisier than before because we consider a higher value for the frequency ω, which causes the pollution effect for FEM. However, with these parameters one can observe an interesting physical phenomenon.

Photonic Nanojet

Parameters $r_\bullet = 1\,\mathrm{m}$, $\mu_\bullet = 2.5281\,\mu_0$, $\epsilon_\bullet = \epsilon_0$, and $\omega = 23.56 \cdot 10^8\,\mathrm{rad\,s^{-1}}$ permit to observe a *photonic nanojet* [49, p. 1985, Fig. 4.a] if one considers the full plane wave as excitation. This can be seen in Figure 6.14, which
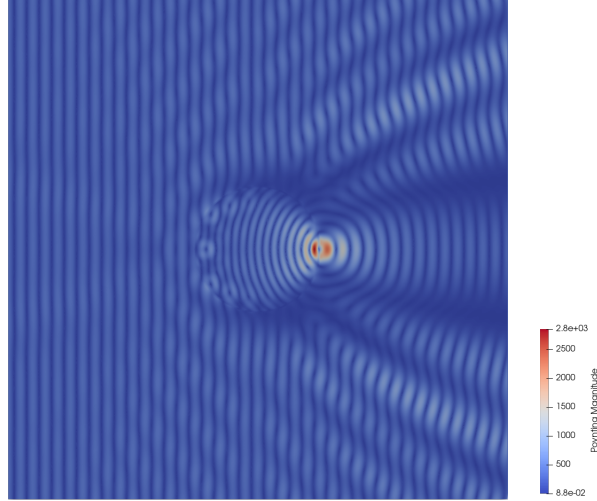
Figure 6.14: Magnitude of the Poynting vector for $\mu_\bullet = 2.5281\,\mu_0$ and $\omega = 23.56 \cdot 10^8\,\mathrm{rad\,s^{-1}}$. The beam on the circumference of the disk is the photonic nanojet. Numerical solution obtained with the DtN-based coupling.

illustrates the magnitude of the *Poynting vector* [57, p. 259, (6.109)] for a simulation with the DtN-based coupling. The other coupling schemes yield comparable results.

Two Trefftz Domains

Parameters are still $r_\bullet = 1\,\mathrm{m}$, $\mu_\bullet = 2.5281\,\mu_0$, $\epsilon_\bullet = \epsilon_0$, and $\omega = 23.56 \cdot 10^8\,\mathrm{rad\,s^{-1}}$. Similarly to the numerical example of Section 2.3.2, we split the disk $\Omega_\bullet$ into two halves, one modeled by FEM (Ω_f), the other by MMP (Ω_m^1): the coupling interface Γ_{f1} is therefore artificial. MMP also models the complement $\mathbb{R}^2 \setminus \Omega_\bullet$ (Ω_m^0): the coupling boundaries Γ_{f0} and Γ_{01}, on the two halves of the circle, correspond to the physical discontinuity of ϵ. The geometry is shown in Figure 6.15a, with a sample mesh in Figure 6.15b.

As excitation we consider terms for $\ell = 0, \ldots, 20$ from the expansion of a plane wave given by (6.3).

(a) Geometry of Ω_f, Ω_m^0, and Ω_m^1. The disk of radius 1 is $\Omega_\bullet$, the area where $\mu \neq \mu_0$.

(b) 2D mesh of Ω_f and Ω_m^1. The blue mesh covers Ω_f, the purple mesh Ω_m^1 and is used for numerical quadrature of the error.
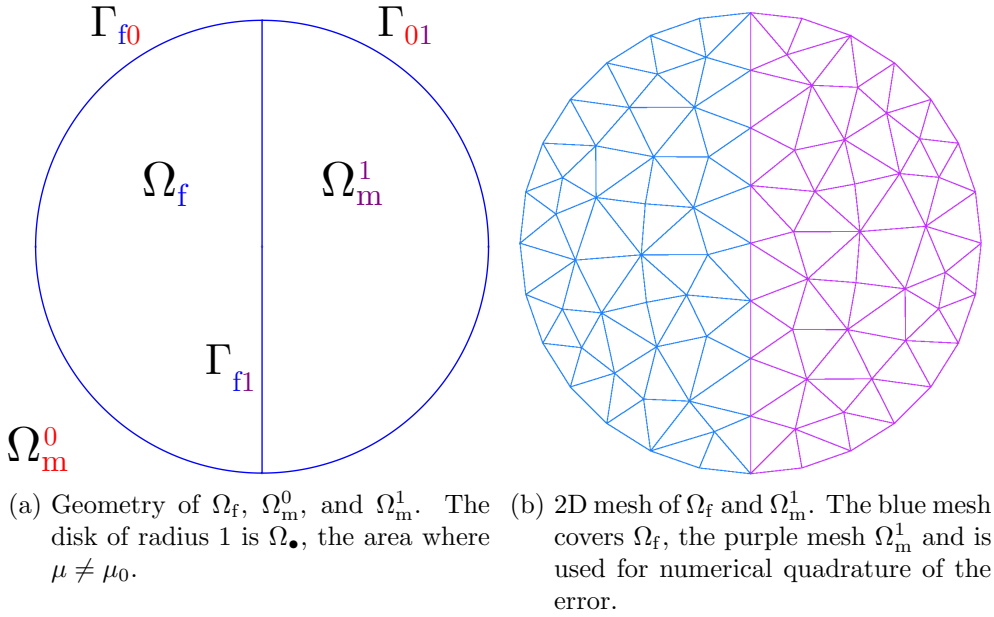
Figure 6.15: Geometry and sample mesh of Ω_f, Ω_m^0, and Ω_m^1.
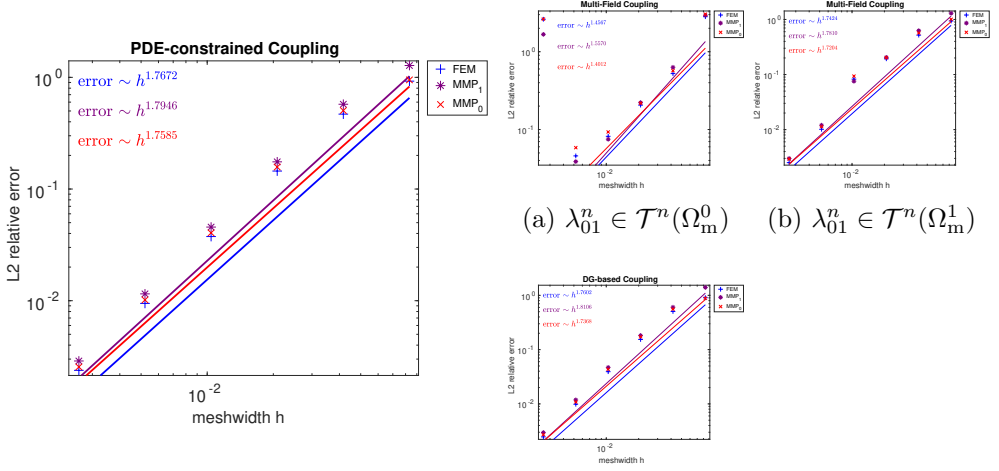
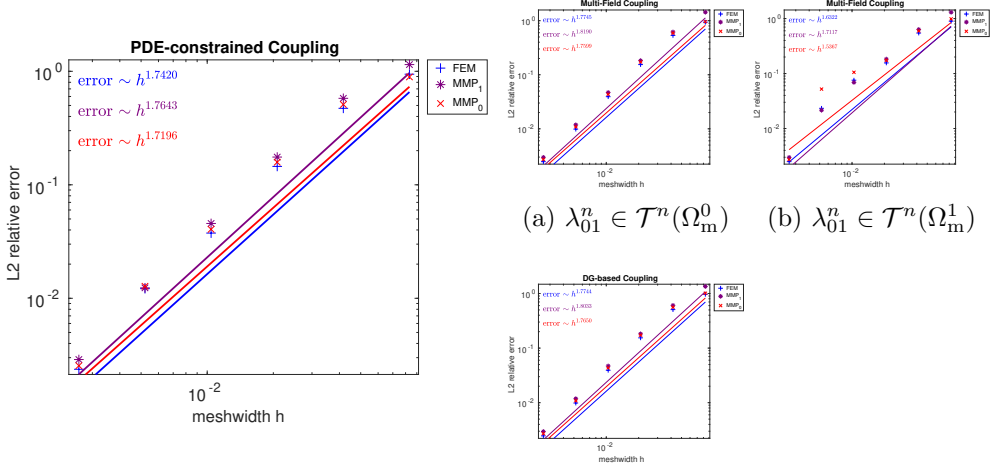Figure 6.16: h-refinement log-log error plots for 2D scattering with exact solution solved with two MMP domains. A single multipole expansion is used for each MMP domain. Parameters are $\mu_\bullet = 2.5281\,\mu_0$ and $\omega = 23.56 \cdot 10^8\,\mathrm{rad\,s^{-1}}$.

To approximate in Ω_{m}^1, a single multipole expansion with Bessel functions as radial dependence is centered in the origin: Bessel functions of the first kind have no singularities in that point, which lies on $\partial\Omega_{\mathrm{m}}^1$. To approximate in Ω_{m}^0, a single multipole expansion with Hankel functions as radial dependence is also centered in the origin.

Figure 6.16 shows h-refinement convergence plots for all coupling approaches, which yield very similar results except for the multi-field coupling with λ_{01}^n discretized by $\mathcal{T}^n(\Omega_{\mathrm{m}}^0)$: there is no convergence for the most refined mesh. This is because the number of degrees of freedom of $\mathcal{T}^n(\Omega_{\mathrm{m}}^0)$ for that mesh is not large enough to properly impose the continuity between Ω_{m}^0 and Ω_{m}^1. In all the other plots we can clearly see algebraic convergence of the FEM and MMP errors with rate ~ 1.7.

We have also considered a different configuration of multipoles. To approximate in Ω_{m}^1, multipole expansions of order 1 are uniformly positioned on a circle of radius 1.5 centered in $(0.5, 0)^\top$. To approximate in Ω_{m}^0, multipole expansions of order 1 are uniformly positioned on a circle of radius 0.5 centered in the origin.

Figure 6.17: *h*-refinement log-log error plots for 2D scattering with exact solution solved with two MMP domains. Many multipole expansions on circles are used for each MMP domain. Parameters are $\mu_\bullet = 2.5281\,\mu_0$ and $\omega = 23.56 \cdot 10^8\,\text{rad s}^{-1}$.

Figure 6.17 shows the corresponding *h*-refinement convergence plots, which look almost the same as Figure 6.16 but without any problem with the multi-field coupling for $\lambda_{01}^n \in \mathcal{T}^n(\Omega_m^0)$.

6.3.2 2D Scattering with Triple-Point Singularities

The problem is the same as in Section 6.3.1, but now we consider different values of μ in each half of the disk $\Omega_\bullet$. Specifically, we take $\mu_+ = 4\,\mu_0$ in the left side of $\Omega_\bullet$ and $\mu_- = 2.5281\,\mu_0$ in the right side. ω is still $= 23.56 \cdot 10^8\,\text{rad s}^{-1}$: wavenumbers are $k_+ = 2\,k_0$ and $k_- = 1.59\,k_0$. Hence, at the extremes of the segment splitting $\Omega_\bullet$ we have triple-point singularities.

We fully surround the points with TPS by a mesh, and therefore also model with FEM a small region on the other side of the physical discontinuity of $\Omega_\bullet$ and an "airbox" in $\mathbb{R}^2 \setminus \Omega_\bullet$. The coupling interfaces Γ_{f0} and Γ_{f1} are therefore auxiliary; only the interface Γ_{01} is physical. The FEM mesh is also locally refined towards the points with TPS: the meshwidth goes like $h_0 + r^3$, with

(a) Geometry of Ω_f, Ω_m^0, and Ω_m^1. The disk of radius 1 is $\Omega_\bullet$: in one half, $\mu = \mu_+$; in the other, $= \mu_-$. In the rectangle outside the disk, $\mu = \mu_0$.

(b) 2D mesh of Ω_f and Ω_m^1. The blue, pink, and green meshes cover Ω_f and are characterized by parameters μ_+, μ_-, and μ_0, respectively. The purple mesh covers Ω_m^1, is characterized by μ_-, and is used for numerical quadrature of the error.
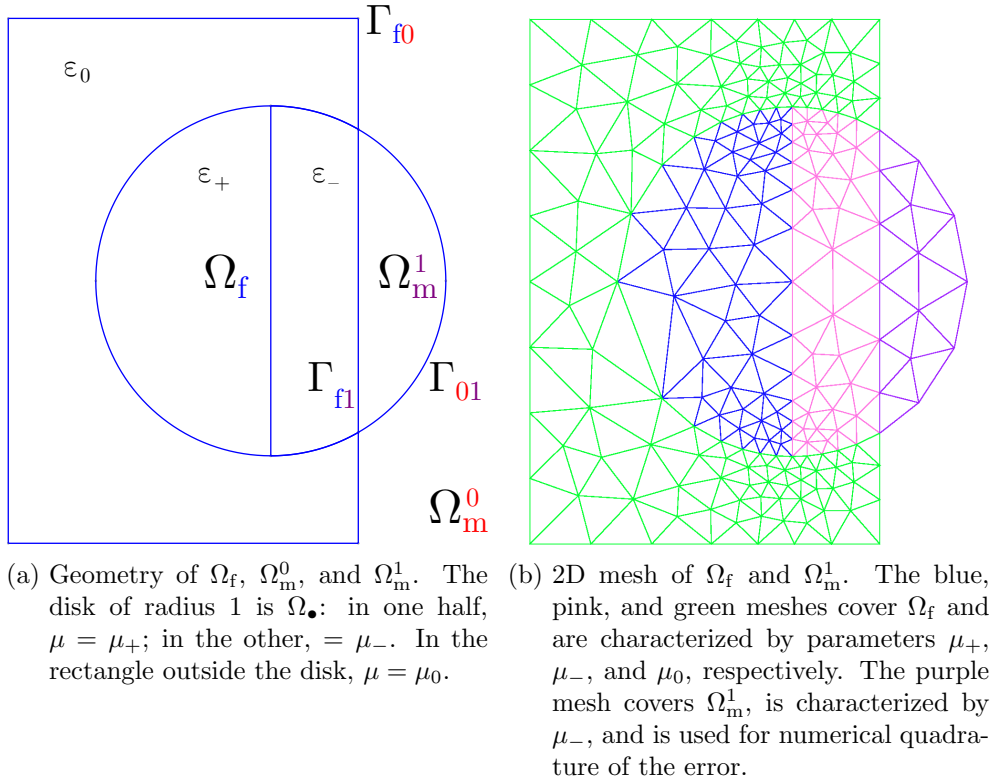
Figure 6.18: Geometry and sample mesh of Ω_f, Ω_m^1, and a part of Ω_m^0.

h_0 minimum meshwidth and r distance from the closest triple point. The geometry is shown in Figure 6.18a, with a sample mesh in Figure 6.18b.

The excitation is still given by a plane wave $u_{inc} := \exp(\imath k_0 z)$ that shifts the MMP ansatz in Ω_m^0. However, given the TPS, there is no exact solution: as reference we rely on the numerical solution provided by a mesh substantially more refined than the finest mesh used in the convergence study.

To approximate in Ω_m^1, multipole expansions of order 1 with Bessel functions as radial dependence are uniformly positioned on a circle of radius 1.5 centered in $(0.5, 0)^\top$. To approximate in Ω_m^0, multipole expansions of order 1 with Hankel functions as radial dependence are uniformly positioned on a circle of radius 0.5 centered in the origin.
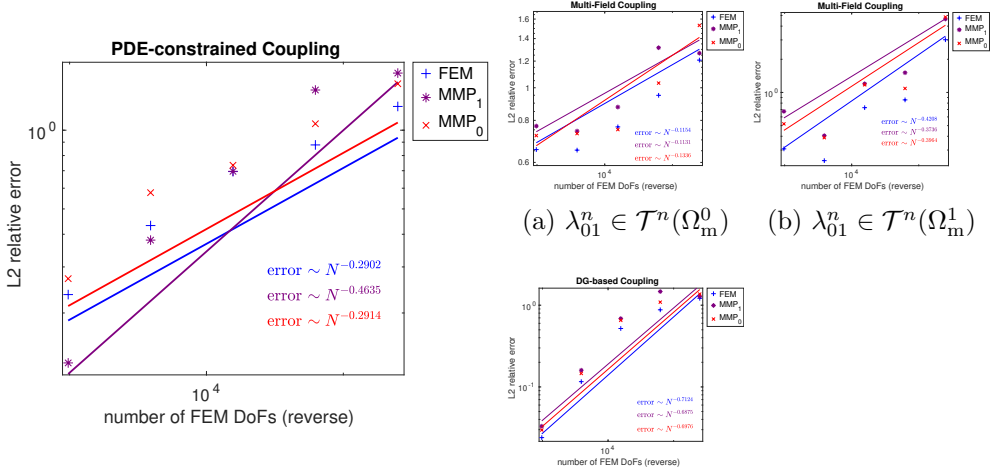
Figure 6.19: DoF-refinement log-log error plots for 2D scattering with TPS solved with two MMP domains (geometry in Figure 6.18a). Parameters are $\mu_+ = 4\,\mu_0$, $\mu_- = 2.5281\,\mu_0$, and $\omega = 23.56 \cdot 10^8\,\mathrm{rad}\,\mathrm{s}^{-1}$.

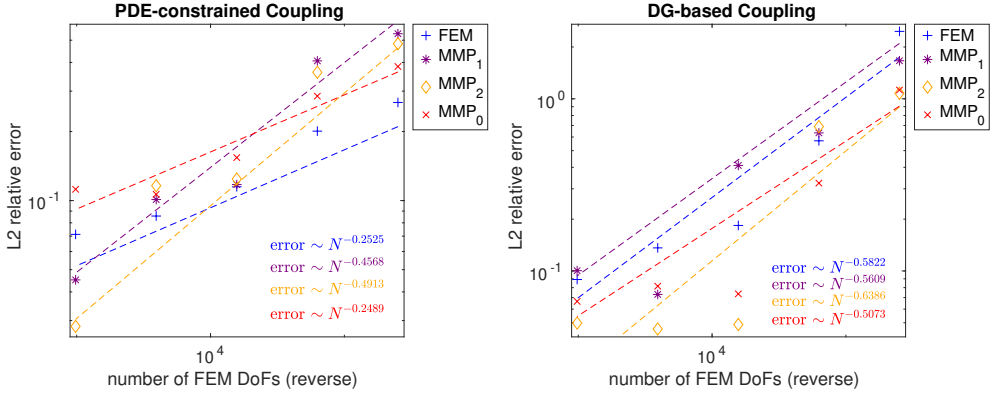Figure 6.19 shows DoF-refinement convergence plots for all coupling approaches. The PDE-constrained and DG-based coupling approaches have similar algebraic convergence patterns, but the datapoints of the multi-field coupling with multiplier $\lambda_{01}^n \in \mathcal{T}^n(\Omega_{\mathrm{m}}^0)$ or $\mathcal{T}^n(\Omega_{\mathrm{m}}^1)$, while they converge, are more irregular.

We repeat this experiment with the geometry shown in Figure 6.20a, where only the points with TPS and their immediate surrounding regions are modeled with FEM, so to minimize the meshed region. A sample mesh is shown in Figure 6.20b.

To approximate in Ω_{m}^1 and Ω_{m}^2, multipole expansions of order 1 are uniformly positioned on two circles of radius 1.5 centered in $(-0.5, 0)^\top$ and $(0.5, 0)^\top$, respectively. To approximate in Ω_{m}^0, multipole expansions of order 1 are uniformly positioned on a circle of radius 0.5 centered in the origin.

Figure 6.21 shows DoF-refinement convergence plots for the PDE-constrained and DG-based coupling approaches: we can still guess algebraic convergence.

(a) The geometry represents Ω_{f}, Ω_{m}^1, and Ω_{m}^2. The disk of radius 1 is $\Omega_\bullet$: in one half, $\mu = \mu_+$; in the other, $= \mu_-$. In the small squares outside the disk, $\mu = \mu_0$.

(b) 2D mesh of Ω_{f}, Ω_{m}^1, and Ω_{m}^2. The light blue, pink, and green meshes cover Ω_{f} and are characterized by parameters μ_+, μ_-, and μ_0, respectively. The blue mesh covers Ω_{m}^1 and is characterized by μ_+, the purple mesh covers Ω_{m}^2 and is characterized by μ_-: both are used for numerical quadrature of the error.

Figure 6.20: Geometry and sample mesh of Ω_{f}, Ω_{m}^1, and Ω_{m}^2.

Figure 6.21: DoF-refinement log-log error plots for 2D scattering with TPS solved with three MMP domains (geometry in Figure 6.20a). Parameters are $\mu_+ = 4\,\mu_0$, $\mu_- = 2.5281\,\mu_0$, and $\omega = 23.56 \cdot 10^8\,\mathrm{rad\,s^{-1}}$.

6.4 Magnetostatics

6.4.1 Magnetostatics with Exact Solution

We solve $\nabla \times \left(\mu^{-1}\nabla \times \mathbf{u}\right) = \mathbf{j}$, $\nabla \cdot \mathbf{u} = 0$ in $\mathbb{R}^3$ subject to the decay condition (1.4) with constant permeability $\mu_0 = 4\pi \cdot 10^{-7}\,\mathrm{H\,s^{-1}}$ (permeability of free space) everywhere. $\Omega_\star$, the domain where $\mathbf{j} \neq \mathbf{0}$, is a torus of radius 0.1 centered at $(0,0,0.5)^\top$ and with normal axis $\left(0, \frac{\sqrt{2}}{2}, \frac{\sqrt{2}}{2}\right)^\top$. In $\Omega_\star$, $\|\mathbf{j}\| = 1.05 \cdot 10^6\,\mathrm{A\,m^{-3}}$ and is tangential to the torus; elsewhere, $\mathbf{j} = \mathbf{0}$. A sample mesh of Ω_f is shown in Figure 6.22; the unbounded complement is the single MMP domain Ω_m.

We consider two different auxiliary boundaries Γ between Ω_f and Ω_m: two spheres centered in the origin of radius 4 and 2. Given that we use tetrahedral meshes, Γ is actually a polyhedral approximation of a sphere.

$\mathcal{T}^n(\Omega_\mathrm{m})$ is generated by multipole expansions uniformly positioned on a circle of radius 1 centered in the origin and lying on the XY-plane. This positioning has been chosen to show that, with auxiliary boundaries Γ, one can properly
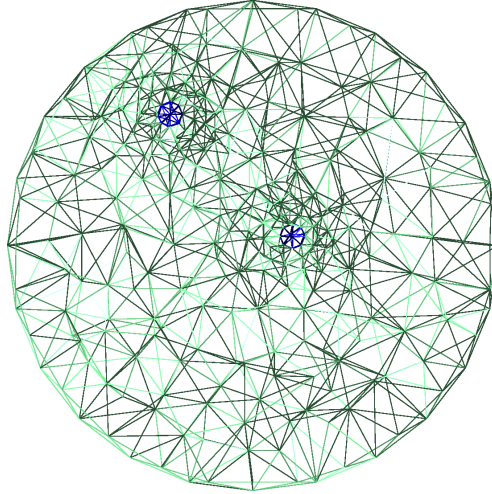
Figure 6.22: Cross-section of a 3D mesh of Ω_f along the YZ-plane. The blue mesh represents $\Omega_\star$. The green mesh covers a hollow ball centered in the origin that, in the mesh shown, has radius 2.

approximate $\mathbf{u}$ in Ω_m regardless of the locations of the multipoles. We only use multipole expansions of order 1.

Numerical Results

Figures 6.23 and 6.24 show h-refinement convergence plots for all coupling approaches, which lead to very similar plots. We can clearly identify a linear convergence of the FEM error when Γ has radius 4, while the convergence is slower with radius 2, when the multipoles are closer to the source in $\Omega_\star$.

In both cases, the MMP error decreases much more slowly. This is due to the fact that the exact solution is so easy to approximate in Ω_m that it can already be represented by very few multipoles.

Figures 6.25 and 6.26 show surface plots of the total relative $\mathbf{L}^2$-error for all coupling approaches. The error is much lower for Γ as a sphere of radius 4 than 2, decreases with h (algebraic convergence), and is generally independent of the number of multipoles.
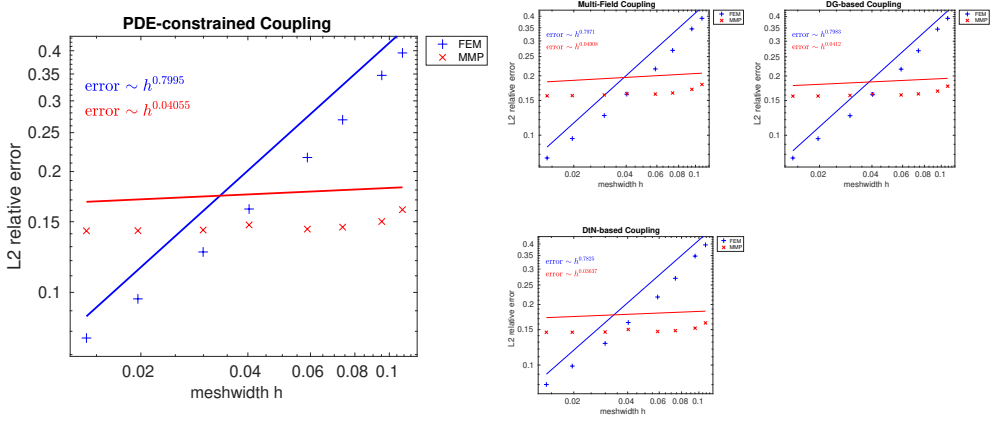
Figure 6.23: *h*-refinement log-log error plots for magnetostatic Maxwell's equations with exact solution. Γ is a sphere of radius 4.
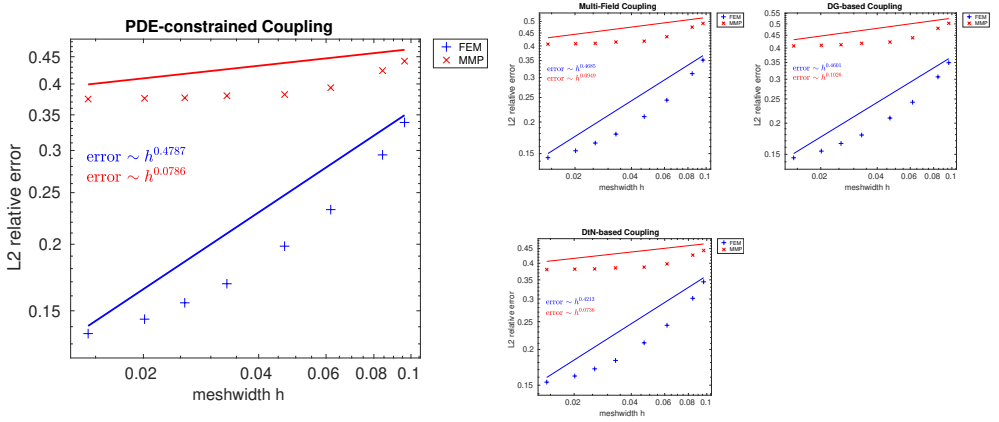
Figure 6.24: *h*-refinement log-log error plots for magnetostatic Maxwell's equations with exact solution. Γ is a sphere of radius 2.
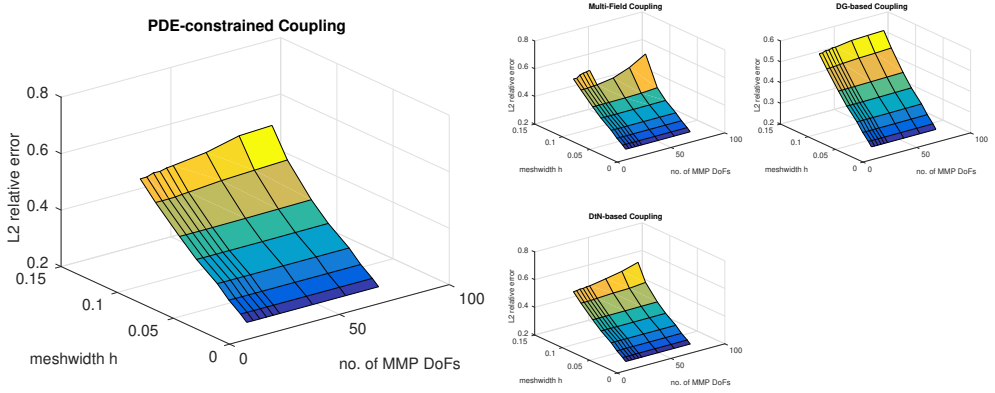
Figure 6.25: Meshwidth h vs. MMP degrees of freedom for magnetostatic Maxwell's equations with exact solution: total relative error. Γ is a sphere of radius 4.
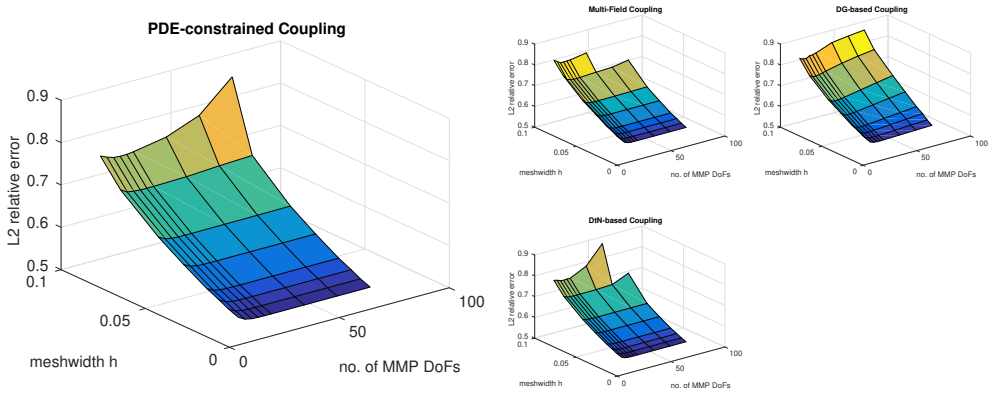
Figure 6.26: Meshwidth h vs. MMP degrees of freedom for magnetostatic Maxwell's equations with exact solution: total relative error. Γ is a sphere of radius 2.

However, the error also increases with the coarsest meshes and highest numbers of multipoles considered, when the coupling is mostly difficult due to a disproportionately large number of degrees of freedom for MMP (dense blocks of the coupling matrices) with respect to FEM (sparse blocks). In these cases, our conjecture is that it becomes difficult for a direct solver to properly solve such an ill-conditioned system, and the MMP error dominates.

All coupling approaches lead to similar plots, except for the multi-field and DG-based coupling, which exhibit even larger errors with the coarsest meshes and highest numbers of multipoles considered. Some of these errors for the multi-field coupling are so large that they have been omitted from the plots.

6.4.2 Magnetostatic Inductor

The problem is the same as in Section 6.4, but now $\Omega_\star$ is composed of three regions: two hollow cylinders and one hollow rectangular prism (see Figure 6.27b). In the cylinders, $\mathbf{j}$ is tangential to the lateral surfaces, with opposite directions and $\|\mathbf{j}\| = 1.05 \cdot 10^6 \,\mathrm{A\,m^{-3}}$ or $= 1.25 \cdot 10^6 \,\mathrm{A\,m^{-3}}$ in each of the cylinders. In the prism, $\mu \sim \|\nabla \times \mathbf{u}\|$ according to a given *nonlinear* curve (*hysteresis loop* [43, p. 290]). Elsewhere, $\mathbf{j} = \mathbf{0}$ and $\mu = \mu_0$.

The geometry of Ω_f is shown in Figure 6.27a, with a sample mesh in Figure 6.27b; the unbounded complement is the single MMP domain Ω_m. Local mesh refinement at the edges and corners of the prism inside Ω_f is needed because the solution is not smooth there.

$\mathcal{T}^n(\Omega_m)$ is generated by multipole expansions uniformly positioned on a rectangular prism with sizes $0.1 \times 0.1 \times 0.08$ that lies completely inside Ω_f (26 expansions). We only use multipole expansions of order 1.

Numerical Results

Figure 6.28 shows a plot of the magnitude of $\mathbf{u}$ along the XY-plane obtained with the DtN-based coupling (Section 3.4). Results were collected after 10 iterations to let $\mu \sim \|\nabla \times \mathbf{u}\|$ converge to a stable value for each part of $\mathcal{M}_f$.
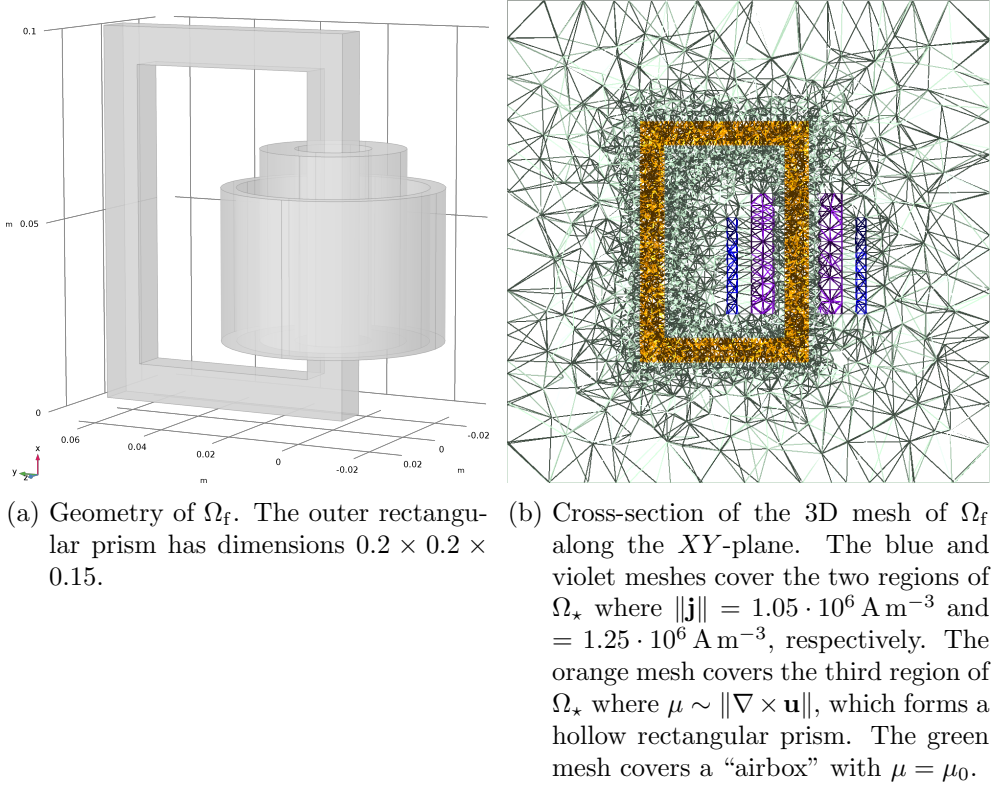
(a) Geometry of Ω_f. The outer rectangular prism has dimensions $0.2 \times 0.2 \times 0.15$.

(b) Cross-section of the 3D mesh of Ω_f along the XY-plane. The blue and violet meshes cover the two regions of $\Omega_\star$ where $\|\mathbf{j}\| = 1.05 \cdot 10^6\,\mathrm{A\,m}^{-3}$ and $= 1.25 \cdot 10^6\,\mathrm{A\,m}^{-3}$, respectively. The orange mesh covers the third region of $\Omega_\star$ where $\mu \sim \|\nabla \times \mathbf{u}\|$, which forms a hollow rectangular prism. The green mesh covers a "airbox" with $\mu = \mu_0$.

Figure 6.27: Geometry and sample mesh of Ω_f.
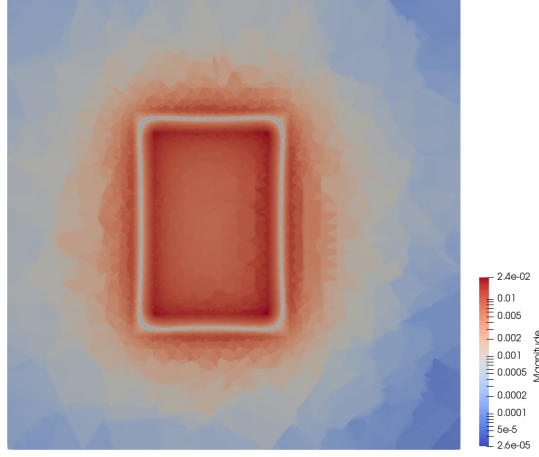
Figure 6.28: Magnitude of $\mathbf{u}$ along the XY-plane. Colors are in logarithmic scale. Plot obtained with the DtN-based coupling.

6.5 Eddy Current with $\mathbf{H}$-Φ Formulation

We solve the eddy-current problem (1.5) introduced in Section 1.1.4. As in [78], we use parameters $\sigma = 3.5 \cdot 10^7 \, \mathrm{Sv} \, \mathrm{m}^{-1}$, $\omega = 400\pi \, \mathrm{rad} \, \mathrm{s}^{-1}$, $\mu_{\mathrm{c}} = \mu_{\mathrm{n}} = 4\pi \cdot 10^{-7} \, \mathrm{T} \, \mathrm{m} \, \mathrm{A}^{-1}$, and $I = 200 \, \mathrm{A}$. Figure 6.29 illustrates the multiply-connected domain Ω^{c} and a part of $\Omega^{\mathrm{n}} =: \Omega_{\mathrm{f}}^{\mathrm{n}}$, which form $\Omega_{\mathrm{f}} := \Omega^{\mathrm{c}} \cup \Omega_{\mathrm{f}}^{\mathrm{n}}$.

The coupling between FEM and MMP is done on all the boundaries of Ω_{f} that do not intersect symmetry planes in Figure 6.29 (artificial interfaces). Hence, considering the variational form found in [13, p. 19, Problem DHP], we aim at finding a stationary point of the functional

$$
\begin{aligned}
\mathrm{J}_{\Omega_{\mathrm{f}}}(\mathbf{H}_{\mathrm{f}}, \Phi_{\mathrm{f}}) := &\int_{\Omega^{\mathrm{c}}} \sigma^{-1} \left(\nabla \times \mathbf{H}_{\mathrm{f}}\right) \cdot \left(\nabla \times \mathbf{H}_{\mathrm{f}}\right) \, \mathrm{d}\mathbf{x} + \\
&\imath\omega \int_{\Omega^{\mathrm{c}}} \mu_{\mathrm{c}} \, \mathbf{H}_{\mathrm{f}} \cdot \mathbf{H}_{\mathrm{f}} \, \mathrm{d}\mathbf{x} + \imath\omega \int_{\Omega_{\mathrm{f}}^{\mathrm{n}}} \mu_{\mathrm{n}} \, \nabla\Phi_{\mathrm{f}} \cdot \nabla\Phi_{\mathrm{f}} \, \mathrm{d}\mathbf{x}
\end{aligned}
\tag{6.5}
$$

subject to the interface conditions (1.6b) and

$$
\mathbf{n} \times \mathbf{H}_{\mathrm{f}} = \mathbf{n} \times \nabla\Phi_{\mathrm{f}} \quad \text{on } \partial_{\mathrm{cn}}\Omega_{\mathrm{f}}.
\tag{6.6}
$$

Figure 6.29: Geometry of Ω_f, formed by Ω^c (one octant of a holed wire) and a part of Ω^n (surrounding unbounded "airbox"). $\partial_D\Omega$ is the intersection with the XZ-plane (frontal face of the figure). $\partial_N\Omega$ comprises the boundaries that intersect the YZ- and XY-planes (right and bottom face, respectively). All the other (auxiliary) boundaries of the figure constitute the FEM–MMP coupling interface Γ.
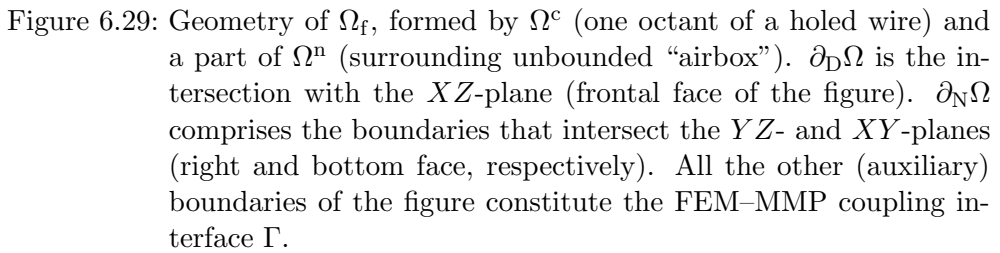
Note that (6.6) only includes one interface condition of (1.6a): the other is implied by (6.5).

As FEM discretization, given meshes of tetrahedra $\mathcal{M}_f$ on Ω_f, we approximate $\mathbf{H}_f \in \mathbf{H}(\mathbf{curl}, \Omega^c)$ with $\mathbf{V}^n(\mathcal{M}_f|_{\Omega^c})$ of (1.14b) and $\Phi_f \in H^1(\Omega_f^n)$ with $V^n(\mathcal{M}_f|_{\Omega_f^n})$ of (1.14a). The Dirichlet boundary conditions of (1.5) are imposed strongly by setting the affected degrees of freedom of $\mathbf{V}^n, V^n$ accordingly. Similarly, (6.6) is imposed by (scalar) Lagrange multipliers for each edge e of $\mathcal{M}_f$ on $\partial_{cn}\Omega_f$, relying on the identity

$$
\int\limits_{e_i} \mathbf{v}_i \cdot \mathbf{t}\,\mathrm{d}\vec{s} = v_{i1}(\mathbf{x}_{i1}) - v_{i2}(\mathbf{x}_{i2}), \quad i = 1, \ldots, N_{\text{edges}}^{\text{bnd}}, \tag{6.7}
$$

with $\mathbf{v}_i \in \mathbf{V}^n(\mathcal{M}_f)$, $v_{i1}, v_{i2} \in V^n(\mathcal{M}_f)$, $\mathbf{t}$ tangent, and $\mathbf{x}_{i1}, \mathbf{x}_{i2}$ corners of edge e_i: on the left of (6.7), one degree of freedom of Nédélec elements $\mathbf{V}^n(\mathcal{M}_f|_{\Omega^c})$ [67, p. 126, Section 5.5]; on the right, a pair of degrees of freedom of $V^n(\mathcal{M}_f|_{\Omega_f^n})$ [67, p. 143, Section 5.6].

Outside Ω_f, multipoles in $\mathcal{T}^n(\Omega_m)$ have the same formulation of (2.2b) (3D Poisson's equation) with the origin shifted inside Ω_f to avoid dealing with their singularities; more specifically, multipoles are uniformly positioned on a rectangular prism that lies completely inside Ω_f. However, to form a multipole that fully respects (1.5), in addition to (2.2b), there must be seven other terms whose origins are symmetrically disposed in the other octants of $\mathbb{R}^3$ such that the boundary conditions of (1.5) hold on the infinite symmetry planes of Ω^n ($\partial_N \Omega^n$ and $\partial_{D2} \Omega^n$).

For each center we consider multipoles up to order 1. The total number of multipoles is set proportional to the number of intersections of $\mathcal{M}_f$ with Γ.

Numerical Results

To validate our results, we first compute induced eddy currents I_3 and I_4, which are defined as surface integrals

$$
I_i := \int\limits_{\Sigma_i} \mathbf{n} \cdot (\nabla \times \mathbf{H})\,\mathrm{d}S, \quad i = 3, 4, \tag{6.8}
$$
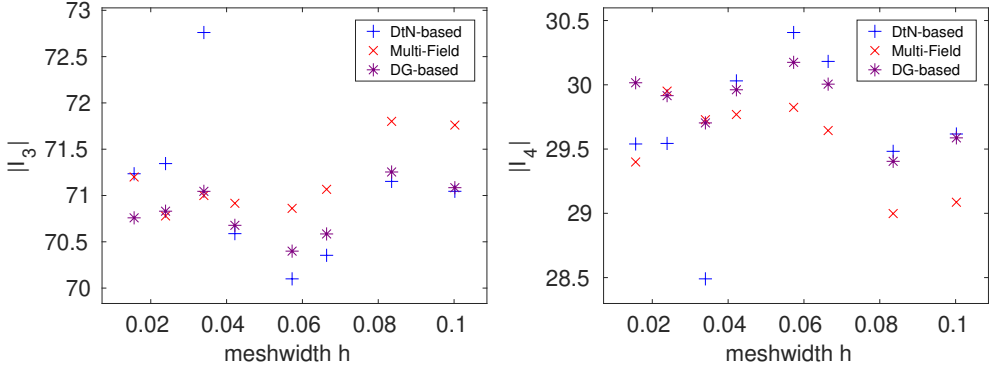
Figure 6.30: Eddy currents $|I_3|$ and $|I_4|$ for different mesh refinements of the geometry in Figure 6.29.

where Σ_3 and Σ_4 are surfaces cutting Ω^c on each side of the hole of Figure 6.29. For all meshes considered, the different coupling approaches return values similar to each other, with $|I_3| + |I_4|$ being very close to $I/2 = 100\,\mathrm{A}$, as expected from the theory. This is shown in Figure 6.30.

We also compute the power loss of the conductor L, which is defined as the integral

$$L := \int_{\Omega^c} \sigma \, \|\mathbf{E}\|^2 \, \mathrm{d}\mathbf{x} = \int_{\Omega^c} \sigma^{-1} \, \|\nabla \times \mathbf{H}\|^2 \, \mathrm{d}\mathbf{x}\,. \tag{6.9}$$

Again, Figure 6.31 shows that L stays constant throughout all our simulations, as expected.

Convergence tests for the relative $\mathbf{L}^2(\Omega_f)$-error of the $\mathbf{H}$-field with respect to the most refined mesh are presented in Figure 6.32. All coupling approaches exhibit an algebraic convergence with a similar rate.

Finally, Figure 6.33 illustrates the magnitude of the $\mathbf{H}$-field in Ω_f as seen from the front of Figure 6.29 (along the XZ-plane), applying the DtN-based coupling to the most refined mesh: the result agrees with engineering intuition. Figures for the other coupling approaches are also very similar.
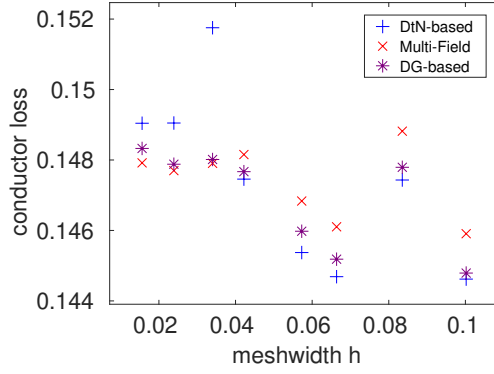
Figure 6.31: Power loss L for different mesh refinements of the geometry in Figure 6.29.
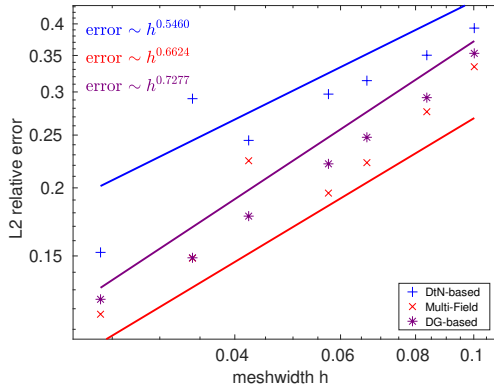
Figure 6.32: h-refinement log-log error plots for eddy-current equations.

Figure 6.33: Magnitude of the real component of $\mathbf{H}$ along the XZ-plane. Plot obtained with the DtN-based coupling.

6.6 Maxwell's Equations

6.6.1 Maxwell's Equations with Exact Solution

We solve $\nabla \times \left(\mu^{-1} \nabla \times \mathbf{u} \right) - \omega^2 \epsilon \, \mathbf{u} = \mathbf{0}$, $\nabla \cdot \mathbf{u} = 0$ in $\mathbb{R}^3$ subject to the Silver-Müller radiation condition (1.3b) with piecewise-constant permeability $\mu = 2.5281 \, \mu_0$ in a unit ball centered in the origin, which we dub $\Omega_\bullet$, and $\mu = \mu_0 = 4\pi \cdot 10^{-7} \, \mathrm{H \, s^{-1}}$ (permeability of free space) elsewhere. ϵ and ω are everywhere equal to $\epsilon_0 = 8.85 \cdot 10^{-12} \, \mathrm{F \, m^{-1}}$ (permittivity of free space) and $23.56 \cdot 10^8 \, \mathrm{rad \, s^{-1}}$, respectively. Wavenumbers are therefore $k_\bullet = 1.59 \, k_0$ in $\Omega_\bullet$ and $k_0 = 7.86 \, \mathrm{rad \, m^{-1}}$ elsewhere.

We assume that $\mathbf{u}$ is subject to an excitation by an incident plane wave propagating along the z-axis outside $\Omega_\bullet$, i.e.

$$\mathbf{u} = \mathbf{u}_{\mathrm{inc}} + \mathbf{u}_{\mathrm{ref}} \text{ in } \mathbb{R}^3 \setminus \Omega_\bullet, \quad \mathbf{u}_{\mathrm{inc}} := \exp(\imath k_0 z) \, (0, 1, 0)^\top, \tag{6.10}$$

where $\mathbf{u}_{\mathrm{ref}}$ represents the unknown reflected potential and z in $\mathbf{u}_{\mathrm{inc}}$ the third Cartesian coordinate. This problem has an exact solution coming from *Mie theory* [16, Chapter 4, pp. 82–101], where the plane wave is expanded into vector spherical harmonics [21, p. 289] and coefficients are derived for the
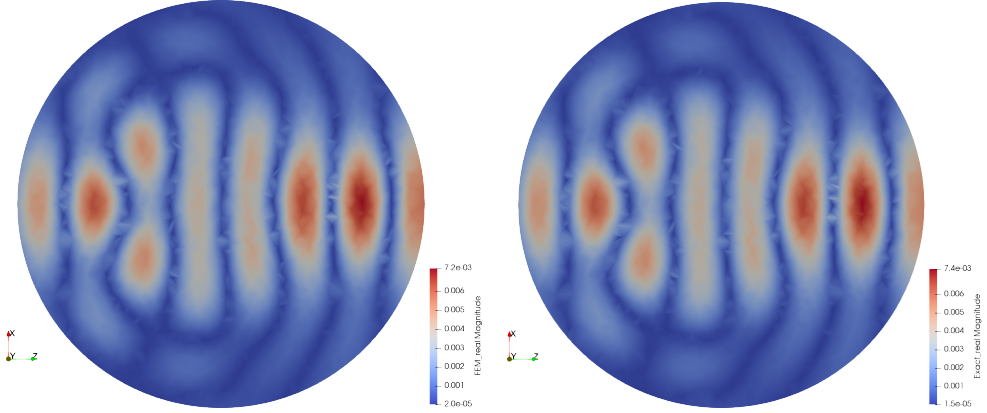
(a) Numerical solution obtained with the DtN-based coupling.

(b) Exact solution given by Mie theory.

Figure 6.34: Magnitude of the real component of $\mathbf{u}$ along the XZ-plane for $\mu_\bullet = 2.5281\,\mu_0$ and $\omega = 23.56 \cdot 10^8\,\mathrm{rad\,s^{-1}}$. The excitation is given by the expansion of a plane wave in terms of vector spherical harmonics (for $\ell = 1, \ldots, 5$) propagating along the z-axis.

corresponding terms of the expansions of the reflected and transmitted potentials.

For our numerical tests, we consider the terms in the expansions of Mie theory for $\ell = 1, \ldots, 5$ (35 terms), identify $\Omega_\bullet$ with Ω_f and $\mathbb{R}^3 \setminus \Omega_\bullet$ with a single MMP domain Ω_m, and therefore set $\Gamma := \partial\Omega_\mathrm{f} \cap \partial\Omega_\mathrm{m}$ on the physical boundary of the ball. Given that we use tetrahedral meshes, Γ is actually a polyhedral approximation of a sphere.

$\mathcal{T}^n(\Omega_\mathrm{m})$ is generated by a single multipole expansion centered in the origin.

Numerical Results

Figure 6.34 exemplifies the performance of FEM–MMP by visualizing the magnitude of $\mathbf{u}$ in the case of the DtN-based coupling (Section 3.4) compared to the exact solution. The other coupling schemes return comparable images.
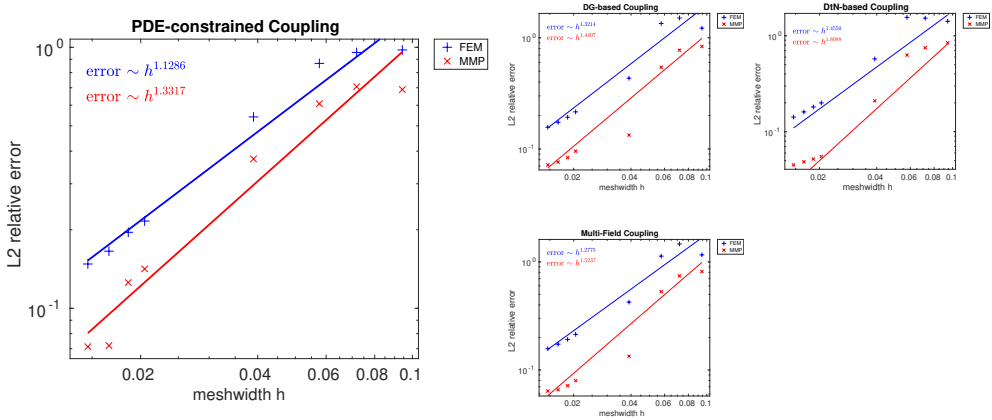
Figure 6.35: h-refinement log-log error plots for time-harmonic Maxwell's equations with exact solution. Parameters are $\mu_\bullet = 2.5281\,\mu_0$ and $\omega = 23.56 \cdot 10^8\,\mathrm{rad\,s}^{-1}$.

For a quantitative convergence test, see Figure 6.35, which shows h-refinement convergence plots for all coupling approaches, which yield very similar results. We can clearly see algebraic convergence of the FEM and MMP errors.

Figure 6.36 shows surface plots of the total relative $\mathbf{L}^2$-error for all coupling approaches. The error decreases with h (algebraic convergence) and is generally independent from the number of multipoles: the FEM error dominates. This is a consequence of the exponential convergence of MMP (Section 2.4): the exact solution is so easy to approximate in the MMP domain that it can already be represented by a multipole expansion of the lowest considered order, which is 8, leading to 160 terms of the expansion – see (2.4).

However, the error also increases with the coarsest meshes and highest numbers of multipoles considered, when the coupling is mostly difficult due to a disproportionately high number of degrees of freedom for MMP (dense blocks of the coupling matrices) with respect to FEM (sparse blocks). In these cases, our conjecture is that it becomes difficult for a direct solver to properly solve such an ill-conditioned system, and the MMP error dominates.

Moreover, we do not have datapoints for the PDE-constrained coupling with the most refined meshes and highest numbers of multipoles: the resulting linear
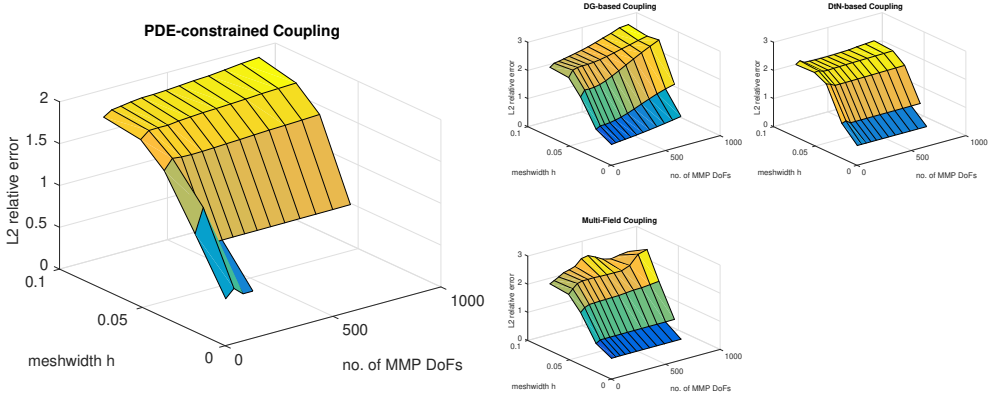
Figure 6.36: Meshwidth h vs. MMP degrees of freedom for time-harmonic Maxwell's equations with exact solution: total relative error. Parameters are $\mu_\bullet = 2.5281\,\mu_0$ and $\omega = 23.56 \cdot 10^8\,\mathrm{rad\,s}^{-1}$.

systems are too large to be solved by an LU decomposition due to memory constraints.

Two Trefftz Domains

Parameters are still $\mu_\bullet = 2.5281\,\mu_0$, $\epsilon_\bullet = \epsilon_0$, and $\omega = 23.56 \cdot 10^8\,\mathrm{rad\,s}^{-1}$. We split the unit ball $\Omega_\bullet$ into two halves, one modeled by FEM (Ω_f), the other by MMP (Ω_m^1): the coupling interface Γ_f1 is therefore artificial. MMP also models the complement $\mathbb{R}^3 \setminus \Omega_\bullet$ (Ω_m^0): the coupling boundaries Γ_f0 and Γ_01, on the two halves of the sphere, correspond to the physical discontinuity of μ. A sample mesh is shown in Figure 6.37.

As excitation, we consider terms for $\ell = 1, \ldots, 5$ from the expansion of a plane wave given by Mie theory.

To approximate in Ω_m^1, a single multipole expansion with spherical Bessel functions as radial dependence is centered in the origin: Bessel functions of the first kind have no singularities in that point, which lies on $\partial\Omega_\mathrm{m}^1$. To approximate in Ω_m^0, a single multipole expansion with spherical Hankel functions as radial dependence is also centered in the origin.

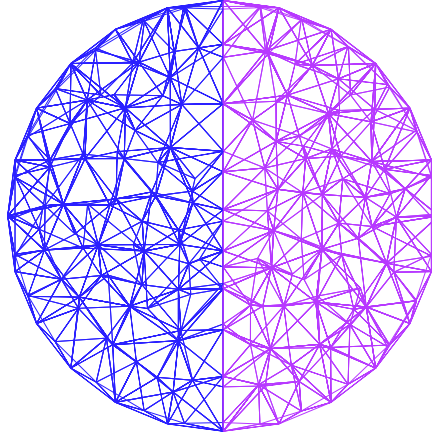Figure 6.37: Cross-section of a 3D mesh of Ω_f and Ω_m^1 along the XZ-plane. The ball of radius 1 is $\Omega_\bullet$, the volume where $\mu \neq \mu_0$. The blue mesh covers Ω_f, the purple one Ω_m^1, which is meshed for numerical quadrature of the error.
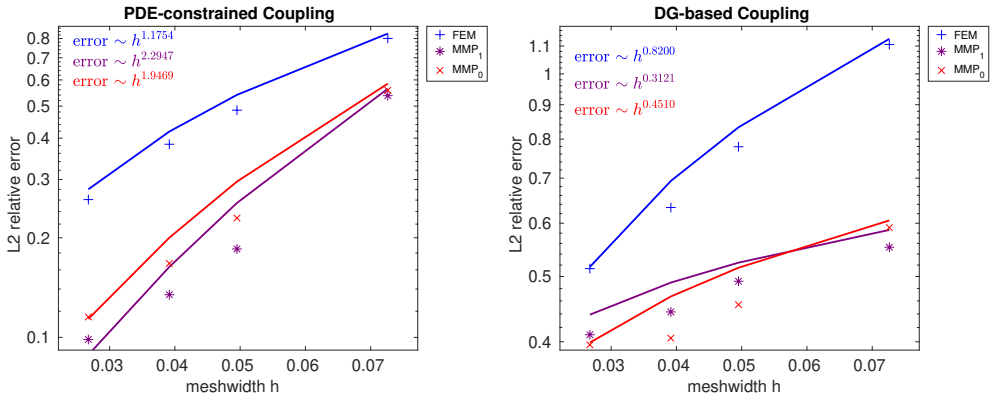

Figure 6.38: h-refinement semi-log error plots (y-axis) for time-harmonic Maxwell's equations with exact solution solved with two MMP domains. Parameters are $\mu_\bullet = 2.5281\,\mu_0$ and $\omega = 23.56 \cdot 10^8\,\mathrm{rad\,s^{-1}}$.

Figure 6.38 shows h-refinement convergence plots for all coupling approaches that work with multiple MMP domains (Sections 3.1 and 3.2). We can see algebraic convergence of the FEM and MMP errors, which is of rate ~ 1 for FEM.

6.6.2 Maxwell's Equations with Triple-Point Singularities

The problem is the same as in Section 6.6.1, but now we consider different values of μ in each half of the ball $\Omega_\bullet$. Specifically, we take $\mu_+ = 4\,\mu_0$ in one half of $\Omega_\bullet$ and $\mu_- = 2.5281\,\mu_0$ in the other half. ω is still $= 23.56 \cdot 10^8\,\mathrm{rad\,s^{-1}}$: wavenumbers are $k_+ = 2\,k_0$ and $k_- = 1.59\,k_0$. Hence, on the circumference that delimits the surface splitting $\Omega_\bullet$ we have triple-point singularities.

We fully surround the circumference with TPS by a mesh, and therefore also model with FEM a small region on the other side of the physical discontinuity of $\Omega_\bullet$ and an "airbox" in $\mathbb{R}^3 \setminus \Omega_\bullet$. The coupling interfaces Γ_{f0} and Γ_{f1} are therefore auxiliary; only the interface Γ_{01} is physical. The FEM mesh is also locally refined towards the points with TPS. A sample mesh is shown in Figure 6.39.

The excitation is still given by a plane wave $\mathbf{u}_{\mathrm{inc}} := \exp(\imath k_0 z)\,(0, 1, 0)^\top$ that shifts the MMP ansatz in Ω_{m}^0. However, given the TPS, there is no exact solution: as reference we rely on the numerical solution provided by a mesh substantially more refined than the finest mesh used in the convergence study.

To approximate in Ω_{m}^1, a single multipole expansion with spherical Bessel functions as radial dependence is centered in the origin. To approximate in Ω_{m}^0, a single multipole expansion with spherical Hankel functions as radial dependence is also centered in the origin.

Numerical Results

Figure 6.40 shows DoF-refinement convergence plots for all coupling approaches that work with multiple MMP domains. We can clearly see algebraic convergence of the FEM and MMP errors, even if the relative errors of the DG-based coupling are higher than those of the PDE-constrained approach.
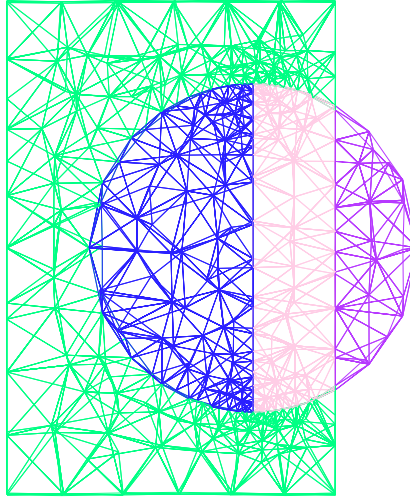
Figure 6.39: Cross-section of a 3D mesh of Ω_{f} and Ω_{m}^1 along the XZ-plane. The blue, pink, and green meshes cover Ω_{f} and are characterized by parameters μ_+, μ_-, and μ_0, respectively. The purple mesh covers Ω_{m}^1, is characterized by μ_-, and is used for numerical quadrature of the error. For better visualization, this mesh is not locally refined at the points with TPS (circumference touching the blue, pink, and green meshes).
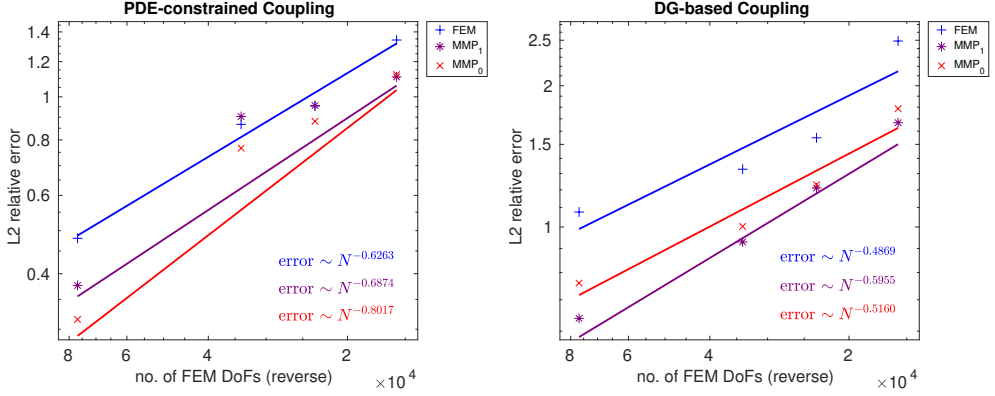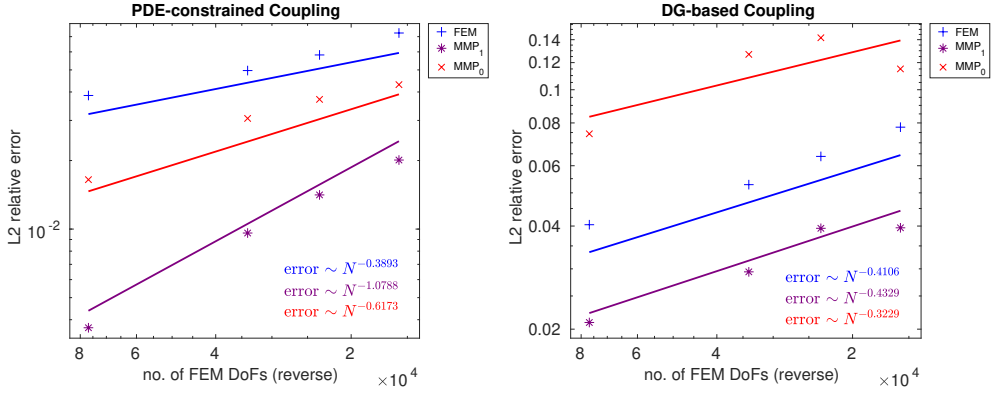
Figure 6.40: DoF-refinement log-log error plots for time-harmonic Maxwell's equations with TPS solved with two MMP domains (sample mesh in Figure 6.39). Parameters are $\mu_+ = 4\,\mu_0$, $\mu_- = 2.5281\,\mu_0$, and $\omega = 23.56 \cdot 10^8\,\text{rad}\,\text{s}^{-1}$.

We have also considered material parameters where the frequency ω is lower, and therefore FEM suffers less from the pollution effect, but the difference between μ_+, μ_-, and μ_0 is higher and the TPS more pronounced. Specifically, $\mu_+ = 10\,\mu_0$, $\mu_- = 4\,\mu_0$, and $\omega = 23.56 \cdot 10^7\,\text{rad}\,\text{s}^{-1}$.

Figure 6.41 shows DoF-refinement convergence plots for all coupling approaches that work with multiple MMP domains. Again, we can clearly see algebraic convergence of the FEM and MMP errors and the errors of the DG-based coupling are higher. However, while the convergence rate does not improve with respect to the plots of Figure 6.40, the values of the relative errors are much lower than before, given the easier-to-handle frequency.

Minimal FEM Mesh

We repeat these experiments with the meshes shown in Figure 6.42, where only the points with TPS and their immediate surrounding regions are modeled with FEM, so to minimize the meshed region. Hence, here we have three MMP domains: bounded $\Omega_{\text{m}}^1, \Omega_{\text{m}}^2$ (μ_+, μ_-) and unbounded Ω_{m}^0 (μ_0).

Figure 6.41: DoF-refinement log-log error plots for time-harmonic Maxwell's equations with TPS solved with two MMP domains (sample mesh in Figure 6.39). Parameters are $\mu_+ = 10\,\mu_0$, $\mu_- = 4\,\mu_0$, and $\omega = 23.56 \cdot 10^7\,\mathrm{rad\,s^{-1}}$.
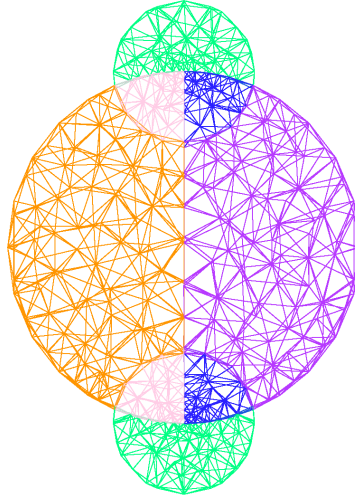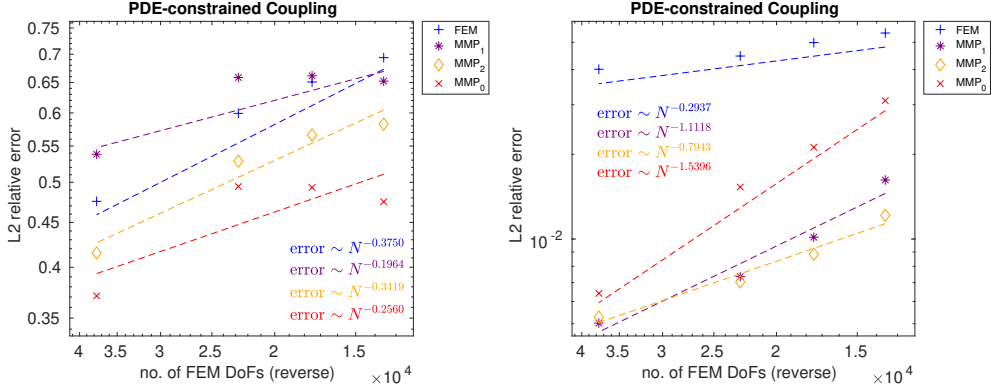

Figure 6.42: Cross-section of a 3D mesh of Ω_f, Ω_m^1, and Ω_m^2 along the XZ-plane. The blue, pink, and green meshes cover Ω_f and are characterized by parameters μ_+, μ_-, and μ_0, respectively. The purple and orange meshes cover Ω_m^1 and Ω_m^2, are characterized by μ_+ and μ_-, and are used for numerical quadrature of the errors.

(a) Parameters are $\mu_+ = 4\mu_0$, $\mu_- = 2.5281\mu_0$, and $\omega = 23.56 \cdot 10^8\,\mathrm{rad\,s^{-1}}$.

(b) Parameters are $\mu_+ = 10\mu_0$, $\mu_- = 4\mu_0$, and $\omega = 23.56 \cdot 10^7\,\mathrm{rad\,s^{-1}}$.

Figure 6.43: DoF-refinement log-log error plots for time-harmonic Maxwell's equations with TPS solved with three MMP domains (sample mesh in Figure 6.42) using the PDE-constrained coupling.

To approximate in Ω_{m}^1 and Ω_{m}^2, two multipole expansions with spherical Bessel functions as radial dependence are centered in the origin. To approximate in Ω_{m}^0, a multipole expansion with spherical Hankel functions as radial dependence is also centered in the origin.

Figure 6.43 shows DoF-refinement convergence plots for the PDE-constrained coupling, given

- $\mu_+ = 4\mu_0$, $\mu_- = 2.5281\mu_0$, and $\omega = 23.56 \cdot 10^8\,\mathrm{rad\,s^{-1}}$ in Figure 6.43a, and

- $\mu_+ = 10\mu_0$, $\mu_- = 4\mu_0$, and $\omega = 23.56 \cdot 10^7\,\mathrm{rad\,s^{-1}}$ in Figure 6.43b.

We can still see algebraic convergence of the FEM and MMP errors. Moreover, the values of the relative MMP errors in Figure 6.43b are again much lower than Figure 6.43a, given the lower frequency.

We do not report results for DG-based coupling because we would have to choose 6 penalty parameters η for $\Gamma_{\mathrm{f}j}, \Gamma_{ij}$, $i < j$, $j = 0, 1, 2$, and 3 discretization spaces $\mathcal{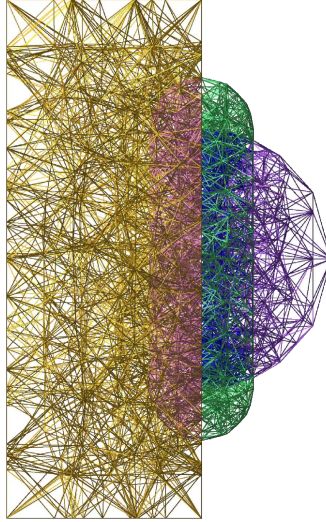T}^n(\Gamma_{ij})$ to impose normal continuity between $\Omega_{\mathrm{m}}^i, \Omega_{\mathrm{m}}^j$ (see Section 3.2).

Figure 6.44: Cross-section of a 3D mesh of Ω_{f}, Ω_{m}^1, and a part of Ω_{m}^0 along the XZ-plane. The blue, pink, and green meshes cover Ω_{f} and are characterized by parameters μ_+, μ_-, and μ_0, respectively. The purple and orange meshes cover Ω_{m}^1 and a part of Ω_{m}^0: they are characterized by μ_+ and μ_-. The mesh of Ω_{m}^1 is used for numerical quadrature of the error, while the mesh of Ω_{m}^0 only serve a graphical purpose.

Minimal FEM Mesh and Layered Medium

We consider a similar setting to Figure 6.42, where the FEM mesh only surrounds the TPS, and further introduce a substrate with permeability μ_- that occupies half of $\mathbb{R}^3$ (with negative z-axis). Hence, the ball $\Omega_\bullet$ becomes a half-ball with permeability μ_+ and there is a physical discontinuity between μ_- and μ_0 on the whole XY-plane: see a sample mesh in Figure 6.44.

To approximate in the half-ball Ω_{m}^1, multipole expansions with spherical Bessel functions as radial dependence are uniformly positioned on a rectangular prism that lies completely outside Ω_{m}^1. However, to approximate in Ω_{m}^0, which contains an infinite physical discontinuity,[2] we cannot make use of the standard

---

[2]Here, Ω_{m}^0 does not fit into the partition of Section 1.2, where we require that $(\mu, \epsilon) \in \mathbb{C}^2$
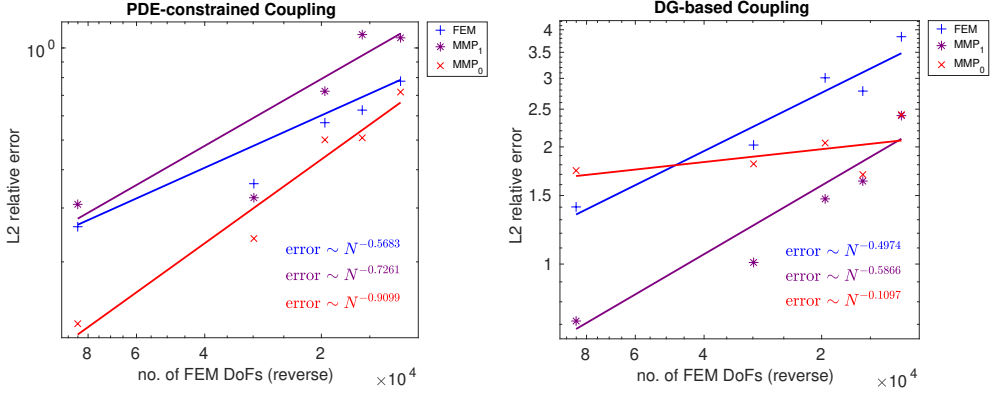
Figure 6.45: DoF-refinement log-log error plots for time-harmonic Maxwell's equations with TPS solved with two MMP domains (sample mesh in Figure 6.44) and layered dipoles. Parameters are $\mu_+ = 4\,\mu_0$, $\mu_- = 2.5281\,\mu_0$, and $\omega = 23.56 \cdot 10^8\,\mathrm{rad\,s}^{-1}$.

multipoles from Section 2.2.

We therefore use *layered dipoles* [60, p. 128, Section 6.3.2], which rely on the *layered-media Green's functions* reported in [3, p. 81, Appendix A] and [4]. Layered dipoles in Ω_{m}^0 are also shifted by plane waves

$$\mathbf{u}_{\mathrm{inc}} + \mathbf{u}_{\mathrm{ref}} \qquad\qquad\qquad\qquad\qquad \text{with } z \geq 0,$$
$$\mathbf{u}_{\mathrm{inc}} \coloneqq \exp(\imath k_0 z)\,(0,1,0)^\top, \quad \mathbf{u}_{\mathrm{ref}} \coloneqq \exp(-\imath k_0 z)\,(0,1,0)^\top A_{\mathrm{ref}},$$
$$\mathbf{u}_{\mathrm{trs}} \coloneqq \exp(\imath k_- z)\,(0,1,0)^\top A_{\mathrm{trs}} \qquad\qquad\qquad \text{with } z < 0,$$

$$(6.11)$$

where $A_{\mathrm{ref}} = \frac{\sqrt{\mu_0} - \sqrt{\mu_-}}{\sqrt{\mu_0} + \sqrt{\mu_-}}$, $A_{\mathrm{trs}} = \frac{2\sqrt{\mu_-}}{\sqrt{\mu_0} + \sqrt{\mu_-}}$, and z_+, z_- are halves of $\mathbb{R}^3$ with positive/negative z-axis. (6.11) can be derived from standard results of reflection and transmission of plane waves with normal incidence [43, p. 403, Section 9.3.2].

Figures 6.45 and 6.46 shows DoF-refinement convergence plots for both the PDE-constrained and DG-based coupling approaches and both sets of parameters used in the previous experiments. We can see algebraic convergence of
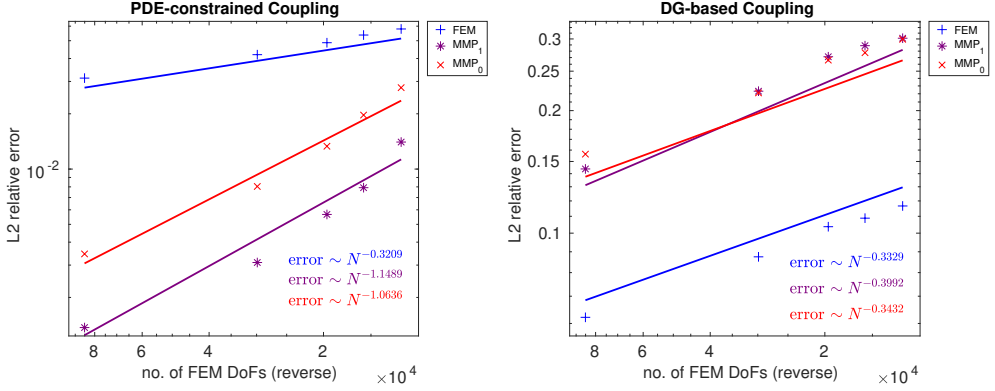
---

is constant in Ω_{m}^0.

Figure 6.46: DoF-refinement log-log error plots for time-harmonic Maxwell's equations with TPS solved with two MMP domains (sample mesh in Figure 6.44) and layered dipoles. Parameters are $\mu_+ = 10 \, \mu_0$, $\mu_- = 4 \, \mu_0$, and $\omega = 23.56 \cdot 10^7 \, \mathrm{rad \, s^{-1}}$.

the FEM and MMP errors: in particular, the FEM convergence rates of both approaches are very similar to each other.

At the same time, plots for the higher frequency $\omega = 23.56 \cdot 10^8 \, \mathrm{rad \, s^{-1}}$ (Figure 6.45) look more irregular because of the FEM pollution effect, especially the one obtained with the DG-based coupling, where the relative errors are quite high (like in the previous experiments). With a lower frequency (Figure 6.46), while the relative errors of the DG-based coupling are still higher than the PDE-constrained coupling, they are at most 0.3 even for the coarsest mesh employed, and all datapoints are aligned very closely to the fitted lines.

7 Conclusions

We have already addressed some advantages of Trefftz methods with respect to BEM in the introduction. Another relevant feature for high-frequency scattering problems is that the locally-supported piecewise-polynomial basis functions of boundary element methods [75, p. 183, Chapter 4] may suffer from the pollution effect like FEM, which is not a problem for the oscillating Trefftz basis functions. Moreover, coupling Trefftz methods with FEM allows to reduce the impact of heuristics on the quality of Trefftz solutions, arguably the major flaw of such methods, as long as the Trefftz domain avoids singularities.

However, similarly to other hybrid methods, the FEM–Trefftz coupling suffers from ill-conditioning. At the same time, its impact is still more limited than FEM coupled with BEM due to the low number of degrees of freedom required for Trefftz methods, given their exponential convergence: the dense Trefftz blocks in the coupling matrices are small (an order of $10^2 \times 10^2$ entries for a usual implementation).

Between the two coupling approaches that work with multiple Trefftz domains (Sections 3.1 and 3.2), we recommend the PDE-constrained coupling thanks to its reliability, especially when the FEM mesh only surrounds field singularities. Even though this coupling requires the highest number of degrees of freedom due to its Lagrange multipliers on the FEM mesh, this number is still low in absolute terms when such mesh is minimal. The DG-based coupling is less expensive, as it relies on fewer variables, but requires the additional user input of appropriate penalty parameters.

Conversely, among all coupling strategies, methods based on the tangential components trace stand out (Sections 3.3 and 3.4): both the multi-field and DtN-based approaches combine a sensibly lower number of degrees of freedom than the PDE-constrained coupling without the penalty parameters of the DG-based one. In particular, the DtN-based coupling is the easiest to implement:

7 Conclusions

Trefftz degrees of freedom can even be eliminated by a Schur complement approach, paving the way for an iterative solver (Chapter 4 and Figure 5.1).

References

[1] CMake v3.14.5. `https://cmake.org`, 2019.

[2] Milton Abramowitz and Irene Ann Stegun. *Handbook of Mathematical Functions with Formulas, Graphs, and Mathematical Tables*. Dover, New York, NY, 9th edition, 1964.

[3] Aytaç Alparslan. *Numerical Analysis of Photonic Nano Structures in Layered Geometries*. PhD thesis, Institute of Electromagnetic Fields, ETH Zurich, Switzerland, 2013.

[4] Aytaç Alparslan, M. İrşadi Aksun, and Krzysztof Arkadiusz Michalski. Closed-form Green's functions in planar layered media for all ranges and materials. *IEEE Transactions on Microwave Theory and Techniques*, 58(3):602–613, March 2010.

[5] Douglas Norman Arnold, Franco Brezzi, Bernardo Cockburn, and Luisa Donatella Marini. Unified analysis of Discontinuous Galerkin methods for elliptic problems. *SIAM Journal on Numerical Analysis*, 39(5):1749–1779, 2002.

[6] Douglas Norman Arnold, Richard S. Falk, and Ragnar Winther. Finite element exterior calculus, homological techniques, and applications. *Acta Numerica*, 15:1–155, May 2006.

[7] Hagit Attiya and Jennifer Welch. *Distributed Computing: Fundamentals, Simulations, and Advanced Topics*. Wiley, New York, NY, 2nd edition, March 2004.

[8] Markus Aurada, Michael Feischl, Thomas Führer, Michael Karkulik, Jens Markus Melenk, and Dirk Praetorius. Classical FEM-BEM coupling methods: nonlinearities, well-posedness, and adaptivity. *Computational Mechanics*, 51(4):399–419, April 2013.

References

[9] Ivo M. Babuška and Stefan A. Sauter. Is the pollution effect of the FEM avoidable for the Helmholtz equation considering high wave numbers? *SIAM Review*, 42(3):451–484, September 2000.

[10] Randolph E. Bank and Harry Yserentant. On the H^1-stability of the L^2-projection onto finite element spaces. *Numerische Mathematik*, 126(2):361–381, February 2014.

[11] Alex H. Barnett and Timo Betcke. An exponentially convergent nonpolynomial finite element method for time-harmonic scattering from polygons. *SIAM Journal on Scientific Computing*, 32(3):1417–1441, 2010.

[12] Roland Becker. Some applications of Nitsche's method. `http://www. math.iitb.ac.in/~neela/CIMPA/notes/nitsche1.pdf`, July 2015.

[13] Alfredo Bermúdez, Rodolfo Rodríguez, and Pilar Salgado. Finite element methods for 3D eddy current problems in bounded domains subject to realistic boundary conditions. An application to metallurgical electrodes. *Archives of Computational Methods in Engineering*, 12(1):67–114, January 2005.

[14] Christine Bernardi, Yvon Maday, and Francesca Rapetti. Basics and some applications of the mortar element method. *GAMM-Mitteilungen*, 28(2):97–123, May 2005.

[15] Pete Bettess, D.W. Kelly, and Olgierd Cecil Zienkiewicz. Marriage à la mode. The best of both worlds (Finite elements and boundary integrals). In Roland Glowinski, E.Y. Rodin, and Olgierd Cecil Zienkiewicz, editors, *Energy Methods in Finite Element Analysis*, chapter 5, pages 82–107. Wiley, Chichester, 1979.

[16] Craig F. Bohren and Donald R. Huffman. *Absorption and Scattering of Light by Small Particles*. Wiley, 1st edition, April 1998.

[17] Alain Bossavit. 'Generalized finite differences' in computational electromagnetics. *Progress In Electromagnetics Research*, 32:45–64, 2001.

[18] Dietrich Braess. *Finite Elements: Theory, Fast Solvers, and Applications in Solid Mechanics*. Cambridge University Press, Cambridge, 3rd edition, 2007.

[19] James Henry Bramble, Joseph E. Pasciak, and Olaf Steinbach. On the stability of the L^2 projection in $H^1(\Omega)$. *Mathematics of Computation*, 71(237):147–156, January 2002.

[20] Franco Brezzi and Luisa Donatella Marini. A three-field domain decomposition method. In *Domain Decomposition Methods in Science and Engineering*, volume 157 of *Contemporary Mathematics*, pages 27–34. American Mathematical Society, Providence, RI, 1994.

[21] B. Carrascal, G.A. Estevez, Peilian Lee, and V. Lorenzo. Vector spherical harmonics and their application to classical electrodynamics. *European Journal of Physics*, 12(4):184–191, 1991.

[22] Carsten Carstensen. Merging the Bramble-Pasciak-Steinbach and the Crouzeix-Thomée criterion for H^1-stability of the L^2-projection onto finite element spaces. *Mathematics of Computation*, 71(237):157–163, January 2002.

[23] Raffael Casagrande. *Discontinuous Finite Element Methods for Eddy Current Simulation*. PhD thesis, Seminar for Applied Mathematics, ETH Zurich, Switzerland, 2017.

[24] Raffael Casagrande and Christoph Winkelmann. Hybrid Discontinuous finite elements for power devices (HyDi), 2016. ABB Corporate Research Center.

[25] Raffael Casagrande, Christoph Winkelmann, Ralf Hiptmair, and Joerg Ostrowski. DG treatment of non-conforming interfaces in 3D curl-curl problems. In *Scientific Computing in Electrical Engineering*, volume 23 of *Mathematics in Industry*, pages 53–61. Springer, Cham, 2016.

[26] Daniele Casati, Lorenzo Codecasa, Ralf Hiptmair, and Federico Moro. Trefftz co-chain calculus. Technical Report 2019-19, Seminar for Applied Mathematics, ETH Zürich, Switzerland, April 2019.

[27] Daniele Casati and Ralf Hiptmair. Coupling FEM with a multiple-subdomain Trefftz method. Technical Report 2019-45, Seminar for Applied Mathematics, ETH Zürich, Switzerland, September 2019.

References

[28] Daniele Casati and Ralf Hiptmair. Coupling finite elements and auxiliary sources. *Computers & Mathematics with Applications*, 77(6):1513–1526, March 2019.

[29] Daniele Casati, Ralf Hiptmair, and Jasmin Smajic. Coupling finite elements and auxiliary sources for Maxwell's equations. *International Journal of Numerical Modelling: Electronic Networks, Devices and Fields*, December 2018.

[30] Daniele Casati, Jasmin Smajic, and Ralf Hiptmair. $\mathbf{H}$-ϕ field formulation with lumped sources and unbounded domains. *IEEE Transactions on Magnetics*, forthcoming.

[31] Weng Cho Chew. *Waves and Fields in Inhomogenous Media*. Undergraduate Texts in Mathematics. Wiley-IEEE Press, New York, NY, 1st edition, 1995.

[32] David Colton and Rainer Kress. *Inverse Acoustic and Electromagnetic Scattering Theory*, volume 93 of *Applied Mathematical Sciences*. Springer, Heidelberg, 3rd edition, 2013.

[33] COMSOL, Inc. COMSOL Multiphysics v5.3a.

[34] Beman Dawes, David Abrahams, et al. Boost C++ Libraries v1.71.0. `https://www.boost.org`, 2019.

[35] Joey Dumont and Denis Gagnon. complex_bessel. `https://github.com/joeydumont/complex_bessel`, 2019.

[36] Lawrence Craig Evans. *Partial Differential Equations*, volume 19 of *Graduate Studies in Mathematics*. American Mathematical Society, Providence, RI, 2nd edition, March 2010.

[37] Theodore William Gamelin. *Complex Analysis*. Undergraduate Texts in Mathematics. Springer, New York, NY, 1st edition, 2001.

[38] Erich Gamma, Richard Helm, Ralph Johnson, and John Vlissides. *Design Patterns: Elements of Reusable Object-oriented Software*. Addison-Wesley, Boston, MA, 1995.

[39] Klaus Gerdes. A summary of infinite element formulations for exterior Helmholtz problems. *Computer Methods in Applied Mechanics and Engineering*, 164(1):95–105, 1998.

[40] Christophe Geuzaine, Jean-François Remacle, et al. Gmsh v4.4.1, 2019. `http://gmsh.info`.

[41] Vivette Girault and Pierre-Arnaud Raviart. *Finite Element Methods for Navier-Stokes Equations*, volume 5 of *Springer Series in Computational Mathematics*. Springer, Berlin, Heidelberg, 1st edition, 1986.

[42] Leslie Greengard and June-Yub Lee. Stable and accurate integral equation methods for scattering problems with multiple material interfaces in two dimensions. *Journal of Computational Physics*, 231:2389–2395, March 2012.

[43] David Jeffrey Griffiths. *Introduction to Electrodynamics*. Pearson, Boston, MA, 4th edition, 2013.

[44] Gaël Guennebaud, Benoît Jacob, et al. Eigen v3.3.7. `http://eigen.tuxfamily.org`, 2018.

[45] Miklos Gyimesi, Igor Tsukerman, Doug Lavers, Tim Pawlak, and Dale Ostergaard. Hybrid finite element-trefftz method for open boundary analysis. *IEEE Transactions on Magnetics*, 32(3):671–674, May 1996.

[46] Christian Hafner. *Beiträge zur Berechnung der Ausbreitung elektromagnetischer Wellen in zylindrischen Strukturen mit Hilfe des "Point-Matching"-Verfahrens*. PhD thesis, ETH Zurich, Switzerland, 1980.

[47] Christian Hafner. Chapter 3 - The Multiple Multipole Program (MMP) and the Generalized Multipole Technique (GMT). In Thomas Wriedt, editor, *Generalized Multipole Techniques for Electromagnetic and Light Scattering*, Mechanics and Mathematical Methods–Series of Handbooks, pages 21–38. Elsevier, Amsterdam, December 1999.

[48] Christian Hafner. OpenMaXwell. `https://openmax.ethz.ch`, 2014. Institute of Electromagnetic Fields, ETH Zurich.

[49] Alexander Heifetz, Soon-Cheol Kong, Alan V. Sahakian, Allen Taflove, and Vadim Backman. Photonic nanojets. *Journal of Computational and Theoretical Nanoscience*, 6(9):1979–1992, September 2009.

References

[50] Michael Hinze, Rene Pinnau, Michael Ulbrich, and Stefan Ulbrich. *Optimization with PDE Constraints*, volume 23 of *Mathematical Modelling: Theory and Applications*. Springer, Houten, 1st edition, March 2009.

[51] Ralf Hiptmair. Discrete Hodge operators. *Numerische Mathematik*, 90(2):265–289, December 2001.

[52] Ralf Hiptmair. Discrete Hodge-operators: an algebraic perspective. *Progress In Electromagnetics Research*, 32:247–269, 2001.

[53] Ralf Hiptmair. Finite elements in computational electromagnetism. *Acta Numerica*, 11:237–339, January 2002.

[54] Ralf Hiptmair, Andrea Moiola, and Ilaria Perugia. *A survey of Trefftz methods for the Helmholtz equation*, pages 237–279. Springer, Cham, October 2016.

[55] Ralf Hiptmair and Oliver Sterz. Current and voltage excitations for the eddy current model. *International Journal of Numerical Modelling: Electronic Networks, Devices and Fields*, 18(1):1–21, January 2005.

[56] Anil Nirmal Hirani. *Discrete Exterior Calculus*. PhD thesis, California Institute of Technology, May 2003.

[57] John David Jackson. *Classical Electrodynamics*. Wiley, New York, NY, 3rd edition, 1999.

[58] Jian-Ming Jin. *The Finite Element Method in Electromagnetics*. Wiley-IEEE Press, New York, NY, 2nd edition, June 2002.

[59] Steven G. Johnson. Notes on Perfectly Matched Layers (PMLs). `http://math.mit.edu/~stevenj/18.369/pml.pdf`, March 2010.

[60] Ueli Koch, Jens Niegemann, Christian Hafner, and Juerg Leuthold. MMP simulation of plasmonic particles on substrate under e-beam illumination. In Thomas Wriedt and Yuri Eremin, editors, *The Generalized Multipole Technique for Light Scattering: Recent Developments*, pages 121–145. Springer, Cham, 2018.

[61] Victor Dmitrievich Kupradze and Merab Aleksandrovich Aleksidze. The method of functional equations for the approximate solution of certain

boundary value problems. *USSR Computational Mathematics and Mathematical Physics*, 4(4):82–126, 1964.

[62] Michael Ludwig. 3D graphics-oriented spherical harmonics library. `https://github.com/google/spherical-harmonics`, 2019. Google.

[63] Isaak D. Mayergoyz. A new approach to the calculation of three-dimensional skin effect problems. *IEEE Transactions on Magnetics*, 19(5):2198–2200, September 1983.

[64] William McLean. *Strongly Elliptic Systems and Boundary Integral Equations*. Cambridge University Press, Cambridge, UK, 1st edition, 2000.

[65] Gustav Mie. Elektrische Wellen an zwei parallelen Drähten. *Annalen der Physik*, 307:201–249, 1900.

[66] Andrea Moiola. *Trefftz-Discontinuous Galerkin Methods for Time-Harmonic Wave Problems*. PhD thesis, Seminar for Applied Mathematics, ETH Zurich, Switzerland, 2011.

[67] Peter Monk. *Finite Element Methods for Maxwell's Equations*. Clarendon Press, 1st edition, 2003.

[68] Federico Moro and Lorenzo Codecasa. Indirect coupling of the cell method and BEM for solving 3-D unbounded magnetostatic problems. *IEEE Transactions on Magnetics*, 52(3):1–4, March 2016.

[69] Federico Moro and Lorenzo Codecasa. A 3-D hybrid cell boundary element method for time-harmonic eddy current problems on multiply connected domains. *IEEE Transactions on Magnetics*, 55(3):1–11, March 2019.

[70] Nobuhiro Moteki. gmie_cpp. `https://github.com/nmoteki/gmie_cpp`, 2016.

[71] H. Murakami, S. Shioya, R. Yamada, and Juan Enrique Luco. Transmitting boundaries for time-harmonic elastodynamics on infinite domains. *International Journal for Numerical Methods in Engineering*, 17(11):1697–1716, 1981.

References

[72] Frédéric Nataf. Absorbing boundary conditions and perfectly matched layers in wave propagation problems. In Ivan Graham, Ulrich Langer, Jens Melenk, and Mourad Sini, editors, *Direct and Inverse problems in Wave Propagation and Applications*, volume 14 of *Radon Series on Computational and Applied Mathematics*, pages 219–231. de Gruyter, Berlin, October 2013.

[73] Alexander Popp, Barbara I. Wohlmuth, Michael W. Gee, and Wolfgang A. Wall. Dual quadratic mortar finite element methods for 3D finite deformation contact. *SIAM Journal on Scientific Computing*, 34(4):B421–B446, 2012.

[74] Koya Sakakibara. Analysis of the dipole simulation method for two-dimensional Dirichlet problems in Jordan regions with analytic boundaries. *BIT Numerical Mathematics*, 56(4):1369–1400, December 2016.

[75] Stefan A. Sauter and Christoph Schwab. *Boundary Element Methods*, volume 39 of *Springer Series in Computational Mathematics*. Springer, Berlin, Heidelberg, 1st edition, 2011.

[76] Olaf Schenk et al. Pardiso v6.0. `https://www.pardiso-project.org`, 2018.

[77] Erick Schulz and Gantumur Tsogtgerel. Convergence of discrete exterior calculus approximations for Poisson problems. *Discrete & Computational Geometry*, forthcoming.

[78] Jasmin Smajic. A novel variant of the $\mathbf{H}$-ϕ field formulation for magneto-static and eddy current problems. *COMPEL*, 38(5):1545–1561, September 2019.

[79] Jasmin Smajic, Christian Hafner, and Jürg Leuthold. Coupled FEM–MMP for computational electromagnetics. *IEEE Transactions on Magnetics*, 52(3):1–4, August 2015.

[80] Rolf Stenberg. Mortaring by a method of J.A. Nitsche. *Computational Mechanics: New Trends and Applications*, 1998.

[81] Alexander Stepanov and Meng Lee. The Standard Template Library. Technical Report 95-11, Hewlett-Packard Laboratories, Palo Alto, CA, November 1995.

124

[82] Endre Süli, Christoph Schwab, and Paul Houston. *hp*-DGFEM for partial differential equations with nonnegative characteristic form. In Bernardo Cockburn, George Em Karniadakis, and Chi-Wang Shu, editors, *Discontinuous Galerkin Methods*, volume 11 of *Lecture Notes in Computational Science and Engineering*, pages 221–230, Berlin, Heidelberg, 2000. Springer.

[83] Enzo Tonti. A direct discrete formulation of field laws: the cell method. *CMES - Computer Modeling in Engineering and Sciences*, 2(2):237–258, 2001.

[84] Enzo Tonti. Finite formulation of electromagnetic field. *IEEE Transactions on Magnetics*, 38(2):333–336, March 2002.

[85] Il'ja Nestorovič Vekua. *New methods for solving elliptic equations*. North Holland Publishing Company, 1967.

[86] Revaz S. Zaridze, Giorgi Bit-Babik, Kakhaber Tavzarashvili, Nikolaos K. Uzunoglu, and Dimitrios P. Economou. The Method of Auxiliary Sources (MAS) — Solution of propagation, diffraction and inverse problems using MAS. In Nikolaos K. Uzunoglu, Konstantina S. Nikita, and Dimitra I. Kaklamani, editors, *Applied Computational Electromagnetics: State of the Art and Future Trends*, volume 171 of *NATO ASI Series*, pages 33–45. Springer, Berlin, Heidelberg, 2000.

[87] Olgierd Cecil Zienkiewicz. Trefftz type approximation and the generalized finite element method — history and development. *Computer Assisted Mechanics and Engineering Sciences*, 4:305–316, December 1996.

Curriculum Vitae

Personal details

Name	Daniele Casati
Date of birth	4. June 1990
Place of birth	Merate, Italy
Citizenship	Italy

Education

09/2016–12/2019	PhD studies in CSE[*] at ETH Zurich Zurich, Switzerland
09/2012–11/2014	MSc studies in CSE[*] at ETH Zurich Zurich, Switzerland
10/2009–07/2012	BSc studies in Physics at Università di Pavia Pavia, Italy
09/2004–07/2009	Secondary school at Liceo M.G. Agnesi Merate, Italy

[*] Computational Science and Engineering